Doctoral Dissertation

Studies on the role of tribological phenomena based on the direct observation of metal plastic deformation

LIN XIAOKE

January 2025

Graduate School of Engineering,
Osaka University

Contents

Chapter 1 Introduction

1.1 Background

Manufacturing engineering technology holds a paramount position in the national economy of every country worldwide, serving as a cornerstone for industrial progress and economic development. Among its fabricating techniques, metal forming processes emerge as indispensable bases, offering fundamental and reliable means of production [1]. Metal forming processes involve a range of manufacturing techniques employed to shape metal workpieces into desired configurations and dimensions. These processes entail the application of pressure or force to induce deformation in the metal material, without the removal of any material, thereby ensuring optimal material utilization and minimizing waste [2-3]. For example, Fig. 1.1 shows typical illustrations of bulk metal forming and sheet metal forming processes [4]. These manufacturing methods not only ensure the fabrication of workpieces endowed with high strength, superior performance, and intricate shapes, but also boasts inherent advantages such as heightened productivity and diminished consumables usage [5-6]. Consequently, metal forming processes find extensive application in industries including automotive, aerospace, construction, and manufacturing for producing a diverse array of metal components and products, as illustrated in Fig. 1.2. Each process offers distinct advantages in terms of efficiency, precision, and the types of shapes achievable [7-9].

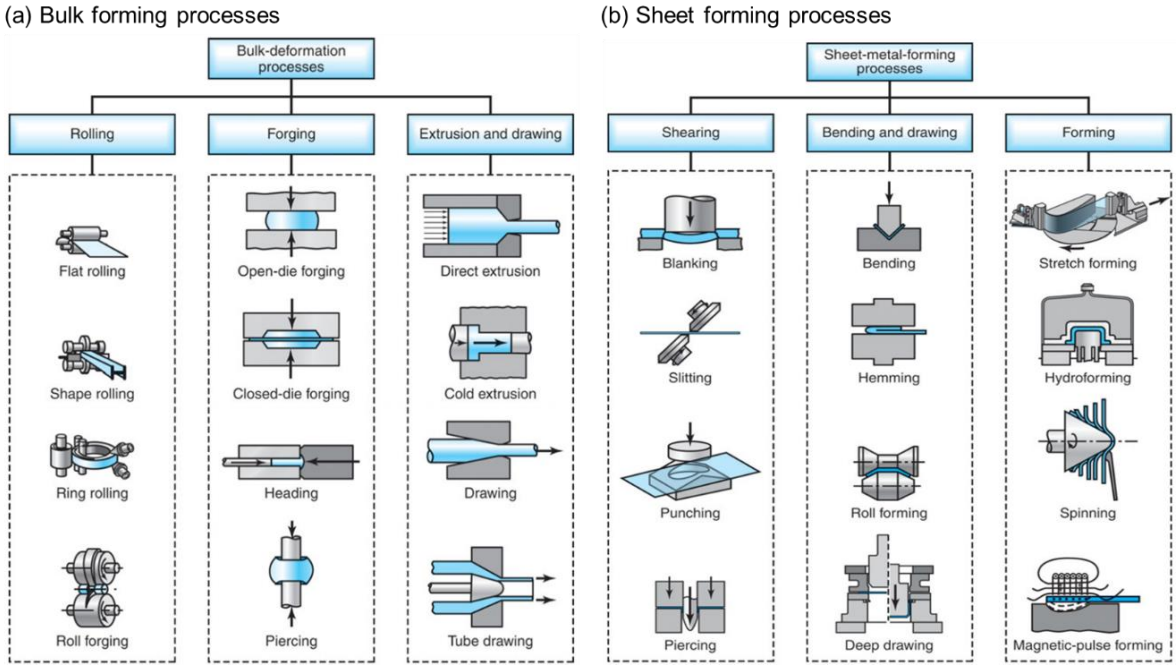

Fig. 1.1 The illustrations of typical (a) bulk and (b) sheet metal forming processes [4]

Fig. 1.2 Some important examples of industrial applications in metal forming processes [6]

Metal forming products are ubiquitous in our daily lives, appearing in a vast array of items that we encounter regularly. These products range from simple items composed of only a few parts, such as eyeglasses and pencil cases, to highly complex assemblies comprising hundreds or even thousands of parts, like computers, automobiles, and airplanes, which are found in various forms across the globe [10]. For instance, Fig. 1.3 provides an illustration of an automobile component that consists of various metal forming products, showcasing the intricate interplay of numerous formed metal parts [4]. Undoubtedly, the integrity and reliability of metal forming products serve as the cornerstone of modern industrial development and technological advancement, underpinning the functionality and durability of countless devices and machines. Consequently, ensuring the avoidance of surface defects in these products is crucial for maintaining their reliability and performance, thereby sustaining the high standards required for their widespread application in diverse industries.

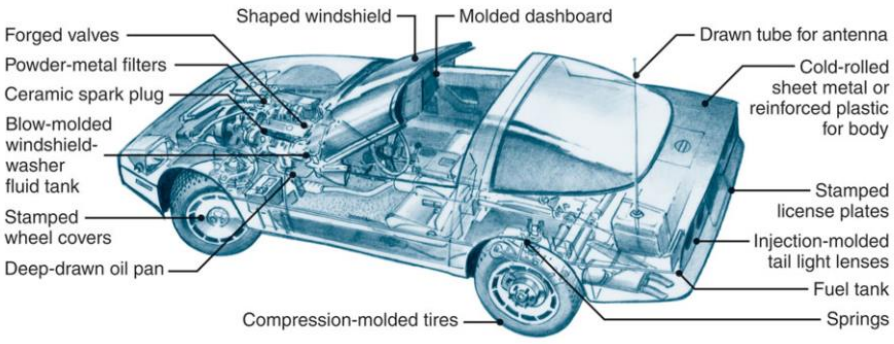

Fig. 1.3 The illustration of an automobile component [4]

It is widely acknowledged that tribological phenomena at the interface play a pivotal role in the occurrence of defects in metal forming processes, and Fig. 1.4 lists some defects occurring in these products [11-14]. As depicted in Fig 1.4, common defects like cracks, arise from excessive deformation beyond the limit of material due to high friction or uneven stress distribution [11]. Conversely, wrinkling manifests as undesired folds or ridges on the product surface, stemming from elevated frictional forces hindering material flow and causing localized deformation, ultimately resulting in wrinkle formation [12]. Clearly, the severity of friction phenomena at the interface disrupts appropriate material flow, culminating in surface defects during these processes. These imperfections invariably compromise the integrity of metal forming products and eventually impede the advancement of industrial technology. It is evident that investigating tribological phenomena at the interface is indispensable for avoiding surface defects and achieving high-quality metal forming products.

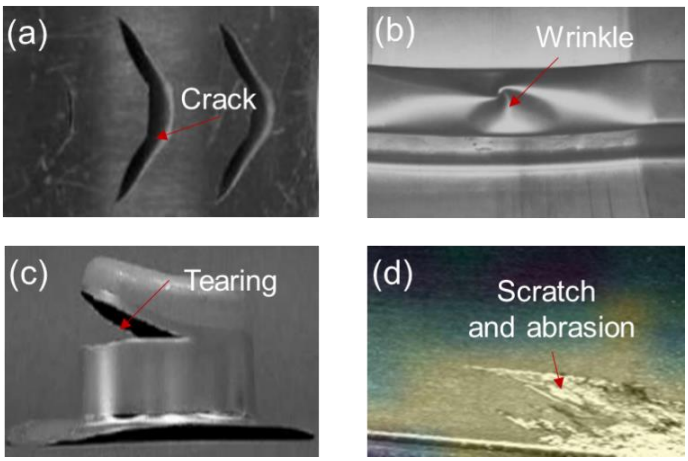

Fig. 1.4 Common defects of forming products: (a) crack, (b) wrinkle, (c) tearing, (d) scratch and abrasion

In recent years, driven by advancements in science and technology and the pressing need for high-quality products, High-Mix Low-Volume (HMLV) production has emerged as the mainstream in the manufacturing sector [15]. HMLV Manufacturing involves producing a diverse range of products in small quantities. This production approach is frequently employed to manage and manufacture unique and intricate products with precise quality specifications. Items that were traditionally mass-produced, such as vehicles or appliances, are now customized and crafted to meet individual customer requirements, thus necessitating HMLV production methods [16-17]. Inevitably, there has been an increasing need for high-mix low-volume manufacturing within the metal forming process, coupled with diverse requirements for achieving both high quality and cost-effective production technologies [18-19]. This places higher demands on the quality of the

metal forming products, thereby further underscoring the heightened significance of comprehending tribological phenomena at the interface. Notably, the study of tribological phenomena is evidently essential for attaining high-quality metal forming products, serving as a cornerstone for the rapid advancement of modern industrial technology. Therefore, there is an urgent demand for a new technique or method to explore the effects of tribological phenomena and develop a deeper understanding of friction phenomena at the interface during plastic processing.

1.2 Prior research

The preceding background introduction and discussion emphasize the significance of studying tribological phenomena at the interface and underscore the pressing need to propose a new technique or method to explore the effects of these phenomena in the metal forming process. Consequently, a summary of prior research on these subjects is presented, focusing on an overview of tribology, tribological phenomena and related friction models in metal plastic processing, the correlation between deformation behavior and tribological phenomena, the methodologies used to investigate these relationships, as well as techniques to quantify deformation behavior in manufacturing processes.

1.2.1 Overview of tribology

Tribology is an interfacial phenomenon that is affected by physical and mechanical properties of the two interacting surfaces as well as operational conditions, primarily investigating the laws of friction, wear, and lubrication between relative moving surfaces, along with their control techniques. It encompasses various industrial fields such as traditional mechanical processing, transportation, aerospace, marine, chemical engineering, and bioengineering [20-21]. The term “tribology” was first introduced by a UK government committee from Britain in 1966, defining it as an interdisciplinary subject concerning the theory and application of the study of friction, lubrication, and wear between relative moving surfaces, and their interrelationships, even though friction, lubrication and wear had been studied for many years before then and have a long and fascinating history [22]. For effective solution of tribology problems, all three constituents should be considered carefully and equally, and Fig. 1.5 lists the illustration for this tribology triangle [23]. Theoretical principles and techniques of tribology can be utilized to enhance the operational efficiency of mechanical systems, prolong their service life, reduce accidents, and provide effective solutions to challenges faced by human society, such as energy shortages, resource depletion, environmental pollution, and health issues. An overview of the key components of tribology will be introduced in the following section.

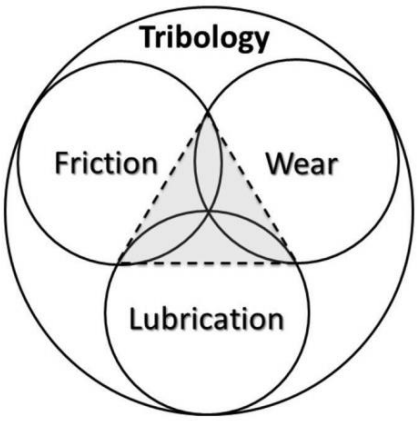

Fig. 1.5 Tribology triangle [34]

(1) Friction [24]

Research on friction primarily aims to elucidate the origins of frictional forces and their energy dissipation mechanisms, among other fundamental physical processes and mechanisms. Friction is defined as the resistance encountered when one surface slides or rolls over another. This broad definition embraces an important class of relative motion: sliding. In ideal sliding, a tangential force F is required to move the upper body over the stationary counterface. Experimental evidence demonstrates that the friction force is frequently linearly proportional to the normal load force W applied to the body. This phenomenon is referred to as Coulomb friction. The ratio between this frictional force and the normal load is termed the coefficient of friction, typically denoted by the symbol μ, that is:

$$\mu = \frac{F}{W} \tag{1.1}$$

Bowden and Tabor developed the friction theory to elucidate the causes of friction [25]. According to this theory, friction comprises two components: the adhesive component, which is an adhesion force developed at the areas of real contact between the surfaces (the asperity junctions), and the plowing component, which is a deformation force required to plow the asperities of the harder surface through the softer one. The resultant frictional force F is then regarded as the sum of the two contributing terms: F_{adh} due to adhesion and F_{def} due to deformation. These components are independent to each other, such that:

$$F = F_{adh} + F_{def} \tag{1.2}$$

These conventional friction models can explain most practical situations and therefore have a wide range of applications. However, for complex tribological phenomena, such as friction occurring at the interface in metal forming processes, these friction models are not suitable for describing the tribological phenomena at the interface.

(2) Wear [26]

Studies on material wear seek to reveal the mechanisms of material removal and influencing factors, thereby establishing physical models, mathematical descriptions, and seeking lubrication, surface treatment, and other technologies to reduce friction and control wear, which holds significant significance for the national economic development. Wear refers to the gradual loss of material from a surface due to mechanical actions like sliding, abrasion, or fatigue. During relative motion, material on the contact surface may be displaced so that properties of the solid body near the surface are altered. Material may then be removed from a surface, resulting in transfer to the mating surface or breaking loose as a wear particle. Like friction, wear is not a material property; it is a system response. Table 1.1 lists different types of wear mechanisms, definitions, and characteristics [27]. Researchers investigate wear mechanisms and develop strategies to minimize wear through the selection of appropriate materials, surface treatments, and lubrication regimes. By reducing wear, engineers can extend the lifespan and reliability of mechanical components.

Table 1.1 Different types of wear mechanisms, definitions, and characteristics [27]

Mechanisms	Definitions	Characteristics
Adhesion	Transfer of material from one surface to another surface by shearing of solid welded junctions of asperities	Adhesive bonding, shearing, and material transfer
Abrasion	Hard particles or protuberances sliding along a soft solid surface	Plowing, wedging, and cutting
Delamination	Delamination of thin material sheets beneath the interface in the subsurface	Plastic deformation, crack nucleation, and propagation
Erosion	Mechanical interaction between solid surface and a fluid, or impinging liquid or solid particles	Angle of incidence, large-scale subsurface deformation, crack initiation, and propagation
Fretting	Small amplitude oscillatory tangential movement between two surfaces	Relative displacement amplitude and entrapment of wear particles
Fatigue	Fracture arising from surface fatigue	Cyclic loading and fatigue crack propagation
Corrosion	Sliding takes place in corrosive environment	Formation of weak, mechanically incompatible corrosive layer

(3) Lubrication [28-29]

Lubrication serves as a necessary means to reduce friction and minimize or prevent wear. The development and proper application of lubricants and lubrication techniques represent the primary technical pathways to significantly enhance mechanical efficiency, ensure long-term reliable operation of machinery, and conserve energy. From ancient times to the present, lubrication has been an effective practical means for two simultaneous purposes: reducing friction losses and extending the service life of rubbing machine parts. The function of the lubricant is to keep the twin components of a part, like bearings and reducers, separated. Lubricants are also used to reduce friction in machine-tool work, such as cutting, forming and grinding. Lubricants, according to their physical state, may be solid, liquid, or gaseous. There are also intermediate types: semisolid and semiliquid. Tribologists study the properties and behavior of lubricants, including viscosity, film formation, and boundary lubrication. Effective lubrication helps minimize frictional losses, dissipate heat, and protect surfaces from damage, thereby enhancing the efficiency and durability of mechanical systems.

In summary, tribology is a multidisciplinary field that encompasses the study of friction, wear, and lubrication in mechanical systems. Through understanding and controlling tribological phenomena, engineers can develop strategies to optimize performance, enhance reliability, and extend the lifespan of components in various applications.

1.2.2 Tribological phenomena in metal plastic processing

In metal forming processes, tribological phenomena refers to interactions occurring at the contact interface between the tool/die and the workpiece material during deformation. These interactions can significantly impact the forming process and the quality of the final products [30]. Among these, interface friction plays a critical role in metal forming processes. It is well-known that tool/die-material interfaces in metal plastic processes are characterized by severe conditions of friction and these conditions have a pivotal role in bulk deformation, influencing tool life, energy consumption, as well as the performance and mechanical properties of the processed material [31-33]. For example, friction at the tool-workpiece interface plays an important role in determining the strain distributions [34] and non-uniform friction stress can result in uneven strain distribution [35]. Additionally, excessive friction between the die and workpiece material can result in surface defects such as scratches, cracks, or wrinkles. These defects compromise the quality of the formed product and may require additional processing steps for correction [36-37]. Moreover, frictional forces dictate the material flow during metal forming. High friction at the die-workpiece interface can impede smooth material flow, leading to uneven deformation and limiting the extent to which a material can be deformed before failure [38]. This impacts the overall formability and dimensional accuracy of the formed components [38-39]. Undoubtedly, friction between the die and workpiece is fundamental to the efficiency and quality of the metal forming process, affecting the formability of bulk material, tool life, as well as the surface finish of the specimen [36, 40].

Another critical tribological phenomena in metal forming processes is the occurrence of adhesion at the interface, particularly in workpiece materials that are chemically active. For instance, dry forming and machining of aluminum alloys are often associated with high adhesion at the die-workpiece interface [41-42]. This is primarily due to work materials undergo severe plastic deformations in metal forming process and usually stretch to 10-20 times their original surface area, leading to a substantial surface enlargement or surface expansion and subsequent exposure of a chemically active nascent surface [43-44]. It cannot be ignored that adhesion-induced wear on the die surface is a prevalent issue in metal forming. When workpiece material adheres to the die surface, it can cause abrasion, material transfer, and surface degradation, ultimately leading to premature die failure and increased maintenance costs [45]. Additionally, adhesion contributes to the overall frictional forces experienced during metal forming. As the tool

and workpiece surfaces adhere to each other, the resistance to relative motion increases, affecting material flow, formability, and process efficiency. Excessive adhesion between the tool and workpiece can restrict the formability of materials. Adhesive forces can impede deformation and hinder the smooth flow of material, resulting in defects such as wrinkles, tears, or cracking, particularly in deep drawing or forming processes [46]. Undoubtedly, adhesion, alongside friction, is a critical aspect of tribological phenomena in metal plastic processing.

While the examination of friction phenomena remains crucial in metal forming processes, addressing tribological phenomena, such as extreme friction and adhesion phenomena occurring at the contact interface, emerges as a pivotal factor influencing the quality of metal forming products, thus warranting considerable attention. To mitigate friction and adhesion while enhancing surface finish, lubricants are commonly applied to the tool-workpiece interface [47]. It is widely acknowledged that lubricants have the capability to modify interfacial friction conditions, facilitate the flow of workpiece material, and prevent adhesion of the workpiece material to the tool/die surface [48]. Liquid lubricants are distinguished by their excellent cooling properties, ease of handling, and superior permeability, making them the most commonly used option under general conditions [49-50]. Traditional methods for evaluating lubrication effectiveness often involve complex experimental setups, with many providing only qualitative assessments [51]. Additionally, methods for evaluating lubricant performance, such as ring testing [52] or compression-tension testing [53], assess lubrication effectiveness within specific environments. However, in real plastic processing, tribological phenomena are highly complex. Despite effective lubrication in controlled test environments, there is a risk that lubricants may prove inadequate in actual manufacturing processes, eventually resulting in rough machined surfaces or even tool damage. Hence, there is a pressing need to devise lubrication evaluation methods suited to real processing environments.

In summary, tribological phenomena at the interface are crucial in metal forming processes due to their significant influence on the quality, efficiency, and reliability of manufacturing operations. Understanding and effectively managing these phenomena are essential for achieving desired outcomes in metal forming. This also highlights the importance of precise friction models to accurately describe these interactions.

1.2.3 Friction models

To accurately depict the tribological phenomena in forming processes, it is imperative to employ a friction model that aligns reasonably with reality. Classic friction models like Coulomb friction and constant friction models continue to be utilized in the majority of forming processes [24, 54]. For example, the Coulomb friction model provides a straightforward way to incorporate friction into the analysis of metal forming processes such as forging, rolling, extrusion, and stamping [55-57]. By using a constant coefficient of friction, it simplifies the calculations needed to predict the forces and energy required for deformation. However, the assumption of a constant coefficient of friction (μ) is a significant simplification. In reality, μ can vary with factors such as contact pressure, temperature, sliding velocity, and surface roughness, which can lead to inaccuracies in predictions. Particularly, the Coulomb model does not consider the influence of normal pressure on friction. In metal forming processes, contact pressure can vary widely, and this variation can significantly affect frictional behavior.

To address this issue, Wanheim et al. proposed an extension of the traditional Coulomb friction model, incorporating the dependency of friction on the normal pressure, as expressed in Eq. 1.3 [58]:

$$\tau_n = m\alpha k \tag{1.3}$$

where τ_n denotes nominal friction stress, k is the yield stress in pure shear, m is the friction factor, α represents the real area of contact and in Fig. 1.6, α is plotted as a function of normal pressure $q/2k$ with the friction factor m as a parameter. This modification offers a more accurate representation of frictional behavior under varying conditions. Furthermore, Fig. 1.7 illustrates the relationship between nominal friction stress and normal pressure with the friction factor m serving as a parameter. The results demonstrate that friction conditions at high normal pressures differ significantly from those at low normal pressures. At lower normal pressures, Amonton's law is valid; however, it becomes meaningless under large pressures because the coefficient of friction becomes pressure-dependent. This model provides a more realistic representation of frictional forces in processes where contact pressure can vary significantly. Undoubtedly, this model has its limitations. For example, it relies on the accurate determination of the reference friction factor; incorrect parameter values can lead to significant deviations in the predicted frictional behavior. Additionally, it does not account for the effect of plastic deformation on frictional conditions at the interface, thereby limiting its applicability.

To overcome these limitations, scholars worldwide have proposed various improved friction models building upon the classic friction models. Table 1.2 presents the mathematical expressions, main character and applications of these friction models.

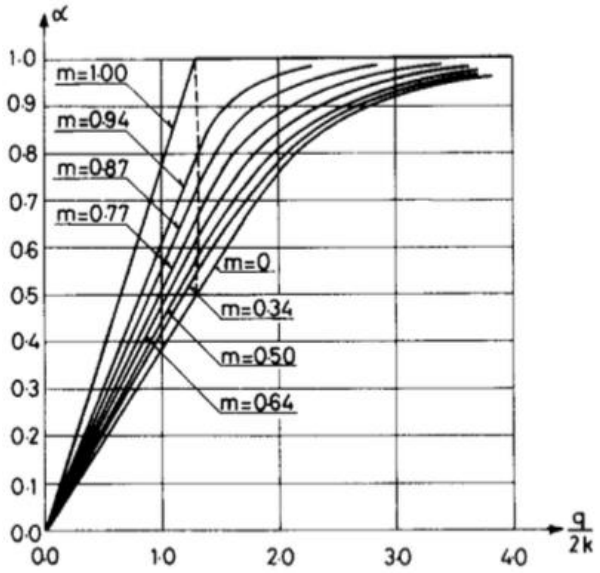

Fig. 1.6 The real area of contact as a function of the normal pressure and the friction factor [58]

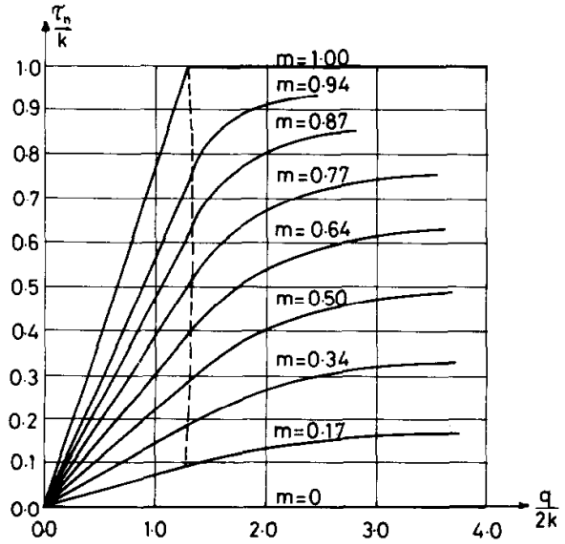

Fig. 1.7 The nominal friction stress as a function of the normal pressure and the friction factor [58]

Table 1.2 Mathematical expression and main character and applications of fiction models [59]

Friction model	Mathematical expression	Main character and applications
Correction model [60]	$\tau = -mk\frac{2}{\pi}\arctan(\frac{v_s}{A})$	Arbitrary curve contact boundary friction conditions
The general friction model [61]	$\tau_n = fak$	A wider range of forming pressure
Realistic friction model [62]	$\tau_f = \begin{cases} \frac{\mu(U_1-U_2)}{h} & (h > 10\sigma) \\ \frac{\mu(U_1-U_2)}{h} & (30\sigma > h > 10\sigma) \\ \tau_a + \tau_a A + \tau_p(1-A) & (h \le 3\sigma) \end{cases}$	Suitable for a wider range of contact lubrication conditions
The dynamic friction model [63]	$\tau_n = \beta\frac{dv_t}{dz}p$	High prediction accuracy on contact stresses at neutral plane
The empirical friction model [64]	$\frac{\tau}{\tau^*} = A\left(\frac{p}{p^*}\right)^a B^{(T-T_0/T^*-T_0)^b}$	Cold forging of aluminum, steel and stainless steel

Due to differing viewpoints and considerations, the friction models mentioned above, including both classic and recent ones, may suit specific plastic forming processes, yet there are still lacks of friction models with adequate accuracy. Furthermore, despite the numerous models proposed to date (Table 1.2), they basically rely on empirical equations grounded in various assumptions and are often criticized for deviating from actual phenomena. This raises questions like how to determine the physical factors governing the constant component in the models or how different machining conditions affect the distribution of friction stress. More importantly, existing friction models do not account for the effects of plastic deformation on tribological conditions at the interface, limiting their scope and applicability. Notably, these models fail to address these considerations adequately. Therefore, exploring friction models based on the response of actual deformation behavior becomes particularly crucial for comprehensive understanding tribological phenomena, serving as a major motivation and objective of this dissertation.

1.2.4 The correlation between deformation behavior and tribological phenomena

The limitations of existing friction models indicate their inability to appropriately describe the tribological phenomena at the interface of the current metal forming process, and therefore it is particularly important to explore a new technique or methodology to study tribological phenomena.

It is well known that deformation behavior is intricately linked with friction phenomena, which significantly impact the final performance and mechanical properties of the material undergoing processing [65]. For example, in severe interface friction conditions, a phenomenon of material flow localization caused by variations in velocity gradients occurs near the tool/die-material contact interface, significantly impacting material removal processes and the quality of material forming [40, 66, 67]. It has been reported that this localization of material flow closely resembles a fluid-like boundary layer, as illustrated by the parallel flow lines shown in Fig. 1.8 [66], which indicate substantial velocity gradients across the secondary shear zone. Since the secondary shear zone is extremely thin compared to the chip, and shear occurs through a viscous-like drag along the rigid tool boundary, a clear boundary layer analogy can be drawn with fluid mechanics. Similar phenomena also occur in metal forming processes, such as in the deformation of cold-extruded billets during the extrusion process, as illustrated by the grid distortion shown in Fig. 1.9 [67]. However, the presence of wall-relative velocity at the tool-material interface suggests that the traditional no-slip boundary condition may not accurately capture this deformation behavior [68-69]. The no-slip assumption at the liquid/solid interface, which has been widely supported by extensive experimental evidence in macroscopic analyses of fluid film lubrication [70], contrasts with microscopic scales where localized sliding occurs at the interface [71]. This phenomenon, akin to the slip observed at the tool-material interface, suggests non-uniform friction conditions along the contact surface [66, 72]. The presence of flow localization and slip conditions at the tool/die-material interface illustrates the deformation characteristics near the contact interface arising from interface friction. These deformation behaviors notably indicate their close correlation with tribological phenomena.

Additionally, dry forming and machining of aluminum alloys are often associated with high adhesion at the die-workpiece interface due to the severe deformation and high surface expansion experienced by the work material [41, 73]. A large surface expansion inevitably increases the amount of chemically active nascent surface generated, ultimately leading to higher adhesion. Clearly, the surface expansion ratio could serve as an indicator of interface adhesion. This ratio is typically used in metal forming to indicate the magnitude of the nascent surface generated [72, 74]. It is the ratio of the enlarged surface area of the final products to the original surface area of the undeformed specimen [75]. Severe surface expansion caused by a plastic deformation of the workpiece is known to cause a flattening of the asperities, increase frictional

traction, and cause a drastic change in the tribological properties [74, 76]. Furthermore, the large surface expansion associated with severe adhesion and friction often leads to the breakdown of the lubricant film, pick-up of the workpiece material on the tool, and the consequent damage of specimen surfaces [77]. Consequently, understanding the behavior of surface expansion plays a pivotal role in comprehending tribological properties under severe contact conditions. Although the factors determining the distribution of surface expansion are still under discussion, investigating the development of the boundary layer structure might elucidate the role in how the surface of bulk material expands at the contact interface. This is because both surface expansion and the plastic boundary layer result from interface friction under severe sliding contact conditions.

In short, deformation behavior and tribological phenomena are closely linked. Exploring the quantitative relationship between friction phenomena and deformation behavior would be the key to gain a comprehensive understanding of tribological phenomena at the interface in metal plastic processes.

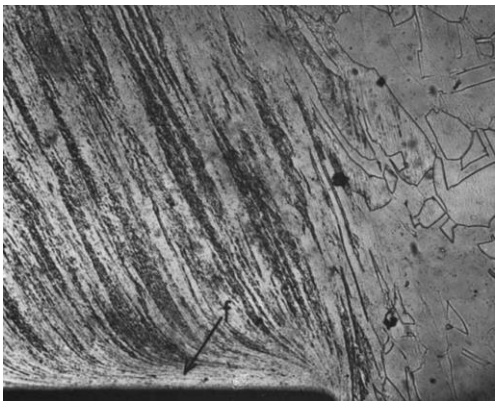

Fig. 1.8 The observation of flow lines by quick-stop section in metal cutting [66]

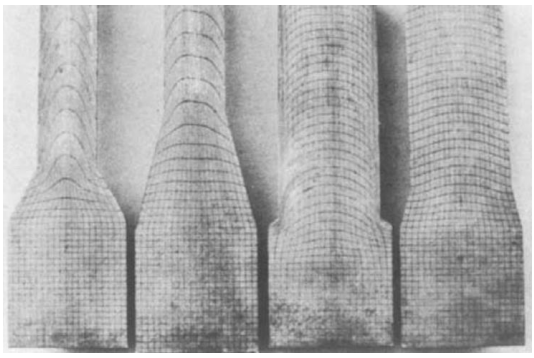

Fig. 1.9 The grid distortion of cold extruded billets [67]

1.2.5 Methodologies to explore deformation-tribology correlation

It is evident that deformation behavior and tribological phenomena are closely related, prompting numerous researchers to employ various methodologies to explore their correlation. These methodologies include tensile testing, the finite element method, slip line field analysis, and photoelasticity. Thus, the strengths and limitations of these conventional methods are introduced in the following sections.

(1) Tensile testing

Tensile testing is a fundamental mechanical test employed to ascertain the mechanical properties of materials, notably metals [78]. It entails applying a controlled tensile load to a standardized test specimen until it fractures. Throughout the test, parameters such as stress, strain, and strain rate are measured and recorded. Tensile testing yields crucial data on material behavior under tension, encompassing elastic modulus, yield strength, ultimate tensile strength, and elongation [79]. In the context of exploring the relationship between deformation behavior and tribological phenomena in metal forming, tensile testing serves to characterize the mechanical properties of the material both before and after forming [80-85]. For example, S. Msolli proposed a multiscale modeling approach for the mechanical behavior of metals and validated this scheme by comparing simulated responses to experimental data obtained from tensile tests [82]. Similarly, Yaping Wang validated a new strain rate-sensitive solid-state pressure bonding model through a series of compression tests and determined the interface bond ratio by conducting tensile tests [83]. By subjecting specimens to tensile testing before and after forming processes, engineers can assess changes in material properties and deformation behavior resulting from interface phenomena such as friction, lubrication, and material interactions [84-85]. In summary, tensile testing is a powerful tool for exploring the relationship between deformation behavior and tribological phenomena in metal forming processes. Through conducting controlled experiments and analyzing mechanical properties under tension, researchers can gain valuable insights into material behavior and optimize forming processes for improved performance and quality. However, tensile testing primarily involves applying uniaxial loading conditions, which can pose challenges when interpreting test results in the context of metal forming applications. Moreover, these conditions may not accurately simulate the complex multiaxial stresses experienced in metal forming processes, due to the differences in loading conditions and deformation mechanisms [80]. Consequently, this mismatch can result in inaccurate predictions of material behavior.

(2) Finite element method (FEM)

FEM is a computational technique used to simulate the behavior of materials and structures under various loading conditions. It involves discretizing the geometry of the object

into finite elements and applying mathematical equations to model the physical behavior of the material. FEM can predict parameters such as stress, strain, displacement, and deformation in complex structures or components [86-87]. In the context of metal forming, FEM can be used to simulate the deformation behavior of metal workpieces, including the effects of tribological phenomena such as friction, lubrication, and material interactions [88-92]. For example, Ramin Ebrahimi proposed an alternative design for the extrusion process by observing the deformation behavior of these processes through EFM and verified that this geometry holds strong potential for industrial applications [89]. Similarly, Shubo Xu utilized the same method to propose a new metal forming process and studied its deformation behavior. The results showed that these numerical simulation findings could offer valuable guidelines for die design, determination of process parameters, and process planning [90]. By incorporating material properties, boundary conditions, and process parameters into the simulation, engineers can analyze how different factors influence deformation behavior and optimize forming processes accordingly. While FEM simulations offer a powerful tool for modeling metal forming processes, they frequently depend on simplifying assumptions and idealizations to manage computational complexity [87]. Nevertheless, these simplifications may inadequately represent the intricate physics and material behavior inherent in metal forming operations, thereby resulting in inaccuracies in predictive outcomes.

(3) Slip line field

A slip line field is a graphical method used in solid mechanics and plasticity theory to analyze the deformation behavior of materials undergoing plastic deformation. It offers a qualitative understanding of the stress and strain distribution in a deforming material by delineating regions where slip or plastic deformation occurs [93]. In slip line field theory, the material undergoing plastic deformation is divided into imaginary slip lines, each representing a path along which material particles slide past each other due to applied stresses. These slip lines are assumed to be continuous and non-intersecting within the material. The direction and magnitude of the velocity gradient along these slip lines provide information about the deformation behavior and flow patterns within the material [94-96]. In summary, slip line field analysis provides a valuable framework for understanding the deformation behavior and flow patterns in metal forming processes. By analyzing slip line patterns and velocity gradients within the material, researchers can gain insights into how tribological phenomena influence deformation behavior and optimize forming processes for improved performance and product quality. Nevertheless, the slip line field method often relies on simplified assumptions regarding material behavior and deformation mechanisms [95]. These assumptions may fail to fully capture the intricate physics and material behavior encountered in real-world metal forming processes,

resulting in inaccuracies in predictions.

(4) Photoelastic method

Photoelasticity is an experimental method used to study stress distribution and deformation in materials by observing birefringence patterns induced by stress [97]. This technique is particularly valuable for visualizing stress fields in transparent models, providing a direct visual representation of stress distribution through isochromatic fringes. These fringes can be analyzed to study friction and contact problems by examining the stress distribution at interfaces [98-101]. For example, C.W. Wern conducted a photoelastic study to examine the stress fields in the cutting process, verifying that the stress fields when cutting copper fibers vary with fiber orientation in a manner similar to the cutting force [101]. This helps in understanding how tribological conditions affect stress and deformation. Additionally, it serves as an excellent tool for validating numerical models. For instance, Tarkes Dora Pallicity used digital photoelasticity to validate simulations of the precision glass molding process [102]. By comparing photoelastic results with simulation outputs, one can verify and refine computational models. However, photoelasticity requires transparent models made of birefringent materials, which typically differ from the actual metals used in forming processes. This discrepancy in material properties can lead to inaccuracies when extrapolating results to real metal forming scenarios. Moreover, while photoelasticity is excellent for qualitative analysis, obtaining precise quantitative stress values necessitates meticulous calibration of the photoelastic material, which can be challenging and time-consuming [101]. Clearly, this technique has limitations in quantifying the effects of tribological phenomena on metal plastic deformation.

In summary, there is still a lack of research focusing on the actual quantitative relationship between tribological phenomena and deformation behavior. This gap persists due to the extreme difficulty in quantitatively investigating interface deformation at tool-material interfaces using conventional methods such as the quick-stop tests and grid marking techniques [103-105]. This challenge arises because material flow is highly localized near the friction interface, and the region of high deformation is extremely thin. Hence, the development of a new technique or methodology that enables quantifying interface deformation behavior could signify a breakthrough in quantitatively exploring the relationship between tribological phenomena and bulk deformation fields. Such advancement invariably enhances our understanding of tribological applications in fundamental machining or forming processes, serving as a milestone breakthrough in the rapid development of modern manufacturing technology.

1.2.6 Techniques to quantify deformation behavior

The preceding discussion emphasizes the role of deformation behavior in comprehending tribological phenomena, with a key difficulty on the technique for quantifying this behavior. Therefore, this section will introduce both conventional and state-of-the-art techniques used to quantify deformation behavior.

(1) Strain gauges

Strain gauges are devices employed to measure the strain experienced by an object undergoing deformation. They consist of thin wires or foil patterns arranged in a grid-like configuration and affixed to the surface of the deforming object. As the object deforms, the strain gauges undergo a change in electrical resistance proportional to the strain magnitude. Throughout the metal forming process, the strain gauges continuously monitor the deformation of the workpiece in real-time [106]. By detecting alterations in resistance due to strain, the strain gauges provide crucial data. This data enables the analysis of strain distribution across the workpiece, measurement of deformation magnitude, and identification of areas experiencing high stress or strain [107-111]. For instance, C. Fast Irvine devised an experimental methodology aimed at characterizing the constitutive behavior of anisotropic sheet metals across a range from uniaxial to plane strain tension, which was accomplished through the utilization of strain gauges as the standard uniaxial tension tests [109]. Paulo Flores presented a methodology rooted in numerical analysis of plane strain tensile tests conducted on various materials and specimen geometries. The objective was to experimentally discern the evolution of the homogeneous strain field zone during deformation. This study established an expression for computing the actual stress within the specimen's plane strain state zone along the loading direction, leveraging experimental data and incorporating the evolution of edge effects in terms of plastic strain [110]. On the other hand, Shakil Bin Zaman employed strain gauges to measure the average strain accumulated along each loading axis until fracture occurred to ascertain and validate a distortional plasticity model using an optimization algorithm [111]. By correlating strain measurements with related variables, researchers can optimize the metal forming process to enhance product quality, minimize defects, and improve efficiency. Overall, strain gauges offer valuable insights into the deformation behavior of metal workpieces during forming processes, enabling researchers and engineers to gain a deeper understanding of the manufacturing process and exert greater control over it. However, traditional strain gauges, typically necessitate direct contact with the material surface and offer only point measurements at specific locations on the workpiece surface [106]. This invasive requirement can disrupt the forming process, modify material behavior, and overlook certain deformation features, ultimately resulting in inaccurate measurements.

(2) Grid marking methods

Grid marking methods, also known as grid analysis or grid marking techniques, entail applying a grid pattern onto the surface of a material or specimen. This pattern comprises regularly spaced lines or dots that function as reference points for measuring deformation during mechanical testing or material processing, such as metal forming [105, 112]. The metal workpiece undergoes the metal forming process, whether it involves forging, rolling, bending, or another deformation method. During the process, the metal undergoes deformation, leading to a corresponding deformation of the grid pattern applied to its surface. Following the completion of the metal forming process, the deformed grid pattern undergoes examination and analysis. Any alterations in the spacing, orientation, or shape of the grid lines or dots indicate the magnitude and direction of deformation experienced by the metal workpiece during forming [113-117]. For example, S. K. Barik utilized circular grids printed on the sheets to determine the effective strain distribution, aiming to validate that the forming behavior of the material depends on both the degree of pre-strain and the change in pressure [116]. In another instance, C. Bandini validated a metal forming finite element (FE) code by comparing it to grid-based experiments. Additionally, they implemented a theoretical model to predict the grain size and shape evolution of aluminum alloys [117]. Overall, through a comparison between the deformed grid pattern and the original, undeformed grid, researchers can quantify the extent of deformation, strain, and deformation gradients across the metal workpiece. These methods serve as valuable tools for investigating deformation behavior in metal forming processes, aiding in the optimization of process parameters, enhancement of product quality, and advancement of understanding regarding material behavior under mechanical loading. However, due to the spatial resolution limits of the grid lines, such as the constraints on grid line spacing and width, it is extremely difficult to observe and capture the characteristics of interface deformation near the contact surface [113]. This difficulty arises from the higher localization and thin layer of the friction-induced deformation field during the metal plastic deformation process.

(3) Quick-stop tests

The quick-stop test is a method employed in metal forming to assess the formability of metal materials. This procedure entails suddenly halting the deformation process during a forming operation, commonly achieved by ceasing the motion of the forming tool while the metal undergoes deformation [104, 118-120]. The objective of this test is to examine the final state of the formed part and analyze any defects or failure modes that may arise. For instance, U. Wiklund utilized a quick stop test to halt the cutting process of stainless steel, enabling observation of the initial layer adhering to the tool surface [119]. Similarly, Koichi HosHl employed the same method to elucidate the mechanism behind the variation of the built-up edge during metal cutting

[120]. It furnishes invaluable insights for process design, material selection, and quality control within metal processing applications. On the other hand, it is evident that quick-stop tests offer only a snapshot of the forming process at the moment of interruption. Consequently, they may fail to capture the dynamic behavior or transient phenomena occurring during deformation, thus limiting the understanding of deformation behavior.

(4) Digital image correlation (DIC) and particle image velocimetry (PIV)

Digital image correlation (DIC) is an optical technique employed to measure full-field displacements and strains on the surfaces of objects undergoing deformation. It involves capturing images of a speckle pattern applied to the specimen surface before and after deformation, and then correlating these images to calculate displacement fields [121]. DIC emerges as a potent tool for observing deformation behavior in metal forming processes owing to its capacity to furnish detailed, high-resolution data across expansive areas. It offers comprehensive full-field strain data, facilitating a thorough understanding of deformation behavior throughout the entire workpiece [122-127]. For example, utilizing DIC technique, Lin Lv introduced a testing method and analytical procedure for materials experiencing complex stress/strain states. This method could be considered an ideal approach for establishing materials databases that focused on accurately describing the mechanical and fracture behaviors of materials [125]. While Pedram Farahnak utilized DIC to analyze material behavior in sheet metal forming and subsequently determined strain rate sensitivity through corresponding experiments [126]. Additionally, it is capable of capturing dynamic deformation events in real-time, offering insights into transient deformation behavior during metal forming processes. Related research, such as that conducted by Pengjing Zhao [127], employed the digital image correlation method to measure the displacement field and monitor the evolution of strain fields and crack initiation during deformation. This suggested that the method offered a comprehensive and precise description of the diverse damage evolution processes observed in blanking aluminum alloy sheets. Overall, DIC proves to be a valuable tool for characterizing deformation behavior in metal forming processes and has the potential to contribute significantly to the optimization and enhancement of manufacturing processes. However, it highly relies on high-contrast and non-repetitive speckle patterns on the surface of the specimen to ensure each subset of the image is unique for accurate correlation [121]. Clearly, creating a suitable speckle pattern on metallic surfaces can be challenging.

In recent years, particle image velocimetry (PIV) has become increasingly prevalent in manufacturing industries and the fundamental principle underlying PIV is the image correlation technique [128]. Generally, PIV is a method employed to measure the velocity field of a fluid flow by tracking the motion of particles suspended within the flow and capturing consecutive images using a camera. Conversely, DIC is a technique utilized to measure deformation and strain

fields in materials under load [129]. Although initially employed to acquire instantaneous velocity data in fluids, PIV has now been adapted to investigate deformation in severe plastic deformation processes of metals during machining and forming processes [69, 130-131]. This method has been successfully employed to investigate deformation in punch indentation, plastic flow during metal cutting, and the analysis of flow dynamics in metal sliding [132-135]. It enables the direct observation of interface phenomena and deformation characteristics, offering a novel avenue for exploration. This approach facilitates the quantification of deformation behavior, thereby contributing to a comprehensive understanding of extreme friction conditions at interfaces and marking a significant advancement in the application of tribology in metal plastic processing.

In summary, DIC/PIV presents notable advantages and considerable potential for quantifying deformation behavior in metal forming processes. This capability serves as the cornerstone for fulfilling the research objective of this study, which seeks to comprehensively understand tribological phenomena at the interface by investigating the quantitative relationship between friction phenomena and deformation behavior.

1.3 Objective

Due to its high production rates, cost-effectiveness, and energy efficiency, the metal forming process is indispensable in modern manufacturing. In recent years, the demand for high-mix, low-volume manufacturing has increased within the metal forming industry and there is a growing need for high-quality metal forming products, as well as technology that can be produced at low cost. To meet these requirements and avoid surface defects effectively, a comprehensive understanding of tribological phenomena is essential. However, conventional friction models used to describe these phenomena mainly rely on empirical equations based on various assumptions, which often deviate from actual conditions. Therefore, exploring friction models based on the response of actual deformation behavior is crucial for a comprehensive understanding of tribological phenomena, serving as a major motivation and objective of this dissertation.

Additionally, the close correlation between tribological phenomena and deformation behavior, combined with the development of PIV techniques, makes it possible to explore the quantitative relationship between them. This exploration would serve as the cornerstone for achieving the research objectives of this study, ultimately enabling a comprehensive understanding of tribological phenomena at the interface. Specifically, the research objectives of this dissertation can be categorized into the following three aspects:

(1) Based on PIV analysis, propose a methodology to characterize deformation behavior, including both interface and bulk deformation, aiming to quantify the effects of tribological phenomena at the interface on deformation.
(2) Investigate the quantitative effects of tribological phenomena on metal plastic deformation and explore the feasibility of classic friction models in the actual metal forming process, enabling the proposal of more accurate friction models based on observed deformation behavior.
(3) Explore the quantitative relationship between tribological phenomena and deformation behavior, thereby enabling the quantification of stress distribution and establishing a quantitative evaluation method for tribological conditions at the sliding contact.

1.4 Outline of the dissertation

The dissertation is structured into six parts, with the first chapter serving as an introduction section. It provides a background overview to underscore the importance of tribological phenomena at the interface. Additionally, prior research is reviewed to ascertain the current state of the art in the fields of tribological phenomena, along with their interrelationship with deformation behavior. This chapter also offers a brief introduction to the motivation and objectives of the study.

In chapter 2, wedge indentation experiments are conducted as a model system to quantify deformation behavior and explore the distinct tribological phenomena at the interface by using PIV analysis. The chapter illustrates various deformation behaviors, such as velocity field and material flow under diverse conditions, demonstrating the potential of wedge indentation to reproduce the diverse deformation fields observed in plastic deformation and the capability of PIV analysis to capture the characteristics of severe plastic deformation, and also explain that existing friction models are inadequate for precisely describing the tribological phenomena, aiming to propose the feasibility of friction models based on observed deformation behavior.

In Chapter 3, building upon the characteristics of various plastic deformation fields and the influence of surface expansion on adhesion force outlined in Chapter 2, the surface expansion distribution is characterized and the quantitative relationship between adhesion phenomena and surface expansion behavior is proposed, with the aim of emphasizing the significance of the distribution of surface expansion ratio in quantifying adhesion stress distribution and understanding tribological phenomena at the interface.

In Chapter 4, attention is directed towards discussing the factors influencing the surface expansion distribution, a topic overlooked in Chapter 3. This chapter focuses on elucidating the effects of friction on plastic deformation in both metal surface and bulk, particularly addressing the factors contributing to the uneven distribution of surface expansion ratio. This correlation facilitates the proposal of a quantitative assessment of tribological conditions at the sliding contact. The aim is to achieve a comprehensive understanding of the correlation between tribological phenomena and deformation behavior.

In chapter 5, based on the quantitative relationship between tribological phenomena and deformation behavior discussed in Chapter 3 and 4, the friction models based on surface expansion distribution is developed, including the quantitative modeling of friction and normal stress distribution, aiming to describe the potential developments in the comprehension of tribological phenomena at the interface and the implications for engineering applications.

The final chapter of the dissertation presents the conclusions drawn from the study and identifies potential avenues for future research in this field.

Chapter 2 Deformation behavior and tribological phenomena in wedge indentation

2.1 General introduction

In metal forming processes, deformation behavior refers to how a metal material responds to external forces and undergoes changes in shape, including material flow, velocity field, strain and strain rate field. A comprehensive grasp of these deformation behaviors holds paramount importance in the exploration of tribological phenomena at the interface in the metal forming processes, facilitating the efficient attainment of desired outcomes [65]. This chapter establishes a model system that enables employing direct in-situ observations coupled with high-speed imaging and particle image velocimetry (PIV) techniques to reproduce and characterize diverse deformation behaviors and exploring the distinct tribological phenomena at the interface by using wedge indentation. Specifically, the deformation fields of different apex angle indenters are investigated and the relationship between the surface expansion behavior and adhesion force is discussed.

2.2 Experimental details

2.2.1 The determination of wedge indentation

The contact interfaces between tools/dies and materials in machining and forming processes differ significantly from conventional engineering sliding contacts. The tribological characteristics of these tool/die-material interfaces are critical in determining the performance of machining and forming operations, as they strongly influence the thermodynamic conditions at the interface. For instance, in metal cutting, severe friction and friction-induced deformation at the tool-chip interface result in the formation of a secondary shear zone (Fig. 2.1 (a)), leading to high cutting temperatures and forces [68]. This, in turn, affects energy consumption and surface quality. Similarly, in metal forming processes such as rolling, this friction-induced deformation—referred to as redundant deformation—occurs at the interface, as illustrated in Fig. 2.1 (b). This redundant deformation leads to non-uniform material flow and work-hardening, consumes additional energy, and can ultimately damage the surface of the workpiece [136].

Despite the critical importance of tribological phenomena and the deformation fields at these contact interfaces, predicting the nature of such severe contact conditions remains challenging. Traditional methods have proven inadequate for quantitatively investigating the deformation behavior at tool/die-material interfaces, largely due to the extreme difficulty in measuring these interactions [105, 118]. Therefore, the development of a new model system

capable of replicating the complex deformation fields at tool/die-material contact interfaces in metal processing is essential to better understand and predict the behavior of these tribological conditions.

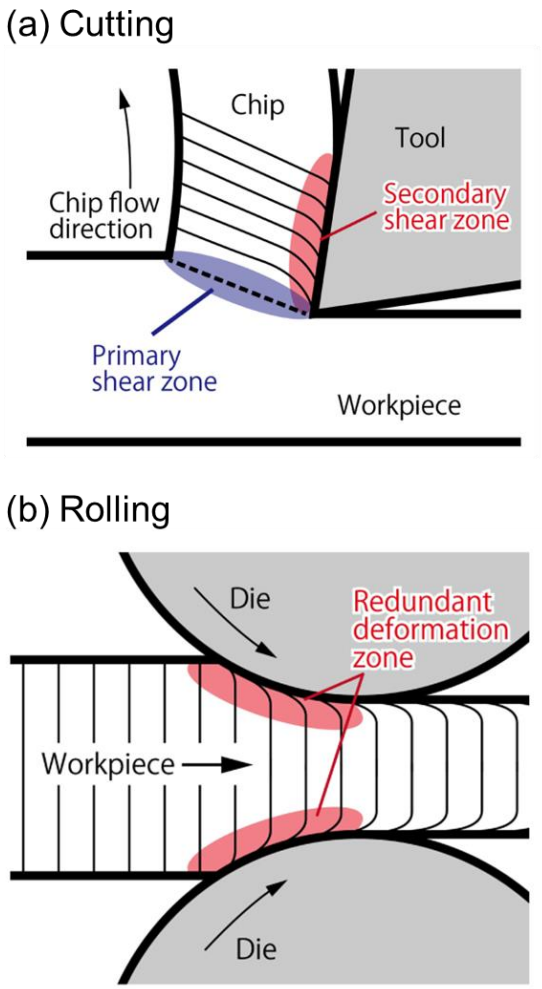

Fig. 2.1 Schematic of deformation characteristics in metal processing: (a) secondary shear zone in metal cutting and (b) redundant deformation zone in rolling [68]

Wedge indentation is commonly employed to assess the mechanical behavior of materials, as the indentation response is intricately linked with the deformation field [137]. This approach is founded on the similarity between the deformation field near the contact interface during indentation and the deformation fields observed in various plastic forming processes, thereby extending its applicability to diverse scenarios [138]. As depicted in Fig. 2.2, the schematic illustrates the deformation modes for narrow and wide wedge indenters, where shearing occurs with narrow-angle wedges (Fig. 2.2 (a)) and compression dominates with wide-angle

wedges (Fig. 2.2 (b)) [133]. By examining the friction phenomena and deformation behavior that develop during indentation, we can draw parallels to other complex material deformation processes, enhancing our understanding and prediction of material performance and tribological phenomena under different forming conditions. Thus, we utilize wedge indentation experiments as a model system to investigate the role of quantitative deformation behavior and its relationship with tribological phenomena at the interface.

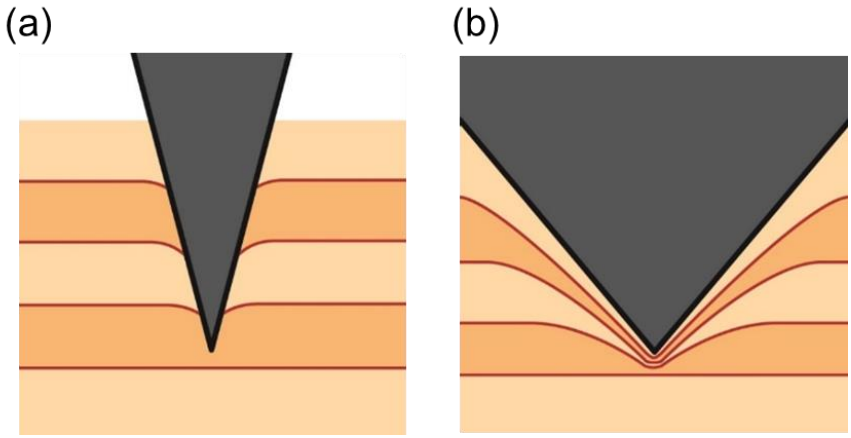

Fig. 2.2 Deformation mode in wedge indentation: (a) shearing with narrow-wedge indenter and (b) compression with wide-wedge indenter

2.2.2 Experimental setups and materials

Fig. 2.3 depicts the different angles of the indenter utilized for the experiment, all of which were constructed from high-speed steel. Experiments were conducted using indenters with angles of 30°, 60°, 90°, and 120°, respectively. By varying the wedge angle of the indenter, we could obtain and reproduce the diverse deformation fields observed in plastic deformation. The indentation experiment was performed using a machining center (FANUC ROBODRILL α-D14iA5).

Fig. 2.4 illustrates the experimental setup for force measurements. The indenter was securely affixed to the machining center using an attached vise, ensuring stability and precision during the experiment. The rotating part of the spindle section was immobilized to prevent any unintended movement. The workpiece material was positioned directly beneath the spindle section, ensuring proper alignment. The indenter was then moved to the appropriate distance to conduct the indentation experiments, allowing for controlled and accurate measurement of the forces involved.

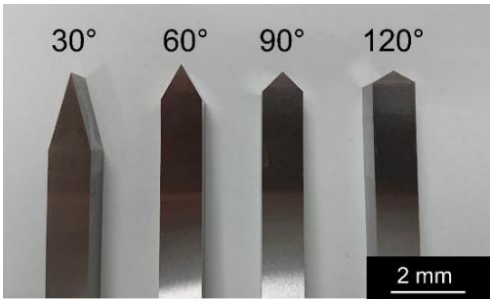

Fig. 2.3 Indenters with different apical angles (2α)

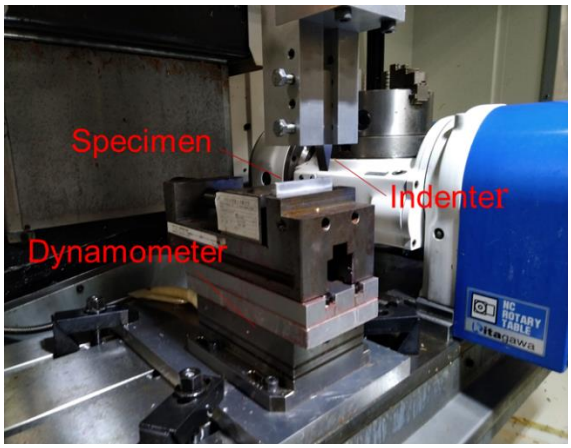

Fig. 2.4 Experiment setup for force measurements

Aluminum, a typical metallic material with diverse applications, undergoes significant deformation at the interface and displays pronounced adhesion during the indentation process, making it conducive to exploring the relationship between tribological phenomena and the deformation field [139]. Consequently, in this study, annealed aluminum (A1050P) was chosen as the workpiece material due to its well-documented mechanical properties and its relevance in practical applications. Table 2.1 provides the primary composition of A1050P, highlighting its suitability for detailed analysis of the deformation and adhesion behaviors observed during indentation experiments.

Table 2.1 Chemical composition ofA1050P

Chemical Composition %								
Al	Si	Fe	Cu	Mn	Mg	Zn	Ti	V
99.56	0.07	0.32	0.01	0.00	0.00	0.00	0.02	0.02

2.2.3 Experimental procedures

The experimental procedures for quantifying the effects of tribological phenomena on deformation behavior comprise two distinct experimental setups in this study. The first setup is devised for observing metal deformation through in-situ observations, while the second is dedicated to measuring indentation force to elucidate the relationship between deformation behavior and tribological phenomena. It is noteworthy that the setup for measuring force closely mirrors that of the in-situ observations, ensuring consistency in experimental conditions. Fig. 2.5 illustrates the schematic of the experimental setup for direct in-situ observations during indentation. To observe the plastic flow occurring within the material, a plane strain condition was ensured by clamping the specimen against a thick, transparent glass block, which restricts out-of-plane deformation and allows clear visualization of the deformation processes. This configuration enables detailed analysis of the material's response under controlled conditions, thereby facilitating a comprehensive understanding of the deformation mechanisms at play. Indentation was conducted at a constant speed (V_0) of 0.1 mm/s until the indenter reached a designated depth (D). Throughout this process, the indentation force in the vertical direction was measured using a piezoelectric dynamometer (Kistler 9272, natural frequency ~2 kHz), onto which the workpiece was mounted. Material flow was recorded in-situ through the glass block using a high-speed camera (Photron WX100), capturing images at 125 frames per second with a spatial resolution of 1 μm per pixel. The image sequences were analyzed via image correlation using PIV techniques to obtain quantitative deformation behavior in the vicinity of the indenters. Further details regarding PIV will be discussed in the subsequent section.

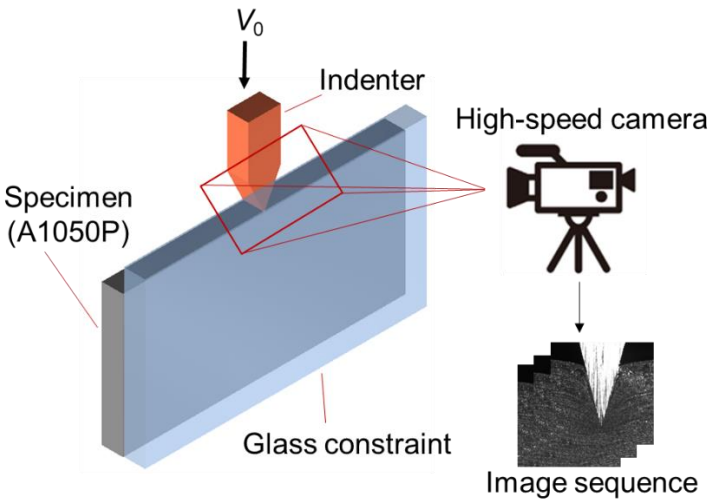

Fig. 2.5 Schematic of the experimental setup for in-situ observations

Fig. 2.6 depicts an example of the indenter motion and the corresponding change in force during the experiments. As illustrated in this figure, the force exhibits a linear increase during indentation (Fig. 2.6 (b)) and then reaching its peak at a given indentation depth, indicating a consistent penetration of the indenter into the specimen. This maximum force, expressed as the indentation force (F), represents the resisting force that impedes the indenter from penetrating and separating the material, resulting from the combined effects of friction force (F_f) and normal pressure (F_n) (see Fig. 2.7). Their relationship with the indenter angle can be expressed as:

$$\frac{F}{2} = F_f cos\alpha + F_n sin\alpha \tag{2.1}$$

The friction force at the indenter-material interface acts as the primary resistance preventing the penetration of the indenter, concurrently causing shear deformation at the contact surface. Conversely, normal pressure is the main driver of compressive effects, particularly causing the accumulation or compression of the material. Due to the symmetrical shape of the indenter, directly measuring the friction force and normal force separately is unfeasible. By varying the indenter angle, we can reproduce different tribological conditions affecting deformation behavior. Specifically, using a relatively narrow-angle indenter in experiments allows for exploring the relationship between interface friction and deformation behavior. This is because the normal component of the normal force on the indenter surface is comparatively small compared to the normal component of the friction force due to the smaller apical angles (Eq. 2.1). On the other hand, a wider-angle indenter makes it possible to investigate the effects of normal pressure on the deformation field.

After stopping for 1 second, the indenter is extracted from the specimen (Fig. 2.6 (c)). During the extraction (Fig. 2.6 (d)), the force is directed opposite to the indentation direction. This force should match the adhesion force at the interface when the material is being pressed in, as both forces result from the interface adhesion between the indenter and the specimen, albeit in opposite directions. Therefore, in this study, this maximum negative force was assessed as the adhesion force (F_a). It is noteworthy that the glass block was removed during the measurement of the indentation force and adhesion force to mitigate the influence of friction between the glass and indenter, ensuring that the measured force accurately reflects the true adhesive interactions. The filming and indentation conditions, including parameters such as indenter angle and indentation speed, are presented in Tables 2.2 and 2.3, respectively, providing a comprehensive overview of the experimental setup and conditions.

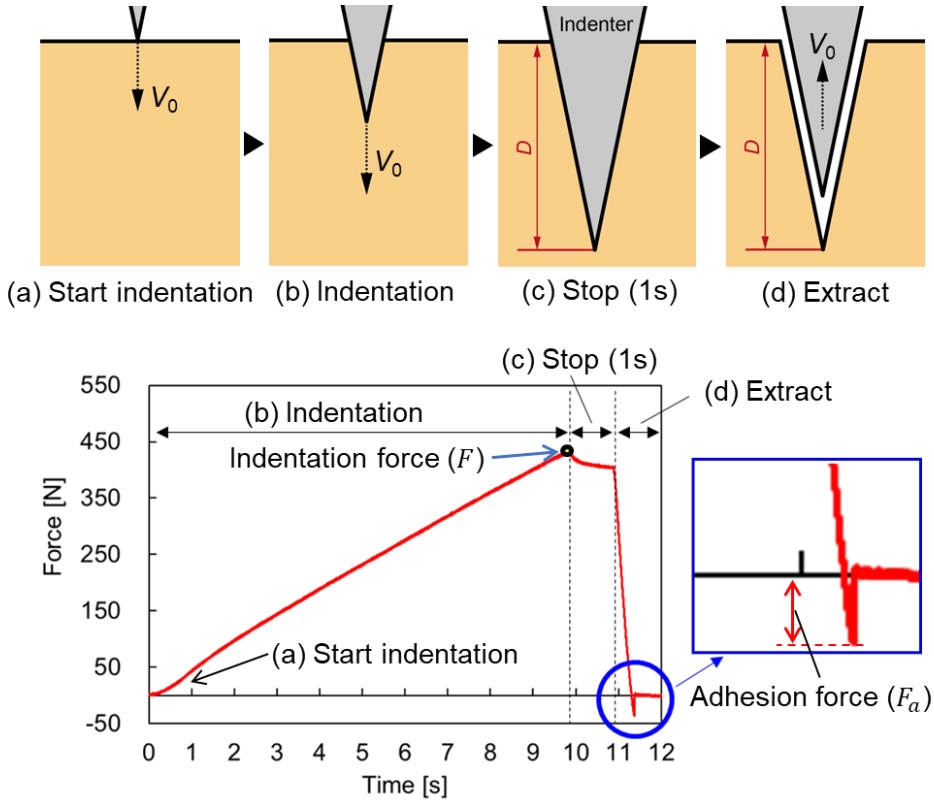

Fig. 2.6 Procedure for measuring adhesion force

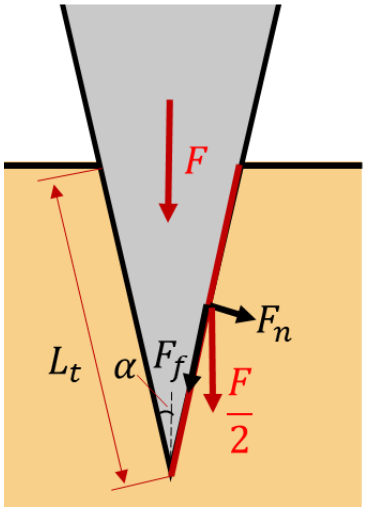

Fig. 2.7 The relationship between each force component

Table 2.2 Filming conditions

Pixel number	2048x2048 (2.048 mm x 2.048 mm)
Shutter speed	125 fps

Table 2.3 Indentation conditions

Workpiece	A1050P
Indenter angle	30°, 60°, 90°, 120°
Indentation speed	0.1 mm/s
Indentation depth	0.5, 1.0, 2.0, 3.0, 4.0, 5.0 mm

2.2.4 The details of PIV

PIV has traditionally been employed to measure two-dimensional velocity fields in macroscopic fluid flows. The fundamental principle of PIV involves correlating successive image frames by tracking specific features in each [140]. Specifically, to visualize the flow, particles are seeded into the fluid and photographed at two distinct times. The resulting images are divided into numerous smaller regions called interrogation regions, as depicted in Fig. 2.8. Particle tracking typically relies on analyzing sequences of photographic images captured of the moving fluid. The motion of particle groups within an interrogation region is determined using a statistical technique known as cross-correlation. If the array of gray values in the first image is denoted as $f_k(i,j)$ and the second image as $g_k(i,j)$, the cross-correlation, $\emptyset_k(m,n)$, is calculated as follows:

$$\emptyset_k(m,n) = \sum_{j=1}^{q}\sum_{i=1}^{p} f_k(i,j) \cdot g_k(i+m, j+n) \tag{2.2}$$

where the k^{th} interrogation region is in a certain region of size p x q pixels in the digital image. This calculation identifies the displacement of particles by determining the peak of the cross-correlation function, which corresponds to the most probable displacement vector within the interrogation region. This method allows for precise measurements of velocity fields by analyzing the shifts in particle positions between consecutive frames. To expedite the calculation of velocity vectors, the application of Fast Fourier Transform (FFT) within the interrogation region can significantly reduce computation time [141].

In the present model system, image sequences of the indentation were captured using a high-speed camera. Subsequently, specific feature points in each frame were tracked through PIV analysis. By identifying the same feature point in two successive image frames, the incremental displacement between frames was computed using spatial averaging [142]. This procedure of determining displacement was repeated for the entire set of grid elements, thereby generating a displacement field for the entire imaged region, which in our study was the area around the indenter. This comprehensive displacement field enabled the calculation of deformation behaviors

such as material flow and velocity field. The detailed steps of the computational process, including FFT application for efficiency, were implemented using MATLAB. Fig. 2.9 depicts the flowchart schematic describing the computation of flow and deformation parameters, illustrating the methodology from image acquisition to final data analysis [133].

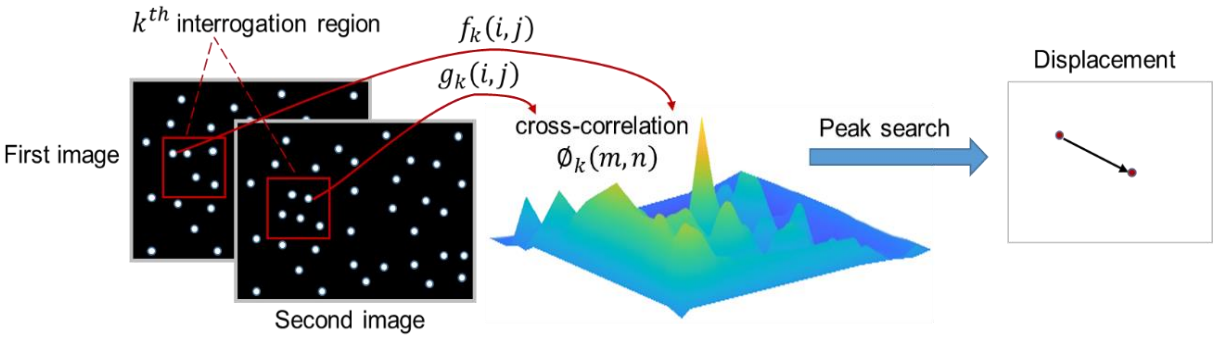

Fig. 2.8 The illustration of an interrogation region and cross-correlation

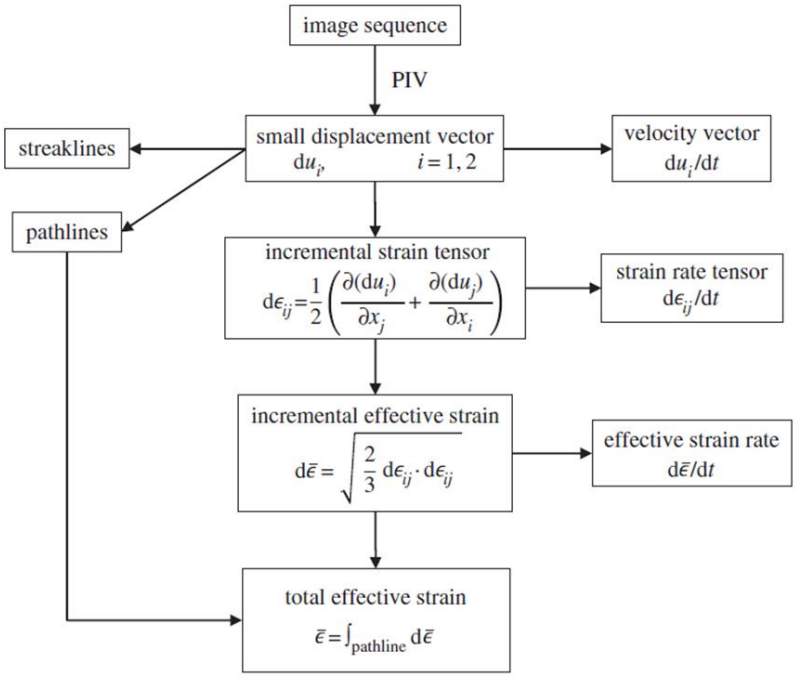

Fig. 2.9 The flowchart schematic of PIV analysis

2.3 Deformation behavior and tribological condition in wedge indentation

2.3.1 Deformation field under varying angle of indenters

We conducted wedge indentation experiments as a model system lying in its abilities to reproduce diverse deformation field by simply varying indenter angles and Figs. 2.10 (a-d) depict the velocity maps derived from the PIV analysis, showcasing both the vertical (V_v) and horizontal (V_h) components for indenter angles of 30° (30 deg), 60° (60 deg), 90° (90 deg), and 120° (120 deg), respectively to demonstrate the effectiveness of this indentation configuration. For the 30-degree indenter (Fig. 2.10 (a)), material flow predominantly occurs in the vertical direction within the region proximal to the indenter face due to interfacial friction and the horizontal velocity field indicates that material movement in the lateral direction is concentrated near the indenter tip. It resembles the deformation seen near the edge of a tool in metal cutting by sharp wedges or in the splitting of wood, where the material separates towards both sides. This similarity reinforces the appropriateness of the term "cutting" for the action of the indenter [133]. Furthermore, for the 60-degree indenter (Fig. 2.10 (b)), material flow in the vertical direction resembles that of the 30-degree indenter, being primarily confined to the region proximal to the indenter surface. However, the horizontal velocity field reveals significant material flow in the lateral direction, likely due to the material being pushed outward by the wider indenter. As a result of the geometric relationship, increasing the indenter angle will inevitably amplify the normal pressure component during indentation (see Eq. 2.1). This suggests that a wider indenter angle not only induces cutting-like deformation near the indenter tip but also promotes broader material displacement due to enhanced compressive forces, namely normal pressure.

On the other hand, for the 90-degree and 120-degree indenter (Figs. 2.10 (c-d)), the vertical velocity of the workpiece beneath the indenter is nearly equal to the indentation velocity, indicating this region of the workpiece material is stationary with respect to the indenter. Specifically, as the material is subjected to compressive forces, regions near the contact interface can undergo significant plastic deformation. This severe deformation can result in work hardening, which reduces the material's capacity for further deformation, contributing to the formation of the "zero velocity" zone. This "zero velocity" zone, also defined as the dead metal zone [143], is significantly more pronounced under the 120-degree indenter (Fig. 2.10 (d)), indicating that this zone of material moves integrally with the indenter. In this sense, it acts as an extension of the indenter [134].

To further illustrate the characteristics of the deformation field under the 120-degree indenter, Fig 2.11 depicts the development of the vertical velocity field over time. In this figure, the velocity field is divided into three regions: a dead metal zone (Region 1) that acts as an extension of the indenter, a transitional zone (Region 2) with a velocity of about 0.06 mm/s, and

Region 3, located away from the indenter, where the material velocity is essentially zero. As shown in the figure, the dead metal zone (Region 1) expands significantly over time due to the effects of strain hardening, which impact the further deformation of the material during this process. This also explains why the deformation field in Region 2 decreases over time, as strain hardening makes it more difficult for further slip to occur. These results clearly demonstrate the capability of wedge indentation to reproduce diverse deformation behaviors.

In metal forming processes, deformation modes pertain to the diverse methods through which a material undergoes reshaping or deformation. Common deformation modes encountered in metal forming encompass compression, tension, bending, shearing, or cutting [144]. During indentation, the workpiece material is mainly subjected to the friction force and normal pressure. The material flow induced by the interface friction is usually shearing or separating material, just like the cutting action of the indenter [145]. Clearly, under narrow-wedge indentation, the deformation field corresponds to the cutting mode. On the other hand, material flow induced by the normal pressure often compressing or accumulating the material, and the region of deformation area under the compression effects exists near almost all the contact surface [146], corresponding to deformation field under wide-wedge indentation. These results indicate a transition from the cutting mode to the compression mode with increasing indenter angles, highlighting the potential of wedge indentation in reproducing multiple deformation fields.

This potential can also be manifested by the flow of grid patterns and Fig. 2.12 shows an image sequence of 30 deg indenter with superimposed grid line from PIV captured at different time intervals. The grid patterns for 30 deg indenter reveal noticeable surface expansion, namely surface enlargement near the indenter tip after indentation [72]. By examining points A_0 and A_1 at different frames, it becomes evident that the workpiece is predominantly stretched towards the region proximal to the indenter face. Fig. 2.13 shows the material flow lines with 30°, 60°, 90°, and 120° indenters respectively. In the case of the 60° indenter (Fig. 2.13 (b)), the grid lines resemble those observed with the 30° indenter (Fig. 2.13 (a)), albeit with less material separation near the indenter. Conversely, for the 90° and 120° indenters (Figs. 2.13 (c-d)), the material flow becomes more diffuse, with minimal observed separation, indicating compression rather than separation of the workpiece. Considering points A_0 and A_1, B_0 and B_1, C_0 and C_1, D_0 and D_1, situated closely at the onset but exhibiting distinct movement during indentation, distinctly highlights the transitional behavior with increasing indenter angle.

In summary, the grid and velocity fields clearly indicate the transition from cutting mode to compression mode with the increase of the indenter angle, suggesting the significant potential of wedge indentation to reproduce diverse deformation behaviors.

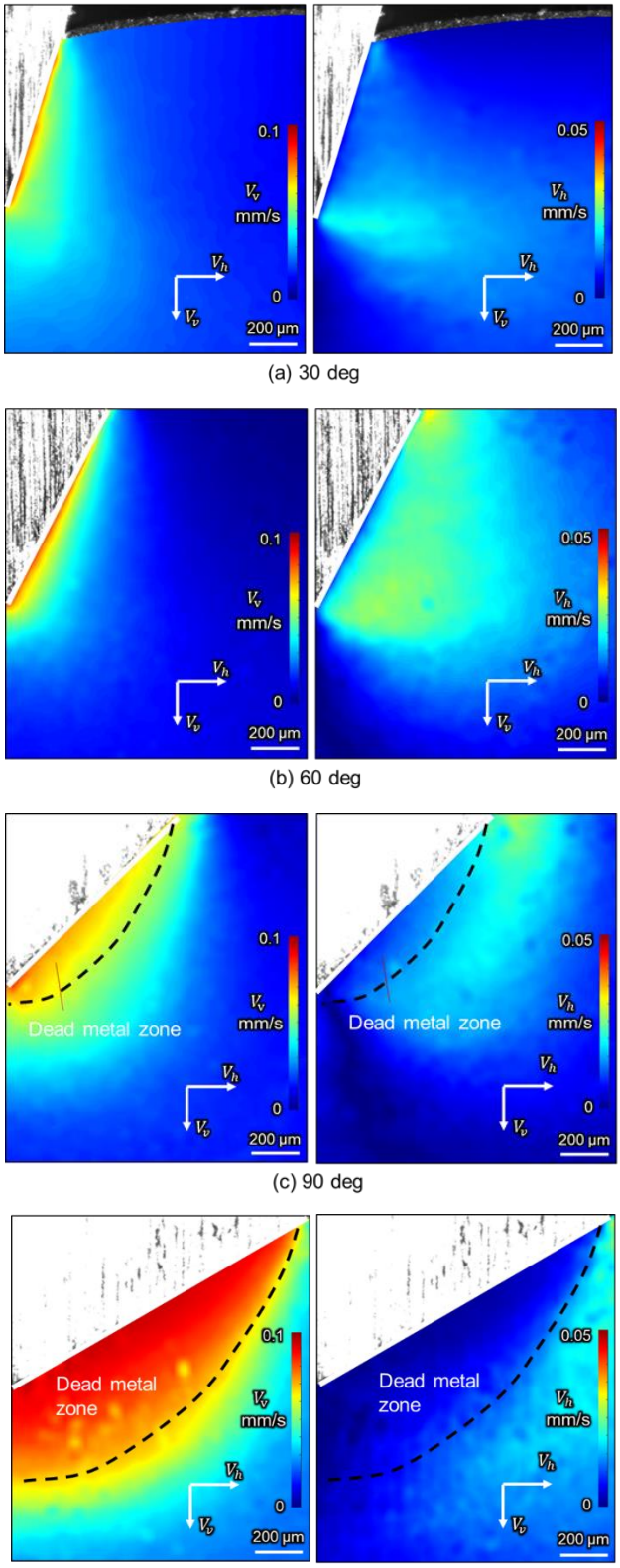

(a) 30 deg

(b) 60 deg

(c) 90 deg

(d) 120 deg

Fig. 2.10 Velocity maps derived by PIV analysis, showing the vertical (V_v: left) and horizontal (V_h:right) components

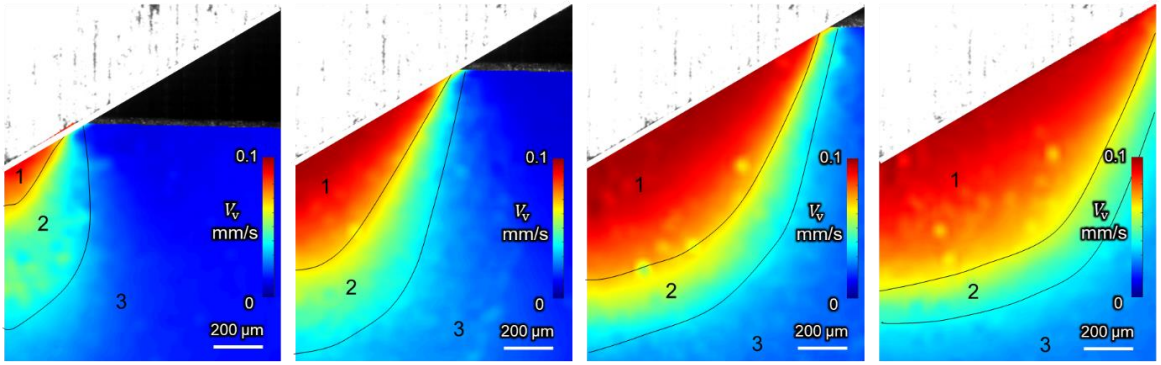

(a) $t = t_0 + 2.5$ s (b) $t = t_0 + 5$ s (c) $t = t_0 + 7.5$ s (d) $t = t_0 + 10$ s

Fig. 2.11 The development of velocity field for the 120 deg indenter

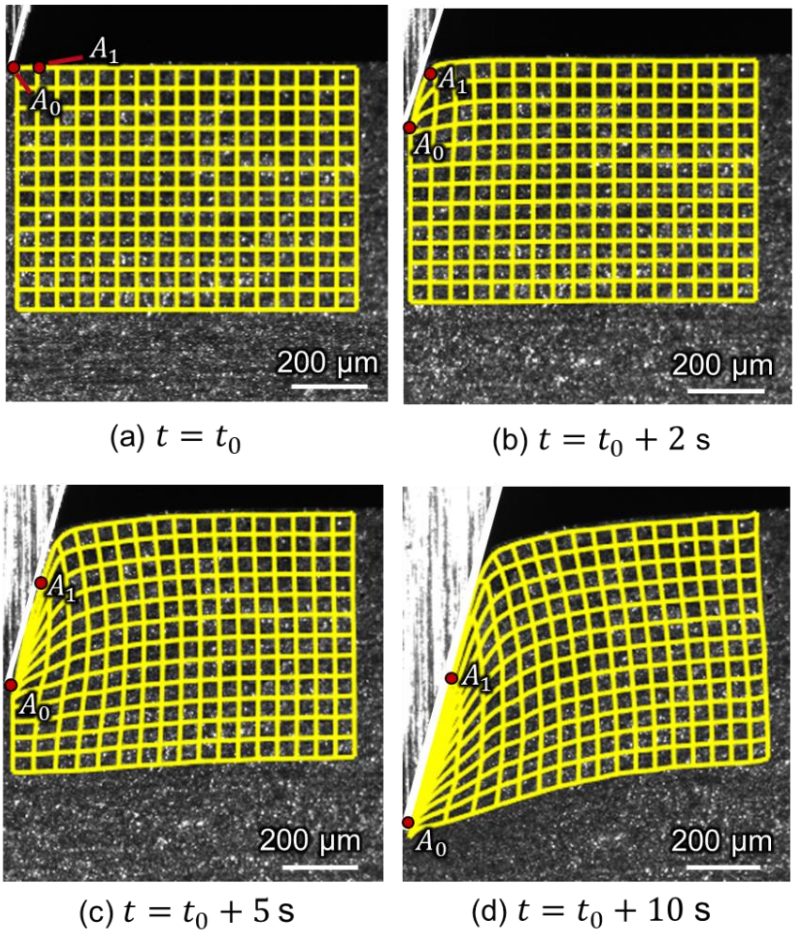

(a) $t = t_0$ (b) $t = t_0 + 2$ s

(c) $t = t_0 + 5$ s (d) $t = t_0 + 10$ s

Fig. 2.12 An image sequence of 30 deg indenter

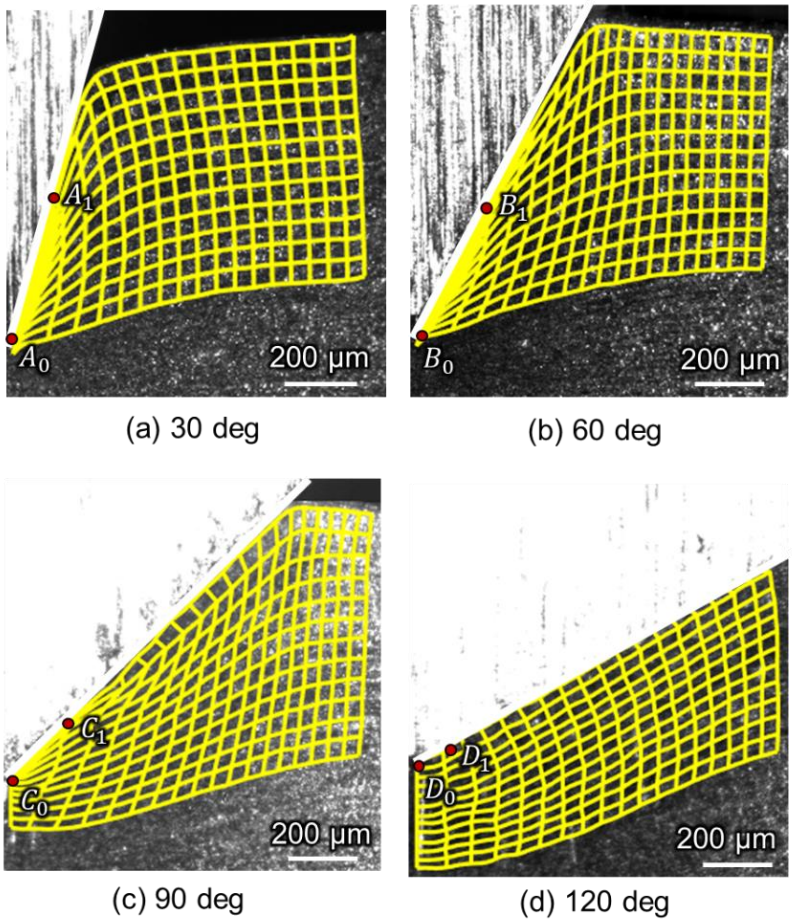

Fig. 2.13 The material flow lines with (a) 30 deg, (b) 60 deg, (c) 90 deg and (d) 120 deg indenter

2.3.2 Limitations of conventional friction models in wedge indentation

The complete understanding of tribological phenomena at the interface remains underdeveloped due to the complexity of the die-workpiece contact. This complexity arises because the tool/die-material interfaces in metal forming processes are subjected to severe frictional conditions, particularly near the tool edge, which is typically associated with high normal pressure. High normal pressure generally results in increased friction force. These tribological phenomena have been demonstrated and described in several friction models, such as the Wanheim-Bay friction model [58] and the mixed Coulomb-sticking friction model, also known as the sticking-sliding friction model [147].

Previous section proves distinct material flow modes between narrow and wide angle indenter, specifically the compression mode for the 120-degree indenter and the cutting mode for the 30-degree indenter. To show the difference of tribological condition at the interface between these two indenters, indentation experiments were conducted to measure the indentation force and

adhesion force with the indentation depth of 1 mm by using 30 deg and 120 deg indenters.

Fig. 2.14 compares the indentation force and adhesion force between the 30-degree and 120-degree indenters. As shown in the figure, the indentation force for the 120-degree indenter is significantly higher than that for the 30-degree indenter. Since the indentation force (F) arises from the combined effects of friction force (F_f) and normal pressure (F_n) (Eq. 2.1) and the proportionality of normal pressure increases with increasing indenter angle, the normal pressure for the 120-degree indenter is largely higher compared to the 30-degree indenter, while the adhesion force for the 120-degree indenter is considerably smaller. According to the traditional pressured-based friction models, like Wanheim-Bay friction model and sticking-sliding friction model, the adhesion force should increase with higher pressure. However, this result shows the opposite trend, which clearly contradicts existing friction models. This outcome indicates that existing friction models are inadequate for precisely describing these tribological phenomena occurring at the interface under current indentation configuration and material properties.

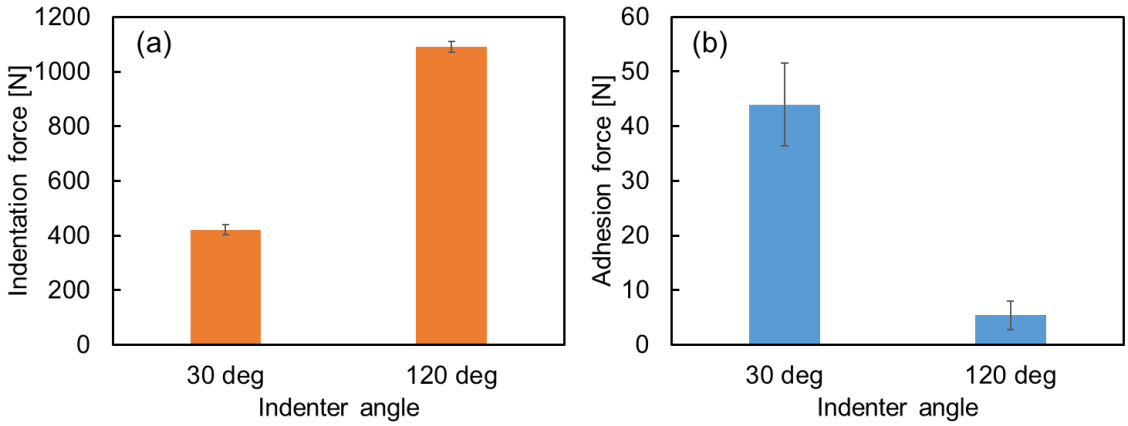

Fig. 2.14 The comparison of (a) indentation force and (b) adhesion force between 30 deg and 120 deg indenters

The different tribological phenomena observed between distinct deformation modes may result from variations in surface expansion behavior. Fig. 2.15 schematically illustrates surface expansion behavior during indentation. As shown in this figure, the surface enlargement decreases with increasing indenter angle, leading to less amount of surface expansion. Consequently, a smaller amount of nascent surface is generated, resulting in a lower adhesion force for wider-angle indenters. These results underscore the critical role of nascent surface generation, specifically the surface expansion parameter following indentation, in determining the magnitude of the adhesion force. This insight highlights the importance of considering surface expansion behavior to understand and control adhesion phenomena during indentation processes.

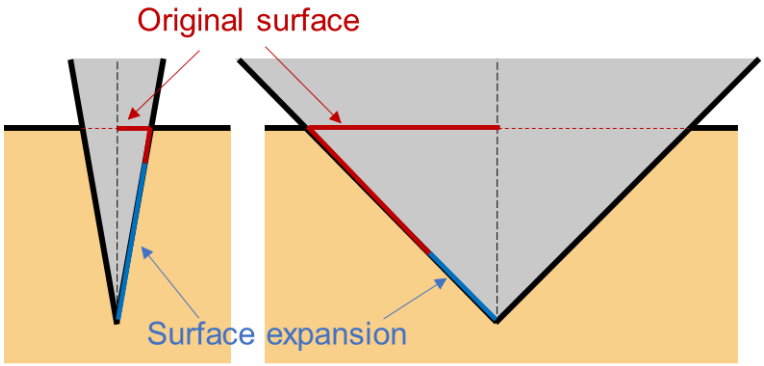

Fig. 2.15 The schematic of surface expansion behavior during indentation with the increasing indenter angle

2.3.3 Influence of surface expansion on adhesion force

It is recognized that the adhesion force is closely linked with surface deformation, which generates a chemically active nascent surface, with surface expansion serving as a representative factor [43]. Previous section proposed that surface expansion significantly influences the magnitude of the adhesion force and existing friction models are inadequate for precisely describing these tribological phenomena during indentation mainly due to variations in surface expansion behavior. Therefore, to assess the impact of surface expansion of the deformed material on the adhesion force at the indenter-material interface, two parameters were defined: surface expansion amount ΔA and surface expansion ratio ϕ. The surface expansion amount ΔA represents the difference between the original surface area of the undeformed specimen and the surface area after stretching due to the indentation process. In the wedge indentation experiment configuration, the surface expansion ΔA per unit length of the specimen width is calculated using the following equation:

$$\Delta A = (L + \Delta L) - L = \frac{D(1 - sin\alpha)}{cos\alpha} \tag{2.3}$$

where D is the indentation depth, and 2α is the indenter angle, as shown in Fig. 2.16. Eq. 2.3 indicates that ΔA differs with the indentation depth and indenter angle.

The surface expansion ratio ϕ is the ratio of the surface expansion amount ΔA to the original surface area of the undeformed specimen, and is expressed as follows:

$$\phi = \frac{\Delta L}{L} = \frac{1 - sin\alpha}{sin\alpha} \tag{2.4}$$

Note that the surface expansion ratio ϕ expressed by this equation represents the average surface expansion across the entire deformed surface, which is a “macroscopic” surface expansion ratio. Eq. 2.4 demonstrates that the macroscopic surface expansion ratio does not depend on the indentation depth; rather, ϕ is solely influenced by the indenter angle in the present experimental configuration.

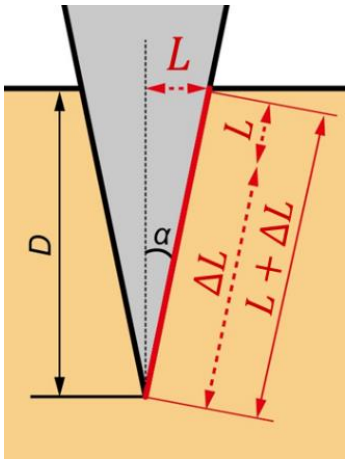

Fig. 2.16 Schematic of wedge indentation

To explore the relationship between surface expansion and adhesion force, we initially conducted indentation experiments to measure adhesion force using various degree indenters with identical surface expansion amounts under the conditions outlined in Table 2.4, in accordance with Eq. 2.3 and Eq. 2.4. Fig. 2.17 shows the relationship between the indenter angle, adhesion force, and surface expansion ratio ϕ. As shown in this figure, the adhesion forces for each indenter vary depending on the indenter angle even with the same surface expansion amount ΔA and the adhesion force is the greatest for the indenter with an indenter angle of 30°, indicating that surface expansion amount is not equal to the nascent surface generated. This is because the aluminum oxide layer stretches in association with the stretching of the bulk aluminum under the conditions of low macroscopic surface expansion ratio ϕ, and the freshly generated nascent surface, which is chemically active and causes a strong adhesion at the interface, is not formed until the macroscopic surface expansion ratio ϕ reaches a certain value, as shown in Fig. 2.18. This result clearly confirms that the exposure of the freshly generated nascent surface and subsequent interface adhesion should be evaluated not by the surface expansion amount ΔA but by the macroscopic surface expansion ratio ϕ. This finding is strongly supported by the result that the magnitude of the macroscopic surface expansion ratio ϕ for each indenter is consistent with the magnitude of the adhesion force.

Table 2.4 Experimental conditions for four indenters

Indenter angle 2α (deg)	30	60	90	120
Indentation depth D (mm)	1.00	1.33	1.85	2.86
Surface expansion amount ΔA (mm^2)	1.53	1.53	1.53	1.53
Surface expansion ratio ϕ $(-)$	2.86	1.00	0.41	0.15

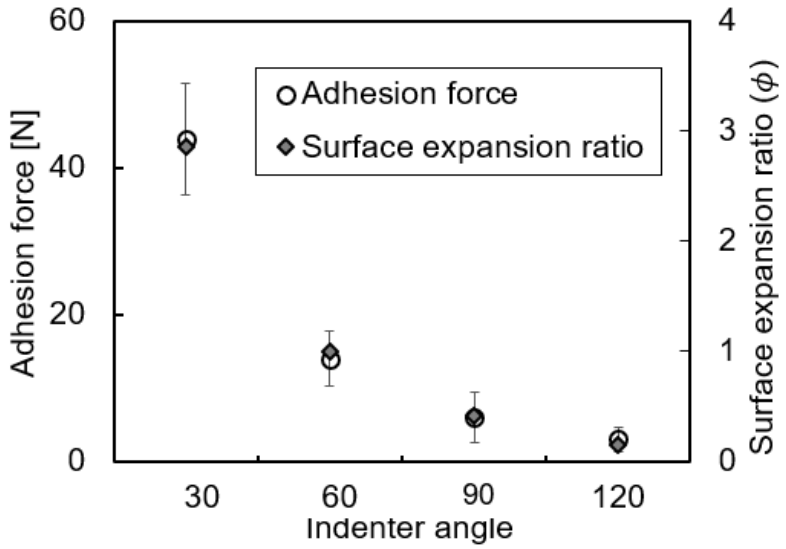

Fig. 2.17 Adhesion force and surface expansion ratio for each indenter

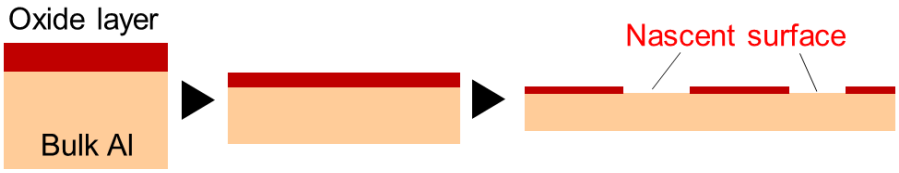

Fig. 2.18 Schematic of exposure of nascent surface

To further explore the relationship between the macroscopic surface expansion ratio and adhesion force, the specific adhesion force is plotted as a function of indentation depth for the indenter with an indenter angle of 30° (Fig. 2.19). Note that the specific adhesion force indicates the adhesion force divided by the indentation depth and the macroscopic surface expansion ratio, as defined in Eq. 2.4, is independent of the indentation depth and determined only by the indenter angle. If the magnitude of the macroscopic surface expansion ratio ϕ truly determines the magnitude of the adhesion force (Fig. 2.17), the specific adhesion force should not differ depending on the indentation depth for the same macroscopic surface expansion ratio. However, as shown in this figure, the specific adhesion force increases with increasing indentation depth, even with the same macroscopic surface expansion ratio ϕ. These results indicate that although

the macroscopic surface expansion ratio reasonably reproduces the magnitude of the adhesion force, it is inadequate to precisely explain or describe the interface adhesion phenomena. This suggests that additional factors, beyond the macroscopic surface expansion ratio, contribute to the adhesion force, necessitating a more detailed examination of the microscopic interactions at the interface.

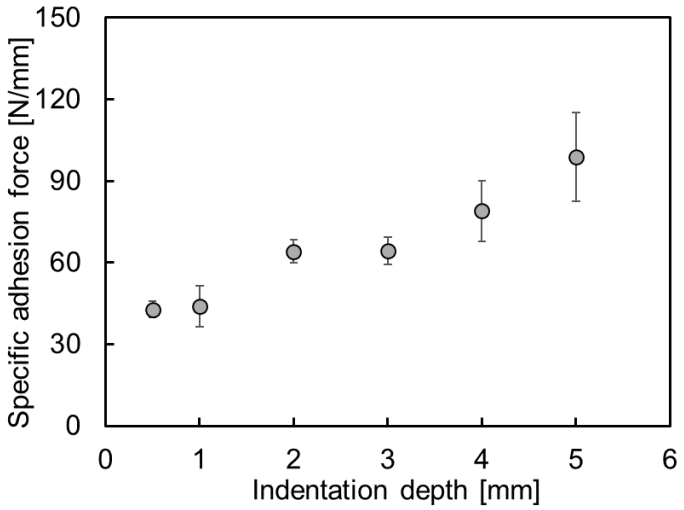

Fig. 2.19 Relationship between specific adhesion force and indentation depth

2.4 Summary

Deformation behavior observed at contact surfaces plays a fundamental role in the tribological behavior, and this behavior is highly correlated with tribological phenomena in machining or forming processes. In this chapter, our focus was on investigating the deformation behavior of different apex angle indenters and exploring the relationship between the surface expansion behavior and adhesion force. The main conclusions are summarized as follows:

(1) Wedge indentation has significant potential to reproduce diverse deformation behaviors. Specifically, material flow is primarily confined to the region near the indenter surface when employing a narrower indenter angle, attributable to interface friction. Conversely, with a wider indenter angle, the material moves collectively with the indenter due to compression deformation behavior. These findings suggest a transition from the cutting mode to the compression mode as the indenter angle increases.

(2) The comparison of the indentation force and adhesion force between the 30-degree and 120-degree indenters indicates that existing friction models are inadequate for precisely describing these tribological phenomena under current indentation configuration. These

distinct tribological phenomena may result from variations in surface expansion behavior, which correlates with the nascent surface area as the indenter angle increases.

(3) The macroscopic surface expansion ratio is qualitatively consistent with the magnitude of the adhesion force at the contact surface compared to the surface expansion amount, but it is inadequate to describe the interface adhesion phenomena precisely. These findings suggest that surface expansion behavior holds significant potential for further exploration of the effects of adhesion phenomena and necessitates a more detailed examination of the microscopic interactions at the interface.

Chapter 3 The correlation between adhesion phenomenon and surface expansion behavior

3.1 General introduction

Previous chapter demonstrated that while the macroscopic surface expansion ratio can reasonably indicate the magnitude of the adhesion force, it is not sufficient to comprehensively describe the interface adhesion phenomenon. This highlights the need for a more detailed examination of the microscopic interactions at the interface. The challenge, therefore, lies in obtaining the microscopic surface expansion ratio, as quantitatively investigating interface deformation is extremely difficult [103]. Hence in this chapter, direct in-situ observations coupled with high-speed imaging and PIV techniques were employed to capture and characterize the distribution of microscopic surface expansion, namely surface expansion distribution defined in this study, at the contact surface. By using single-groove indenters, the quantitative relationship between the surface expansion distribution and adhesion force was examined and the friction model for adhesion stress distribution was proposed.

3.2 Surface expansion behavior in wedge indentation

3.2.1 The procedure for obtaining surface expansion distribution

The preceding discussion has underscored the intimate connection between adhesion force and surface expansion ratio. However, as depicted in Fig. 2.19, it becomes evident that the macroscopic surface expansion ratio fails to precisely characterize the interface adhesion phenomenon. This observation prompts a deeper inquiry into the relationship between adhesion force and microscopic expansion ratio, specifically focusing on the distribution of microscopic surface expansion ratio along the deformed surface, which is defined as the surface expansion distribution in our research. The previous chapter demonstrates that the wedge indentation experiments and PIV analysis effectively capture the characteristics of severe plastic deformation. This capability enables the characterization of the surface expansion distribution at the contact surface. By applying the PIV analysis, the surface expansion distribution $\phi(x)$ was obtained by the following procedure:

(1) Plot virtual tracking markers at regular intervals of l on the metal surface (Fig. 3.1 (a)).
(2) Obtain the position of the tracking marker P_n from the indenter tip (x_n) and the distance between virtual tracking markers P_n and P_{n+1} ($l + \Delta l_{n\_n+1}$) during the indentation process (Fig. 3.1 (b)).
(3) Calculate the midpoints x_{n_n+1} and the local surface expansion ratio ϕ_{n_n+1} between the

tracking markers P_n and P_{n+1} based on the following equation:

$$x_{n\_n+1} = \begin{cases} 0 & (n = 0) \\ \frac{x_n + x_{n+1}}{2} & (n > 0) \end{cases} \tag{3.1}$$

$$\phi_{n\_n+1} = \frac{\Delta l_{n\_n+1}}{l} \tag{3.2}$$

(4) Obtain the distribution of the surface expansion ratio $\phi(x)$ for the local surface expansion ratio at the point x_{n_n+1} as ϕ_{n_n+1}(Fig. 3.1 (c)).

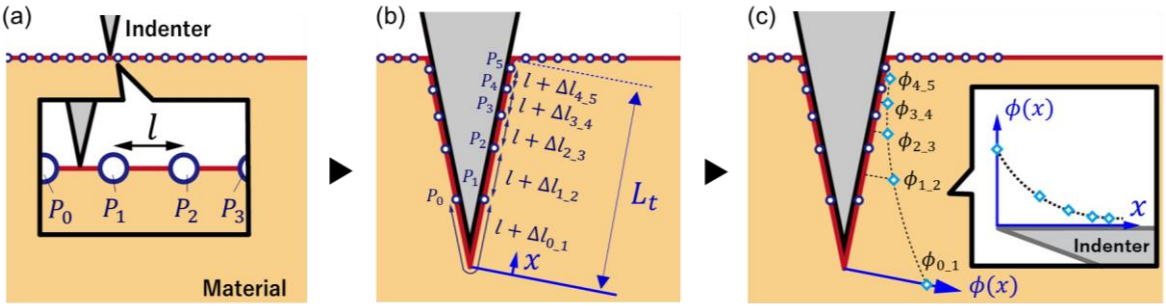

Fig. 3.1 Procedure for obtaining distribution of surface expansion ratio $\phi(x)$

3.2.2 The results of surface expansion distribution in wedge indentation

Fig. 3.2 and Fig. 3.3 show the images of 30 deg and 120 deg indenters with superimposed virtual tracking markers ($l = 12.0$ μm) before and after indentation ($D = 1.0$ mm) respectively, indicating that the virtual tracking markers successfully reproduce the local surface expansion along the indenter face under distinct deformation fields. Note that, in Figs. 3.2 and 3.3, the markers are highlighted every five points to clearly show the movement and positional relationship of each tracking marker. As shown in Fig. 3.2, the movement of each tracking point along the indenter face for the 30-degree indenter varies considerably and the distance between the two successive tracking points becomes particularly pronounced near the indenter tip, indicating significant nascent surface generation in this region. In contrast, the tracking points for the 120-degree indenter move integrally with the indenter (Fig. 3.3), with little or no surface enlargement. Evidently, these distinct surface expansion behaviors associated with nascent surface generation are closely related to the interface adhesion phenomena (see Fig. 2.18). This visualization helps in understanding the local deformations and their contributions to the overall adhesion force, thereby providing a more detailed and accurate depiction of the interface adhesion phenomena.

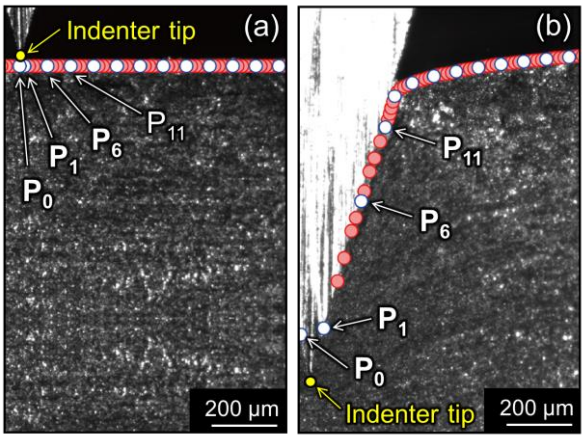

Fig. 3.2 Virtual tracking markers (a) before and (b) after indentation process for 30 deg indenter

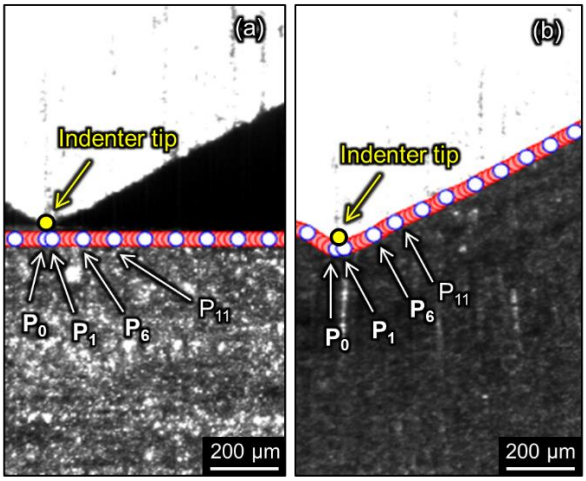

Fig. 3.3 Virtual tracking markers (a) before and (b) after indentation process for 120 deg indenter

Fig. 3.4 shows the comparison of surface expansion distribution $\phi(x)$ along the side face of the indenter between 30 deg and 120 deg indenter at indentation depths of 1.0 mm. Note that the origin in this figure represents the indenter tip. Additionally, the values of x_{n_n+1} and ϕ_{n_n+1} in this figure are the averages of values obtained from eight different experiments (see Fig. 3.1). As illustrated in this figure, the surface expansion ratio for 120 deg indenter along the interface is nearly zero, i.e., there is almost no new nascent surface generated. This clearly explains why the adhesion force of 120 deg indenter is significantly smaller than that of 30 deg indenter, since the adhesion force is highly related to the nascent surface that is chemically active.

Clearly, under narrow-wedge indentation, the workpiece material undergoes higher adhesion force and more severe localized surface expansion near the indenter edge, which facilitates a more detail discussion on the relationship of surface expansion distribution and adhesion force for the 30-degree indenter.

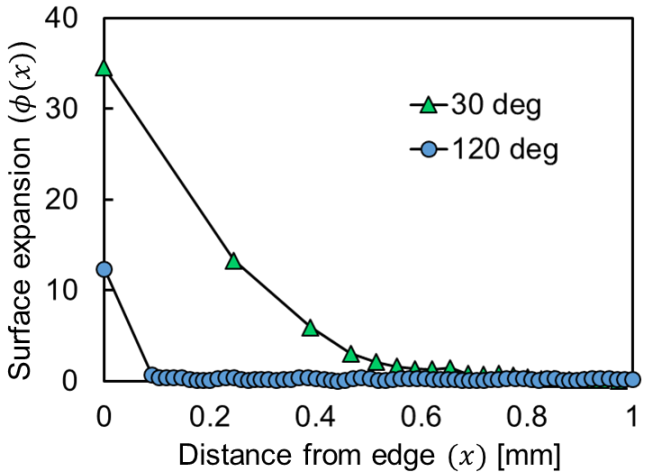

Fig. 3.4 The comparison of surface expansion distribution $\phi(x)$ along the side face of the indenter between 30 deg and 120 deg indenter at indentation depths of 1.0 mm

3.3 Influence of surface expansion distribution on adhesion force

To investigate the relationship between surface expansion distribution and adhesion force for the 30-degree indenter across a wide range of spatial variation, we obtained the surface expansion distribution at different depths (see Fig. 3.1) and Fig. 3.5 presents the surface expansion distribution, $\phi(x)$ at indentation depths of 0.5, 1.0, 1.5, and 2.0 mm. As shown in this figure, the surface expansion ratio is not uniform along the indenter face, and the localization of surface expansion in the vicinity of the indenter tip is evident. This non-uniform distribution highlights the importance of considering local variations in surface expansion when analyzing adhesion phenomena, as localized areas of high surface expansion may exert a disproportionate influence on the overall adhesion force. Specifically, localized and large surface expansion ratios inevitably create more new surfaces, thereby influencing the amount of adhesion experienced at the interface.

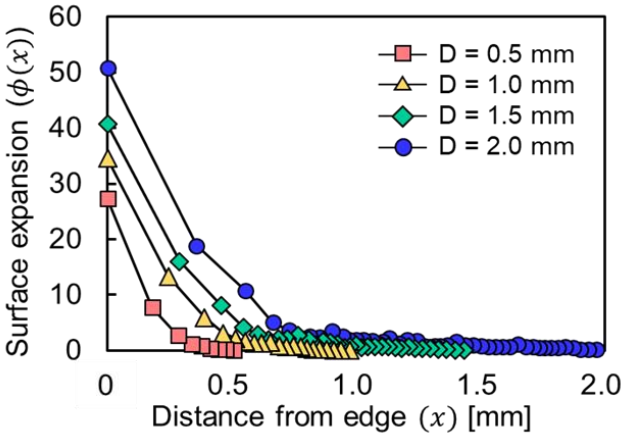

Fig. 3.5 Distribution of surface expansion ratio $\phi(x)$ for each indentation depth

On the other hand, larger indentation depth inevitably increases the value of the micro surface expansion ratio near the indenter tip for each point. Therefore, to mitigate the influence of the variation in indentation depth on the indenter face at each point, the sliding distance $L_s(x)$ and normalized surface expansion ratio distribution $\phi'(x)$ were defined as follows:

$$L_s(x) = L_t - x = \frac{D}{\cos\alpha} - x \tag{3.3}$$

$$\phi'(x) = \frac{\phi(x)}{L_s(x)} \tag{3.4}$$

where L_t is the length of contact surface at indenter-workpiece interface, D is the indentation depth, and 2α is the indenter angle (refer to Fig. 2.16 and Fig. 3.1). Since the normalized surface expansion ratio distribution $\phi'(x)$ eliminates the influence of the sliding distance at each point, the relative localization of the surface expansion along the indenter face at each indentation depth can be examined by comparing $\phi'(x)$. Fig. 3.6 shows the normalized surface expansion distribution $\phi'(x)$ at indentation depths of 0.5 and 2 mm. This figure clearly indicates that while the severe localization of the surface expansion occurred in the vicinity of the indenter tip for a small indentation depth (D = 0.5 mm), the surface expansion localization became considerably less and the surface expansion distribution becomes more diffuse with increase in the indentation depth. This suggests that the increase in the specific adhesion force with increasing the indentation depth (Fig. 2.19) results from the widespread distribution of the surface expansion ratio with an increase in the indentation depth, as shown in Fig. 3.6. This is because surface expansion above a certain value is required to cause strong adhesion at the interface, as explained in Section 2.3.3.

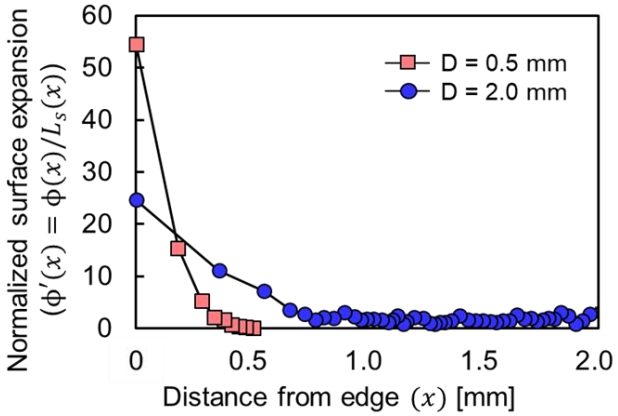

Fig. 3.6 Distribution of surface expansion ratio normalized by sliding distance $L_s(x)$

The change from localized to diffused distribution in surface expansion is most likely caused by the increase of the shear flow stress of the material in the vicinity of the indenter tip owing to the strain hardening caused by the intense plastic deformation. To verify this hypothesis, the surface expansion ratio at $x = 0$ and $x = 0.6$, i.e., $\phi(0)$ and $\phi(0.6)$, are plotted as a function of the indentation depth (Fig. 3.7). As shown in Fig. 3.7 (a), the surface expansion ratio in the vicinity of the indenter tip rapidly increases in the initial stage of indentation, while the transition from rapid to gradual increase in the surface expansion is observed with the increase of the indentation depth. In contrast, at $x = 0.6$, the surface of the material slowly expands after the indentation depth reaches 0.6 mm, then the surface expansion ratio rapidly increases with increasing the indentation depth, as shown in Fig. 3.7 (b). These results clearly demonstrate that the heightened shear flow stress, attributable to strain hardening, leads to the suppression of plastic deformation in the immediate vicinity of the indenter tip. Consequently, this suppressed plastic deformation fosters surface expansion at positions further away from the indenter tip.

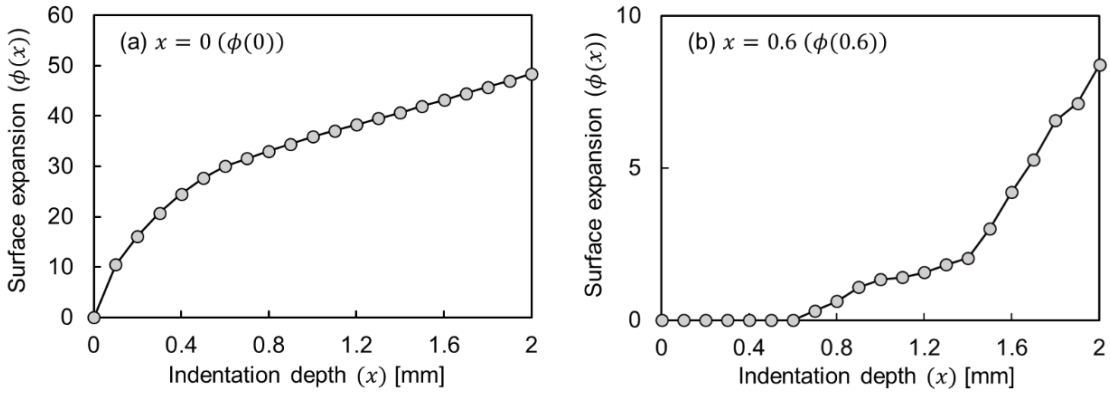

Fig. 3.7 Surface expansion ratio at (a) $x = 0$ and (b) $x = 0.6$

From these results, it is concluded that, in contrast to the conventional "macroscopic" surface expansion ratio, the distribution of the microscopic surface expansion ratio along the deformed surface, known as the surface expansion distribution $\phi(x)$, can effectively capture the quantitative characteristics of material deformation behavior at the contact surface. This nuanced analysis offers deeper insights into the interface adhesion phenomena, allowing for a more comprehensive understanding of the intricate mechanisms at play during indentation processes.

3.4 Relationship between adhesion stress and surface expansion distribution

The results in the previous section clarify that the surface expansion ratio distribution plays a pivotal role in determining the adhesion force since this distribution is closely related to the nascent surface generated during the deformation process. Hence, we hypothesize that the microscopic adhesion force distribution $\tau_a(x)$, i.e., adhesion stress distribution, can be expressed as a function of surface expansion distribution $\phi(x)$:

$$\tau_a(x) = k\phi(x) \tag{3.5}$$

where k is defined as a factor of the adhesion stress distribution, indicating that the adhesion stress $\tau_a(x)$ has the same distribution as the surface expansion distribution $\phi(x)$. To verify the relationship between the adhesion stress distribution and surface expansion distribution, the mean adhesion stress and mean surface expansion ratio are compared by measuring the adhesion force of normal and single-groove indenters. Fig. 3.8 shows the 2-dimensional and 3-dimensional profiles of textured indenter, I-600 and Table 3.1 lists the configuration of the fabricated indenters, which was fabricated by using a femto-second laser technology.

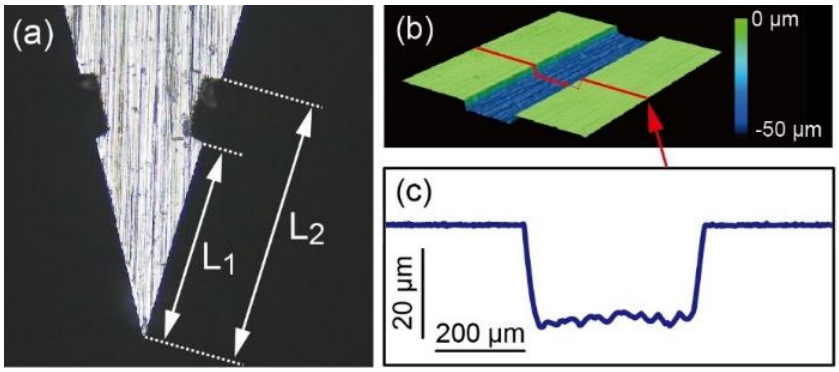

Fig. 3.8 Developed indenter with single micro-groove (I-600), (a) optical microscope image, (b) three-dimensional profile, and (c) two-dimensional profile

Table 3.1 Parameters of single microgroove indenters

Indenter name	L_1 (μm)	L_2 (μm)	Depth of groove D (μm)	x_m (mm)
I-300	300	500	30	0.4
I-400	400	600	30	0.5
I-500	500	700	30	0.6
I-600	600	800	30	0.7
I-700	700	900	30	0.8
I-800	800	1000	30	0.9
I-900	900	1100	30	1.0
I-1000	1000	1200	30	1.1
I-1100	1100	1300	30	1.2
I-1200	1200	1400	30	1.3

As shown in this table, each indenter has a different grooved area on the indenter face. Since the grooved area $L_1 < x < L_2$ becomes a non-contact state at the interface, the adhesion force (F_{a_12}) generated partially in the area between $L_1 < x < L_2$ (Fig. 3.8 (a)) would be zero. By using the adhesion stress distribution $\tau_a(x)$, the adhesion force (F_a) generated over the entire side surface of the indenter and partial force (F_{a_12}) generated in the area between $L_1 < x < L_2$ for normal indenter are expressed as follows:

$$\frac{F_a}{2} = \int_0^{L_t} w\tau_a(x)dx \tag{3.6}$$

$$F_{a\_12} = \int_{L_1}^{L_2} w\tau_a(x)dx \tag{3.7}$$

where L_t is the contact length between the indenter face and specimen, and w is the width of the specimen. By measuring the adhesion force of single groove indenter and normal indenter, namely F_{a_g} and F_a, respectively, adhesion force F_{a_12} partially generated in the area between L_1 and L_2, as well as mean adhesion stress $\tau_a(x_m)$ at the mid point of micro-groove could be calculated by:

$$F_{a\_12} = \frac{F_a - F_{a\_g}}{2} \tag{3.8}$$

$$\tau_a(x_m) = \frac{F_{a\_12}}{w(L_2 - L_1)} = \frac{\int_{L_1}^{L_2} \tau_a(x)dx}{L_2 - L_1} \tag{3.9}$$

Fig. 3.9 (a) shows a schematic diagram of the mean adhesion stress and the position of the groove structure. In this figure, x_m is the position of the midpoint of the micro-groove (see Table 3.1), equal to:

$$x_m = \frac{L_2 + L_1}{2} \tag{3.10}$$

Furthermore, Fig. 3.9 (b) depicts a schematic diagram of the mean surface expansion ratio and the position of the groove structure. As shown in this figure, mean surface expansion ratio $\phi(x_m)$ at the mid point of micro-groove can be expressed as:

$$\phi(x_m) = \frac{\int_{L_1}^{L_2} \phi(x)dx}{L_2 - L_1} \tag{3.11}$$

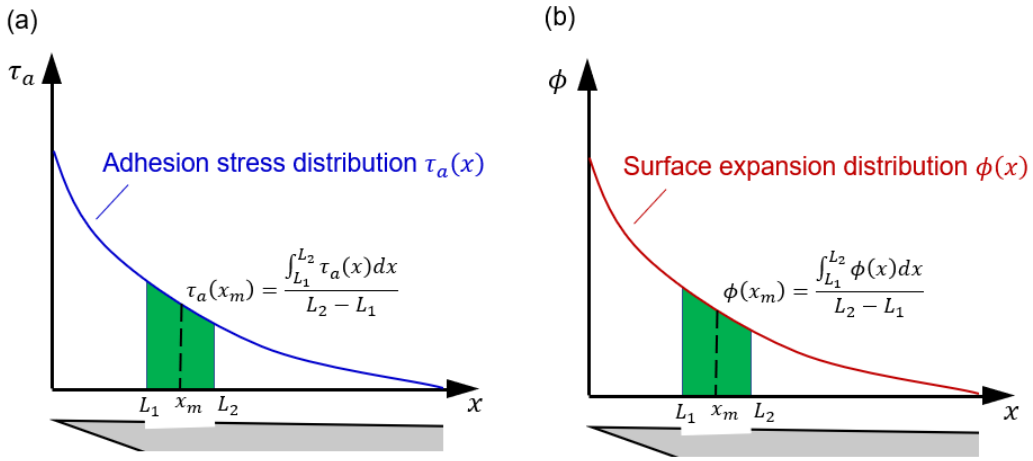

Fig. 3.9 The schematic diagram of (a) mean adhesion stress $\tau_a(x_m)$ and (b) mean surface expansion ratio $\phi(x_m)$ at x_m

Assuming that the hypothesis in Eq. 3.5 is correct, the partially generated force F_{a_12} and mean adhesion stress $\tau_a(x_m)$ are given as follows:

$$F_{a\_12} = \int_{L_1}^{L_2} w\tau_a(x)dx = kw\int_{L_1}^{L_2} \phi(x)dx \tag{3.12}$$

$$\tau_a(x_m) = \frac{F_{a\_12}}{w(L_2 - L_1)} = \frac{\int_{L_1}^{L_2} \tau_a(x)dx}{L_2 - L_1} = \frac{k\int_{L_1}^{L_2} \phi(x)dx}{L_2 - L_1} = k\phi(x_m) \tag{3.13}$$

Eq. 3.13 suggests that mean adhesion stress $\tau_a(x_m)$ should be proportional to the mean surface expansion ratio $\phi(x_m)$ if the assumption (Eq. 3.5) is correct. Therefore, we can verify the hypothesis in Eq. 3.5 by comparing mean adhesion stress, which was experimentally obtained by measuring F_a and F_{a_g} (Eq. 3.9), and mean surface expansion ratio, which was calculated based on surface expansion distribution (Eq. 3.11).

To verify that the assumption in Eq. 3.5 remains valid at larger depths, it was essential to observe a broader processing area than in the previously analyzed region. Accordingly, we adjusted the experimental conditions and obtained the surface expansion ratios at increased depths. Fig. 3.10 shows the surface expansion distribution, $\phi(x)$ for indentation depths of 2, 3, 4, and 5 mm under these new conditions.

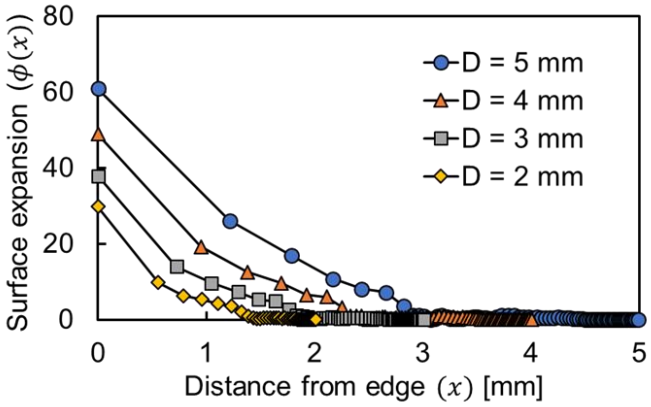

Fig. 3.10 Distribution of surface expansion ratio $\phi(x)$ for each indentation depth

Fig. 3.11 illustrates the relationship between the mean surface expansion ratio, obtained based on Fig. 3.10, and mean adhesion stress at different indentation depths, calculated by force measurements of normal and single-grooved indenters (Eq. 3.9). The red dashed line in this figure represents the shear yield stress τ_s (64 N/mm^2) of the specimen (A1050P) used in this study. It indicates that the adhesion stress is proportional to the surface expansion ratio at relatively small surface expansion ratios. However, at large surface expansion ratios, the adhesion stress nearly converges to the shear yield stress of the specimen under the current indentation configuration, suggesting that the hypothesis in Eq. 3.5 holds true under certain conditions, but becomes unsuitable when the surface expansion ratio is significantly large. This occurs because in highly adhesive materials, like aluminum used in this study, a significant surface expansion ratio generates a substantial amount of nascent surface, leading to strong adhesion at the interface and

causing the adhesion stress to approach the material's shear yield stress. However, the maximum adhesion stress at the interface cannot exceed this yield stress, so even with further surface expansion, the adhesion stress remains capped at this threshold.

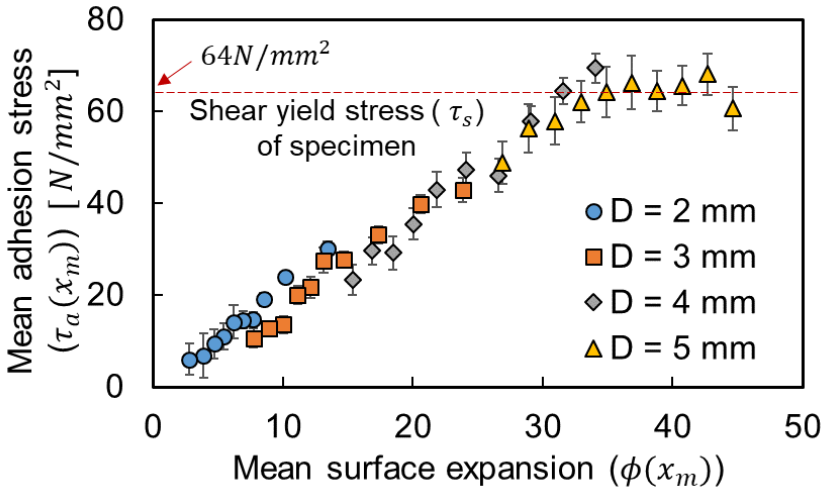

Fig. 3.11 The relationship between the mean surface expansion ratio and mean adhesion stress at different indentation depth

3.5 Adhesion stress distribution model in wedge indentation

3.5.1 Determination and validation

Based on previous section, the adhesion stress distribution under the current indentation configuration and material properties is not totally proportional to the surface expansion distribution and it might converge to the shear yield stress of the material under large surface expansion ratios, which facilitates other assumption that adhesion stress distribution may be similar to sticking-sliding condition at the interface observed in the metal cutting process [147]. Based on following sticking-sliding friction model commonly employed in cutting process:

$$\tau = \begin{cases} \mu\sigma_n & (\mu\sigma_n < m\tau_s) \\ m\tau_s & (\mu\sigma_n \geq m\tau_s) \end{cases} \tag{3.14}$$

the function of adhesion stress distribution could be modified as:

$$\tau_a = \begin{cases} k\phi(x) & (k\phi(x) < m\tau_s) \\ m\tau_s & (k\phi(x) \geq m\tau_s) \end{cases} \tag{3.15}$$

where τ_s is the shear yield stress of the material, k is a factor for the adhesion stress distribution discussed in the previous section, and the constant m (where $0 < m \leq 1$), whose value depends on material properties and processing conditions, typically refers to the friction factor. It describes the relationship between the maximum friction stress at the interface—specifically, the maximum adhesion stress under the current indentation configuration—and the shear yield stress of the work material [148]. Note that the variation of k and m are complicated. Factors influencing these variations will be discussed in a subsequent section. Additionally, it is worth noting that, although the expression form for adhesion stress distribution (Eq. 3.15) closely resembles that of the sticking-sliding friction model (Eq. 3.14), they represent fundamentally different characteristics. Although Eq. 3.14 follows the traditional pressure-based friction model [58], the newly proposed adhesion stress distribution does not exhibit this characteristic. Specifically, the adhesion stress distribution is independent of normal pressure variations and is instead determined by the surface expansion ratio under the current indentation configuration and material properties.

As shown in Fig. 3.11, at large surface expansion ratios, the maximum adhesion stress nearly converges to the shear yield stress of the material. Considering the high adhesion characteristics of the material under the current experimental conditions, as discussed in the previous section, it is reasonable to assume that the maximum adhesion stress closely approximates the material's shear yield stress. Therefore, for the current indentation configuration and material, we set $m = 1$ in Eq. 3.15. In other words, the maximum adhesion stress τ_{a_max} equals to τ_s at large surface expansion ratios. To specify these conditions more clearly, Fig. 3.12, building upon Eq. 3.15, illustrates the predicted adhesion stress distribution along the contact interface, based on the surface expansion distribution obtained under the current indentation scenario (Fig. 3.10). In this figure, L_c denotes the transitional position where τ_{a_max} reaches τ_s, when $\phi(x)$ exceeds a certain threshold. In other words, by determining L_c, we can obtain a quantitative distribution of $\tau_a(x)$ according to Eq. 3.15. In the following part, we will explain how to deduce the value of L_c.

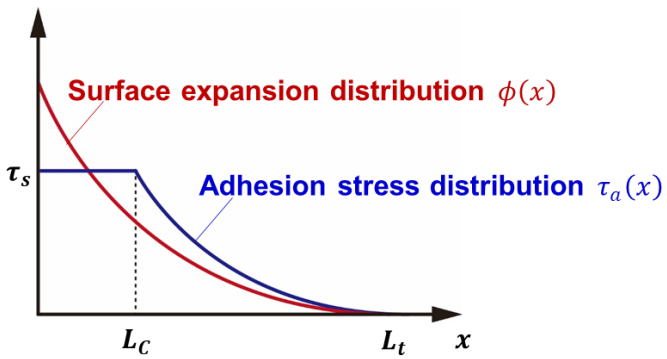

Fig. 3.12 The schematic of the surface expansion distribution and adhesion stress distribution along the contact interface

Based on this discussion, the adhesion stress could be modified as:

$$\tau_a(x) = \begin{cases} k\phi(x) & (x > L_c) \\ \tau_s & (x \leq L_c) \end{cases} \tag{3.16}$$

Considering the continuity of adhesion stress distribution, gives that:

$$\tau_s = k\phi(L_c) \tag{3.17}$$

The integral value of the adhesion stress distribution along the contact interfaces in this research should equal to the total adhesion force F_a. Therefore, the following equation must hold:

$$F_a = 2\int_0^{L_t} w\tau_a(x)dx = 2w\left[\int_0^{L_c} \tau_s dx + \int_{L_c}^{L_t} \tau_a(x)dx\right] = 2w\left[\tau_s L_c + k\int_{L_c}^{L_t} \phi(x)dx\right] \tag{3.18}$$

From the equations above, we can derive the length of L_c, thereby quantifying distribution of adhesion stress. Fig. 3.13 presents the predicted adhesion stress distribution $\tau_a(x)$ at indentation depths of 2, 3, 4, and 5 mm based on Eq. 3.15. The results confirm that as the indentation depth increases, the region where the maximum adhesion stress reaches the shear yield stress also expands, correlating with an increasing overall surface expansion ratio. Conversely, the regions where the adhesion stress does not reach the shear yield stress exhibit a distribution curve similar to the actual surface expansion ratio observed (Fig. 3.10).

Based on this comparison, the experimental mean adhesion stress, calculated as outlined in the previous section (Eq. 3.13), is plotted in Fig. 3.14 to assess the consistency between the experimental data and the model predictions. The comparison shows that the predicted adhesion stress distributions closely align with the experimental values obtained from the grooved indenters, validating the accuracy of the proposed friction models based on surface expansion distribution. These findings lay the foundation for further development and quantification of friction models grounded in actual deformation behavior in metal forming processes.

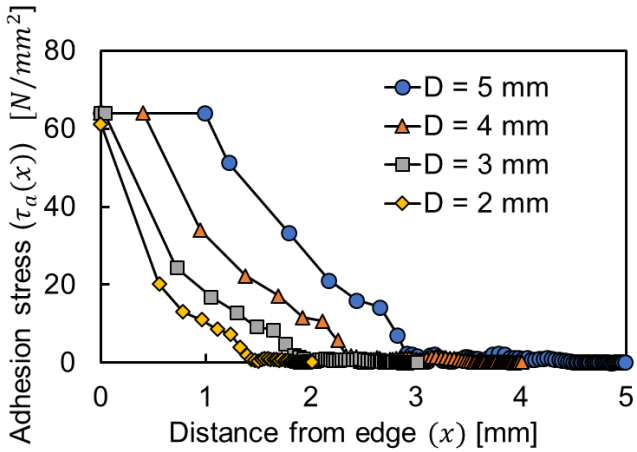

Fig. 3.13 The predicted adhesion stress distribution $\tau_a(x)$ at indentation depths of 2, 3, 4, and 5 mm

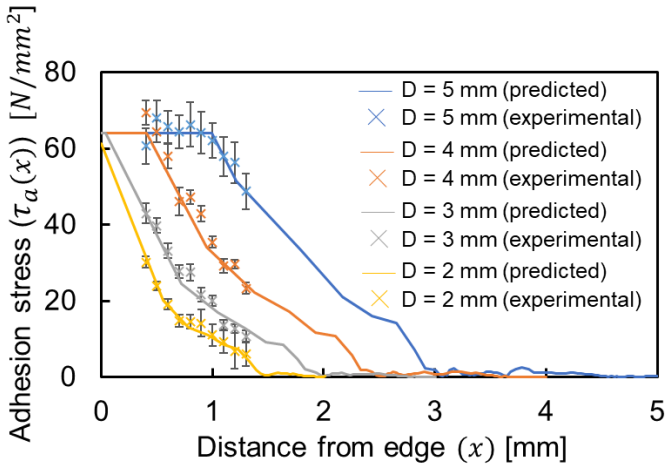

Fig. 3.14 The comparison between experimental results and predicted adhesion stress

3.5.2 Factors influencing adhesion stress distribution

The results of the previous section suggest that the adhesion stress distribution, $\tau_a(x)$, can be represented in terms of the surface expansion ratio, $\phi(x)$, the material's shear yield stress, τ_s, and appropriate coefficients k and m, as Eq. 3.15 expressed. In other words, Eq. 3.15 implies that $\tau_a(x)$ increases proportionally with $\phi(x)$ and converges toward the certain adhesion stress, $m\tau_s$, under the current indentation configuration. For instance, for the highly adhesive material used in this study, it can be assumed that m equals to 1, indicating maximum adhesion stress converges to the material's shear yield stress. Conversely, for materials with lower adhesiveness, m may be smaller than 1, implying that maximum adhesion stress converges to a value below the shear yield stress. A smaller adhesion stress, combined with a larger surface expansion ratio,

inevitably changes the value of k and m. Thus, changes at the interface—such as the introduction of suitable surface coatings or effective lubricants—may lead to variations in k and m. Evidently, multiple factors influence the distribution of adhesion stress. In the following part, we will briefly discuss the effects of lubrication condition, surface coating, material property, and temperature on the proposed adhesion stress distribution model (Eq. 3.15).

(1) Lubrication condition

Good lubrication in metal forming processes can effectively reduce the coefficient of friction and minimize the likelihood of direct contact between the workpiece material and the die, thereby lowering adhesion forces. Specifically, the lubricant film serves as a physical barrier, diminishing metal-to-metal contact and reducing the chances of adhesion [48]. This directly decreases the adhesion stress and the corresponding value of k. Furthermore, by continuously acting as a physical barrier at the interface, effective lubrication ensures its persistent presence, facilitating smoother material flow and reducing the shear stress needed to initiate plastic deformation during processing. Under such condition, the maximum adhesion stress may converge below τ_s, where $m < 1$. Therefore, selecting the appropriate lubricant and optimizing lubrication conditions are crucial in metal forming processes. These factors not only influence adhesion forces but also significantly impact forming quality, die life, and overall process efficiency.

(2) Surface coating

Surface coating generally exhibits a low friction coefficient, significantly reducing the contact friction between the tool and the workpiece. This characteristic can greatly diminish the adhesion of the workpiece material to the tool surface during processing, effectively preventing the formation of a bond between them [4]. The reduction in adhesion stress inevitably leads to a decrease in the value of k. Additionally, in cases of contact between materials with high chemical affinity and adhesion, the maximum adhesion stress at the interface inevitably matches the material's shear yield stress. In such condition, shearing may occur within the material, leaving a portion adhered to the tool, fulfilling $m = 1$. Conversely, when a coating with low surface free energy is applied, the adhesion at the interface decreases, resulting in a adhesion stress at the interface that is smaller than the material's shear yield stress. In this scenario, shearing occurs at the adhesive interface, indicating that $m < 1$. Although surface coating does not directly alter the shear yield stress of the workpiece material, they can indirectly lower the shear stress to initiate deformation by reducing friction, controlling temperature, and optimizing cutting forces. This improvement enhances the material's flowability and contributes to better forming quality.

(3) Material properties

Different materials exhibit distinct adhesion characteristics, primarily due to variations in their chemical composition, crystal structure, and surface energy. For instance, soft metals such as aluminum and copper are more prone to adhesion with die surfaces during processing, largely because of their high surface activity, which enhances adhesion forces. In contrast, harder metals like steel and titanium alloys, which possess higher yield strength and surface hardness, are less likely to adhere to dies or tools during machining [4]. As a result, materials with lower adhesiveness generally exhibit a reduced adhesion force and smaller k values under identical conditions. Moreover, for materials with lower adhesiveness, the reduced adhesion force results in the maximum shear stress at the adhesive interface being smaller than the material's shear yield stress. This causes shearing to occur at the contact interface, leading to $m < 1$. Additionally, highly reactive metals like aluminum tend to form thick oxide layers on their surfaces. The thickness of this oxide layer can also influence the values of k. As illustrated in Fig. 2.18, the oxide layer stretches along with the bulk aluminum during indentation, with a new surface forming only after the surface expansion ratio reaches a certain threshold. When a thick oxide layer is present, fresh surface exposure is reduced compared to that of a thin oxide layer under the same expansion, leading to a decrease in adhesion force and a corresponding reduction in k values. However, with sufficient surface expansion, the maximum adhesion stress is expected to converge to the material's shear yield stress regardless of oxide layer thickness. In such cases, m should remain unchanged, i.e., $m = 1$.

(4) Temperature

Temperature is typically an indirect occurring factor primarily due to issues such as inadequate lubrication or excessive tool friction, both of which can lead to increased wear and elevated temperatures during machining. The effect of temperature on the m value is considerable. Generally, higher temperatures cause material softening, which lowers the material's shear yield stress during processing [148]. As a result, the adhesion stress distribution curve converges below τ_s at room temperature, fulfilling the condition where $m < 1$. This reduction in maximum adhesion stress may lead to a decrease in the ratio of τ_a to ϕ, meaning that the value of k decreases. However, with rising temperatures, the metal's plasticity also increases, making it easier for the material to flow and deform. This enhances the contact area between the nascent surface of material and the tool surface, which can significantly raise adhesion forces. Consequently, this increase in adhesion may lead to a corresponding rise in the k value.

In summary, any factors that directly or indirectly reduce adhesion between the workpiece and the tool surface, significantly impact the distribution of adhesion stress. These

factors are thus essential in shaping the friction models profile, advancing our deeper understanding of tribological phenomena at the interface.

3.5.3 The effects of lubrication conditions on adhesion stress distribution

The previous section explored the influence of various factors on the variables within the adhesion stress distribution model. This section will narrow the focus to one of these key factors: lubrication conditions. Here, we will analyze how variations in lubrication conditions affect the distribution of adhesion stress. It is well-recognized that lubrication methods play a critical role in reducing adhesion, enhancing process efficiency, and improving the overall quality of the forming process. In our current research, a commercially available mineral-oil-based lubricant (refer to as 'oil') was employed in the lubricated condition [149].

Fig. 3.15 is the comparison of adhesion force at different indentation depths, conducted at a speed of 0.1 mm/s, both with and without the presence of a lubricant. This figure distinctly indicates that the adhesion force under the lubricated condition is largely lower than that in the dry condition. This substantial reduction suggests an effective mitigation of interface adhesion due to the application of the lubricant. These findings are supported by observations of the indenter face after experiments (Figs. 3.16 (a) and (b)). Note that, in Fig. 3.16, the results of the element analysis at points A and B conducted using the Laser-Induced Breakdown Spectroscopy [150] are also presented. As shown in Figs. 3.16 (a) and (b), pronounced adhesion to the indenter face, identified as aluminum oxide through the element analysis, is observed in a dry state (Fig. 3.16 (a)). In contrast, under the oil condition, minimal or no adhesion occurs (Fig. 3.16 (b)), indicating that the use of lubricant reduces interface adhesion.

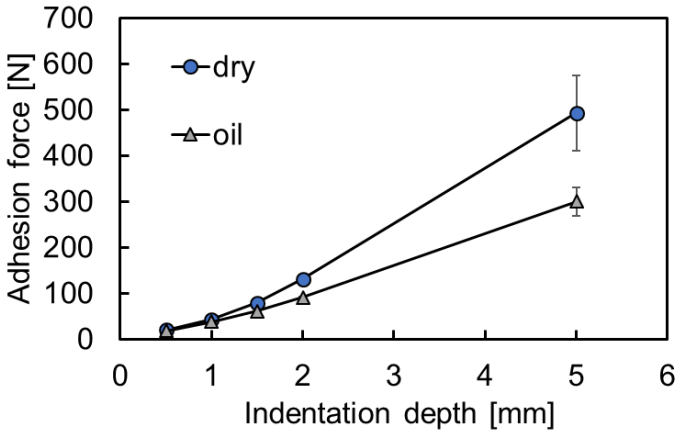

Fig. 3.15 The comparison of adhesion force with and without lubricant

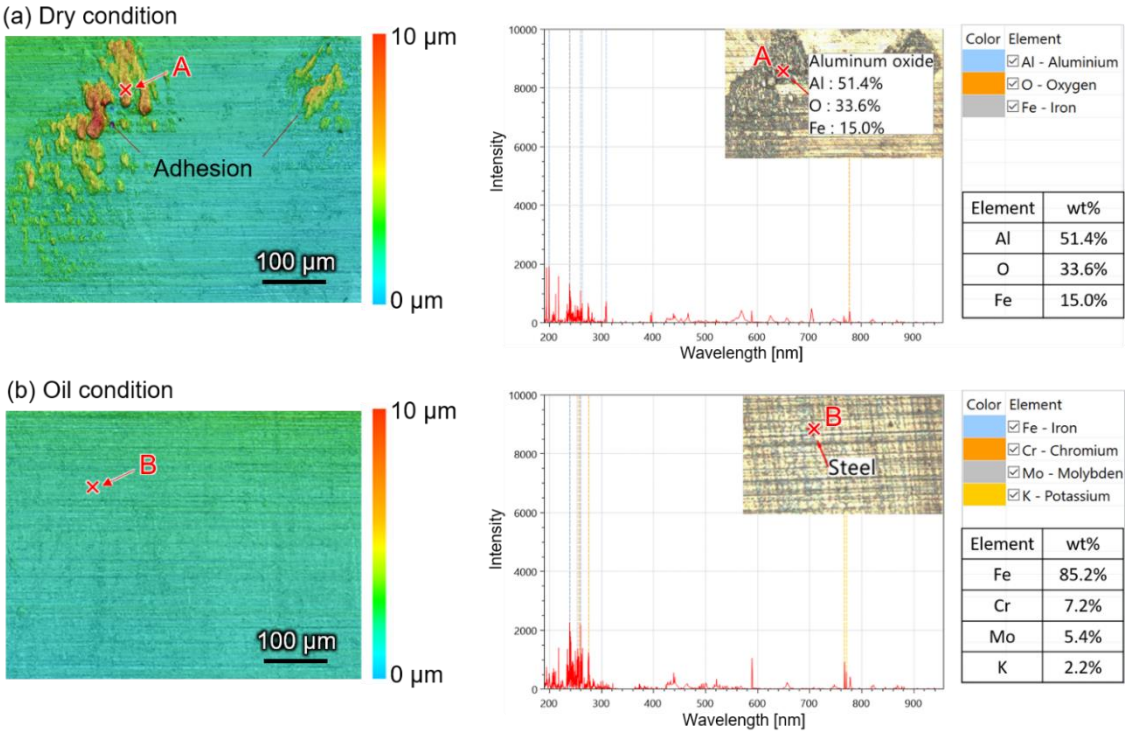

Fig. 3.16 Observation for indenter surface and its corresponding element analysis under (a) dry and (b) oil conditions

To show the effects of lubrication condition on adhesion stress distribution, Fig. 3.17 compares the correlation between the mean surface expansion ratio and mean adhesion stress at different indentation depths, both with and without lubricants. Note that the red dashed line and green dashed line in this figure are the trend lines of this correlation under dry and oil conditions, respectively. As shown in this figure, the ratio of τ_a and ϕ, represented by k, namely the slope of the trend line, is significantly lower under lubricated conditions than under dry conditions. This is because the lubricant effectively reduces the adhesion force, resulting in lower adhesion stress at the same surface expansion ratio.

As discussed in the previous section, if the lubricant could consistently remain at the interface, it would be expected that both k and m would decrease, resulting in $m < 1$. However, current experimental results show that m remains unchanged, as the maximum adhesion stress under lubricated conditions nearly converges to the shear yield stress of the specimen. This finding suggests that, despite the lubricant supply, the adhesion stress in regions with high surface expansion converges to the material's shear yield stress, indicating for the oil conditions employed in current indentation configuration, m can be approximated as 1. This is primarily because the oil film near the indenter tip is squeezed out and breaks down under high pressure, resulting in direct contact between the indenter surface and the nascent material surface, with the

maximum adhesion stress approaching the material's shear yield stress. This observation suggests that in areas of significant surface expansion—where normal stress is also high—the lubricant is unlikely to remain at the interface, as it is expelled and degraded. Thus, it is evident that the effects of lubrication on m and k are heavily influenced by the pressure resistance and penetrability of the lubricant.

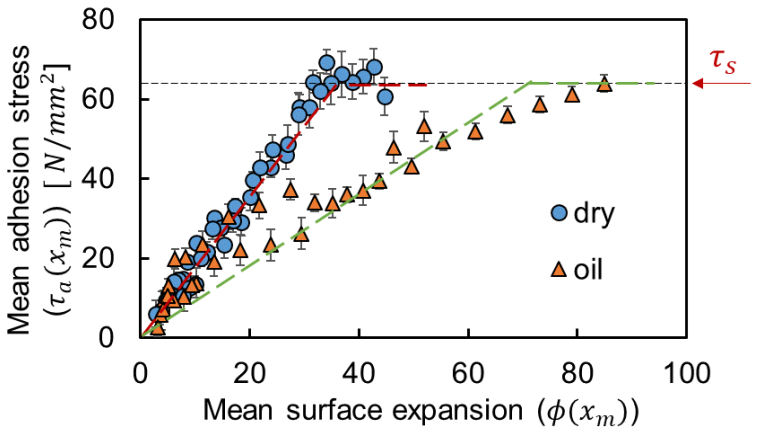

Fig. 3.17 Comparison of the mean surface expansion ratio and mean adhesion stress at different indentation depths between with and without lubricants

Building on this premise, we deduced the adhesion stress distribution under oil conditions at indentation depths of 2, 3, 4, and 5 mm based on Eq. 3.15, alongside the experimentally derived mean adhesion stress values using the same methodology as Fig. 3.14. As illustrated in Fig. 3.18, the predicted adhesion stress distribution aligns closely with the experimental data, even under lubricated conditions, further confirming the reliability of the quantitative adhesion stress distribution model. As shown in the figure, the experimental adhesion force under oil lubrication is slightly higher than the predicted adhesion force. The reason for this is that the micro-grooves can serve as micro-pools for retaining oil fluid [151]. As a result, the oil film near the indenter tip, which would typically break down under high pressure, can still maintain its effect of reducing direct contact between the indenter surface and the nascent surface of the workpiece. This effectively reduces the adhesion force of single-groove indenters.

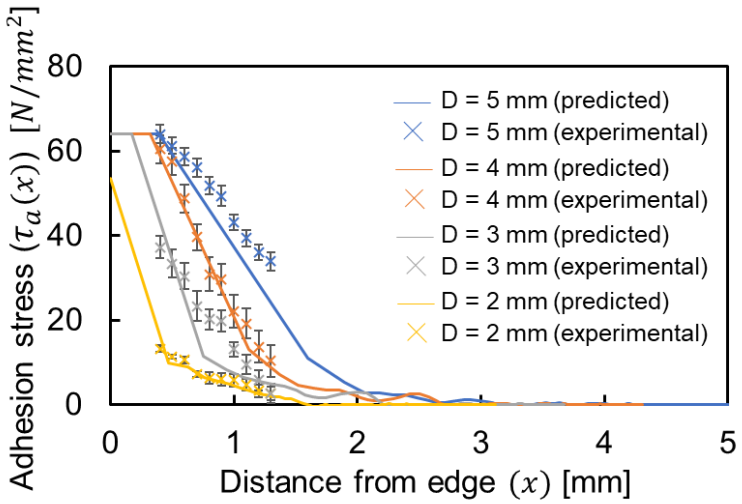

Fig. 3.18 The comparison between experimental results and predicted adhesion stress under oil conditions

3.6 Summary

Interface adhesion is pivotal to understanding tribological behavior at the contact surface, exerting significant influence on tribological phenomena in machining and forming processes. In this chapter, our focus was on exploring the quantitative relationship between interface adhesion phenomenon and surface expansion behavior to propose suitable friction model through wedge indentation and direct observation. The main conclusions are summarized as follows:

(1) The surface expansion ratio exhibits non-uniformity along the indenter face, with surface expansion predominantly localized near the indenter tip. As the indentation depth increases, this localization diminishes significantly, giving way to a more diffuse surface expansion distribution.

(2) The change from localized to diffused distribution in surface expansion with increasing indentation depth is due to the heightened shear flow stress, attributable to strain hardening, leads to the suppression of plastic deformation in the immediate vicinity of the indenter tip. Consequently, this suppressed plastic deformation fosters surface expansion at positions further away from the indenter tip. As the result, the surface expansion distribution becomes more diffused, resulting in the proportion of the surface expansion ratio that exceeds the threshold for causing adhesion at the interface increases, subsequently leading to a higher adhesion force.

(3) The adhesion stress distribution based on surface expansion distribution is proposed and expressed as:

$$\tau_a = \begin{cases} k\phi(x) & (k\phi(x) < m\tau_s) \\ m\tau_s & (k\phi(x) \geq m\tau_s) \end{cases}$$

Specifically, adhesion stress, $\tau_a(x)$, is proportional to the surface expansion ratio, $\phi(x)$, with the factor of k at relatively smaller surface expansion ratios, while it converges to the certain adhesion stress, $m\tau_s$, at larger surface expansion ratios during processing. Multiple factors influence the constants m and k, including lubrication conditions, surface coatings, material properties, and temperature. In our study, the effects of lubrication conditions on adhesion stress distribution were discussed as an effective example, demonstrating how lubrication can significantly alter the adhesion characteristics and frictional behavior at the interface. The findings reveal a high degree of consistency between the predicted values of adhesion stress distribution and the experimental mean adhesion stress values, both with and without lubricants. This consistency makes it possible to quantify the friction model based on actual deformation behavior in the metal forming process, marking a significant breakthrough in quantitatively investigating the relationship between tribological phenomena and deformation behavior.

Chapter 4 The effects of interface friction on plastic deformation in metal surface and bulk

4.1 General introduction

The previous chapter highlighted the critical role of the microscopic distribution of the surface expansion ratio in understanding interface adhesion phenomena. However, limited attention has been given to the factors influencing this distribution. Clarifying these determinants could provide a deeper insight into the interrelationship between material plastic deformation at the interface and the prevailing friction conditions. It is well-established that under severe friction, a phenomenon of flow localization occurs at the contact interface during metal plastic processing and this flow localization closely resembles the behavior of a fluid-like boundary layer [112, 118]. Investigating the development of the boundary layer structure might elucidate the role in how the surface of bulk material expands at the contact interface and determine surface expansion distribution, since both surface expansion and the plastic boundary layer result from interface friction under severe sliding contact conditions [69]. Therefore, in this chapter, plastic deformation behaviors, including surface expansion at the contact interface are quantified by using PIV analysis, and compare it with traditional boundary layer theory. Specifically, the quantitative relationship between interface friction and interface deformation, namely wall-slip phenomenon and surface expansion behavior at the interface, is investigated. Through PIV analysis, the critical factors influencing surface expansion distribution are investigated. Moreover, it explores the interrelations among interface friction, boundary layer phenomena and the distribution of surface expansion and proposes quantitatively assess tribological conditions at the sliding contact.

4.2 Boundary layer and wall-slip phenomenon

Boundary layer phenomena hold significant importance in fluid mechanics, wherein a thin layer of fluid forms over a solid surface due to differences in velocity gradients. It has been reported that the deformation field in the vicinity of severe sliding contact caused the friction induced retardation of material flow, such as tool-chip interface in machining process and die/mold-material interface in forming process, resembles a fluid-like boundary layer flow [68]. To understand the relationship between the friction condition and plastic boundary layer structure, wedge indentation experiments were conducted. Fig. 4.1 shows the deformation field superimposed by the streaklines obtained by the PIV analysis. In Fig. 4.1 (a), the initial streak lines U_n (n: streakline number) at $t = t_0$ are placed orthogonal to the indenter face, i.e., the X and Y axes are tangential and normal to the indenter face, respectively. Fig. 4.1 (b) shows the

material flow at $t = t_0 + 5$ s. The red and yellow points in these figures correspond to the endpoints of the streaklines and points on the indenter face tangent to the initial position of the endpoints, respectively. In other words, the gap between red point and yellow point for each streakline at $t = t_0 + 5$ s (Fig. 4.1 (b)) indicates the relative motion between the material and indenter at the interface.

The friction at the interface induces a shear stress tangential to the bulk material near the indenter surface, which is transmitted to the workpiece and influences its deformation behavior. As depicted by the streaklines in Fig. 4.1 (b), the material displacement along the x-direction gradually diminishes and eventually becomes stationary at a distance from the indenter face, indicating the existence of velocity gradients of the bulk deformation. This result shows that the material is dragged by the interface friction between the indenter and material, which consequently results in the formation of a plastic boundary layer.

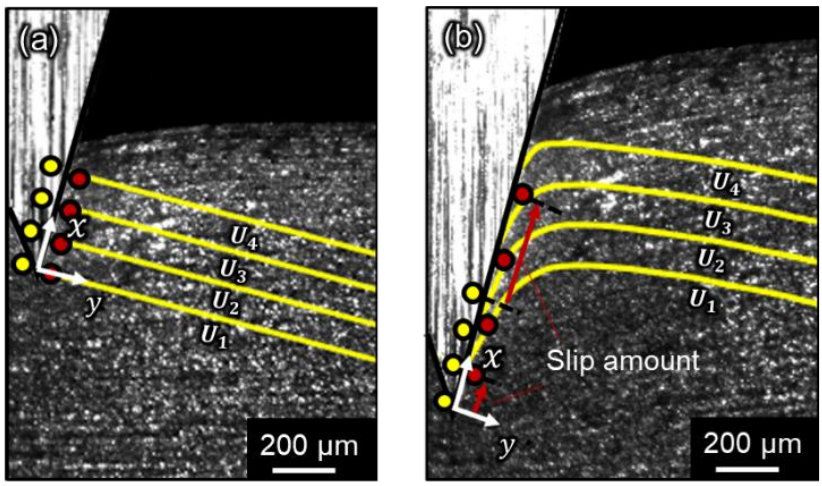

Fig. 4.1 Material flow at (a) $t = t_0$, (b) $t = t_0 + 5$ s

The characteristics of this friction-induced deformation are also evident in the distribution of the velocity in x direction (v_x), i.e., velocity of the material along the indenter face, as shown in Fig. 4.2. Note that the velocity field is determined by averaging velocities over 20 consecutive frames, and $v_x(x, y)$ denotes the value of v_x at the coordinate (x, y). Fig. 4.2 (a) confirms that the formation of a steep velocity gradient that constitutes the plastic boundary layer. Also, Fig. 4.2 (b) shows the relationship between v_x and the vertical distance away from the interface (y) at $x = 100, 300, 500, 700$ μm, confirming that the deformation is largely confined to the region close to the indenter face. Additionally, Fig. 4.2 (b) indicates several aspects of the plastic boundary layer resulting from the interface friction between the material and the indenter face. Firstly, the velocity gradient, namely the boundary layer structure, differs depending on the

value of the x-coordinate and a more pronounced velocity gradient is observed in the area closer to the indenter tip. As explained in previous chapter, the adhesion friction stress along the indenter face increases toward the indenter tip, suggesting that the boundary layer structure is determined by the friction condition at the interface. Secondary, velocity difference exists at the interface between the indenter and the material, namely, wall-slip occurs at the interface. In Fig. 4.2 (b), v_{wall} is the velocity component of the indenter face in the x-direction, equivalent to $v_0 cos\alpha$ (v_0: indentation speed, α: half of indenter angle). As shown in this figure, the velocity of the material at the interface, i.e., $v_x(x, 0)$, is lower than v_{wall}, which clearly shows the existence of the wall slip at the interface and causes the relative motion between the material and indenter at the interface, as shown in Fig. 4.1 (b).

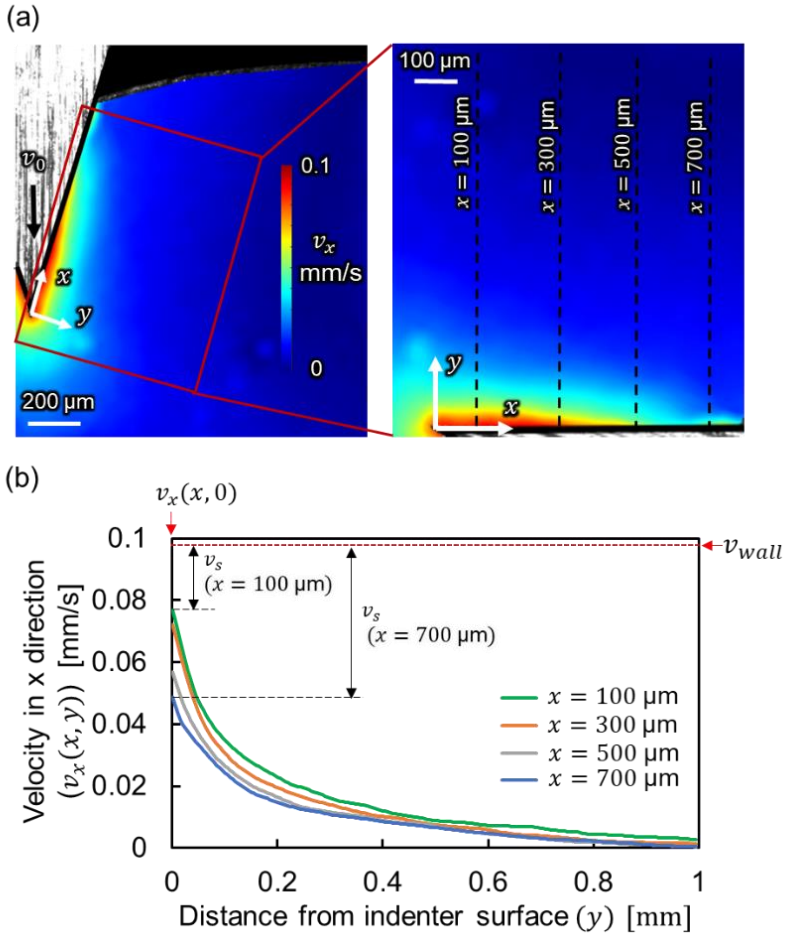

Fig. 4.2 (a) Velocity field of the x direction and (b) the relationship between v_x and y at different values of x axis ($x = 100, 300, 500, 700$ μm)

In order to quantitatively examine the relationship among interface friction, boundary layer structure, and wall-slip at the interface, wall-slip velocity $v_s(x)$ is defined as follows:

$$v_s(x) = v_{wall} - v_x(x, 0) \tag{4.1}$$

Fig. 4.3 shows the distribution of $v_s(x)$ along the indenter face, indicating that $v_s(x)$ decreases toward the indenter tip. This decrease arises from material deformation at the interface caused by friction drag, where the velocity of the material $v_x(x, 0)$ is higher near the indenter tip due to greater friction stress.

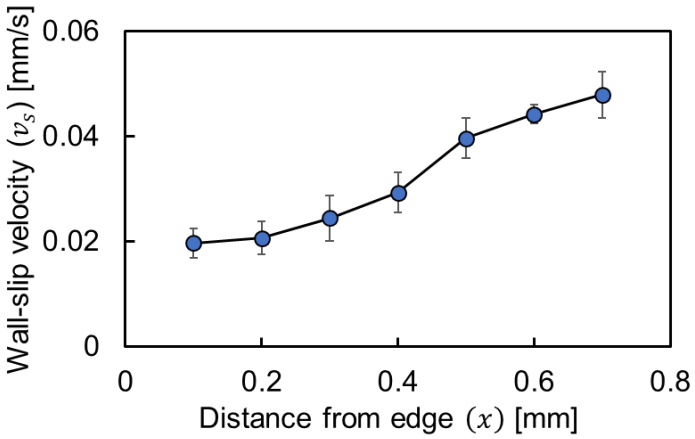

Fig. 4.3 Wall-slip velocity distribution

Furthermore, to examine the impact of wall-slip velocity on the boundary layer structure, the velocity field $v_x\,(x, y)$, which is shown in Fig. 4.2 (b), is normalized based on the following equation:

$$v_n(x, y) = \frac{v_x\,(x, y)}{v_{wall} - v_s(x)} = \frac{v_x\,(x, y)}{v_x\,(x, 0)} \tag{4.2}$$

Fig. 4.4 shows the normalized velocity field $v_n(x, y)$ at $x = 100, 300, 500, 700$ μm. In contrast to Fig. 4.2 (b), all curves of the normalized velocity field nearly converge to a single curve, strongly suggesting that the boundary layer structure is determined by the wall-slip behavior at the interface. These findings suggest that the interface friction primarily determines the wall-slip behaviors at the interface, such as wall-slip velocity or wall-slip amount, which subsequently determines the bulk deformation of the material, i.e., the plastic boundary layer structure.

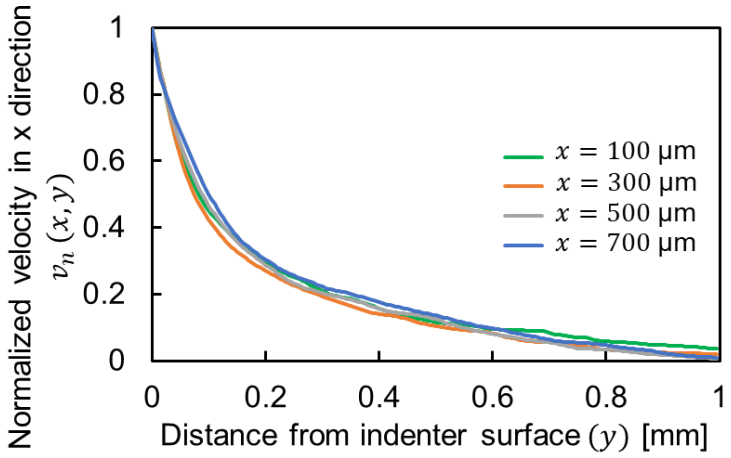

Fig. 4.4 The relationship between v_n and y at different values of x axis ($x = 100, 300, 500, 700$ μm)

Note that the friction-induced plastic boundary layer is very similar to a laminar fluid boundary layer characterized by steep velocity gradients. However, wall-slip behavior plays a crucial role in the plastic boundary layer, which is not typically observed in classical fluid mechanical boundary layers. This distinction may be one of the features of the friction-induced plastic boundary layer and aids in understanding friction-induced deformation behaviors.

4.3 Relationship between the wall-slip velocity and surface expansion distribution

Explained in the preceding section, wall-slip behavior is pivotal in comprehending interface friction and its linked deformation patterns. Surface expansion stands out as a paramount phenomenon in sliding contact, exerting a significant influence on interface friction. Specifically, the surface expansion ratio—denoting the ratio between the original material's surface area and the area post-deformation—directly influences the exposure of chemically active nascent surfaces at the contact interface, which also directly corresponds to the adhesion force distribution at the interface. Additionally, the surface expansion ratio is distributed non-uniformly at the interface, and its distribution also changes as the friction condition at the interface during the deformation process. Prior chapter has paid limited attention to the factors influencing this distribution. This section seeks to fill this gap by elucidating the relationship between surface expansion behavior and the wall-slip phenomenon, and identifying the key factors influencing the distribution of surface expansion at the sliding contact interface.

Section 3.2.1 and Section 4.2 clearly illustrate methods for determining the distribution of surface expansion and wall-slip velocity without considering the relationship with time, respectively. To comprehensively explore the relationship between wall-slip velocity and surface

expansion distribution during indentation and facilitate understanding, we analyze the distribution of wall-slip velocity and surface expansion distribution over time, corresponding to varying indentation depths. Fig. 4.5 depicts the procedure for obtaining distribution of surface expansion ratio $\phi(x,t)$ at any given time t. By tracking virtual markers placed at regular intervals of l on the metal surface (Fig. 4.5 (a)) through PIV analysis, the position of tracking marker P_n from the indenter tip (x_n) and the distance between P_n and P_{n+1} $(l+\Delta l_{n\_n+1})$ at different time t during the indentation process can be obtained (Fig. 4.5 (b)). The distance of midpoints x_{n_n+1} between P_n and P_{n+1} from the indenter tip, namely $x_{n\_n+1}(t)$ and the corresponding local surface expansion ratio $\phi_{n\_n+1}(t)$ at the position of point x_{n_n+1} at given time t are calculated by the following Eq. 4.3 and Eq. 4.4. The distribution of surface expansion ratio $\phi(x,t)$ is determined based on the local surface expansion ratio $\phi_{n\_n+1}(t)$ and local point $x_{n\_n+1}(t)$, respectively (Fig. 4.5 (c)).

$$x_{n\_n+1}(t)=\begin{cases}0 & (n=0)\\ \frac{x_n(t)+x_{n+1}(t)}{2} & (n>0)\end{cases} \tag{4.3}$$

$$\phi_{n\_n+1}(t)=\frac{\Delta l_{n\_n+1}(t)}{l}=\begin{cases}\frac{x_n(t)+x_{n+1}(t)-l}{l} & (n=0)\\ \frac{x_{n+1}(t)-x_n(t)-l}{l} & (n>0)\end{cases} \tag{4.4}$$

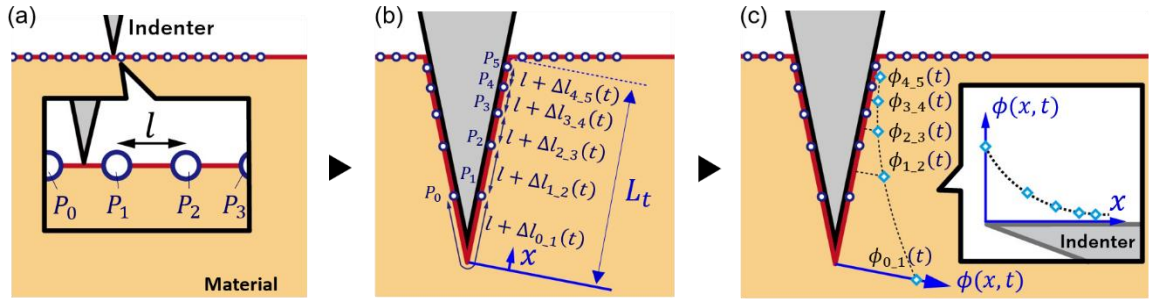

Fig. 4.5 The procedure for obtaining distribution of surface expansion ratio $\phi(x,t)$ at given time t

Fig. 4.6 (a) shows images featuring superimposed virtual tracking markers (l = 25.6 μm) at an indentation depth of 5 mm, demonstrating that the virtual tracking markers successfully visualize the local surface expansion along the indenter face. The tracking markers (P_1-P_5), initially placed on the metal surface at regular intervals (see Fig. 4.5 (a)), demonstrate varied movement, reflecting different slip conditions along the interface surface. Moreover, Fig. 4.6 (b) illustrates the surface expansion distribution $\phi(x,t)$ at specific time intervals—20, 30, 40, and

50 seconds—corresponding to indentation depths of 2.0, 3.0, 4.0, and 5.0 mm, respectively. Note that this figure should naturally match with Fig. 3.10. As depicted in this figure, the surface expansion ratio varies along the indenter face, and the localization of the surface expansion in the vicinity of the indenter tip is evident. These results confirm the non-uniform nature of the surface expansion distribution along the indenter face and indicate that the localized surface expansion results in the severe frictional conditions near the indenter tip.

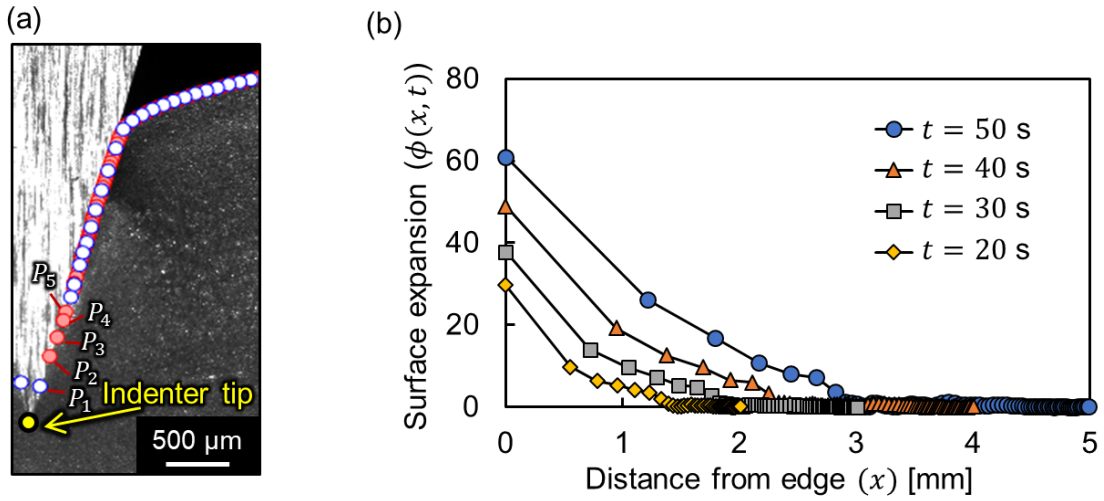

Fig. 4.6 Distribution of surface expansion ratio: (a) tracking markers with the depth of 5 mm and (b) surface expansion distribution at different given time t

According to Eq. 4.4, the non-uniform surface expansion distribution is caused by the difference in the surface expansion deformation behavior at each two consecutive points along the indenter face at a given time. This uneven surface expansion distribution is closely linked to the wall-slip velocity at each point along the interface. To depict the relationship between surface expansion and wall-slip velocity, a schematic diagram in Fig. 4.7, illustrating the assumption of the movement of each tracking point under slip and no-slip conditions, is presented.

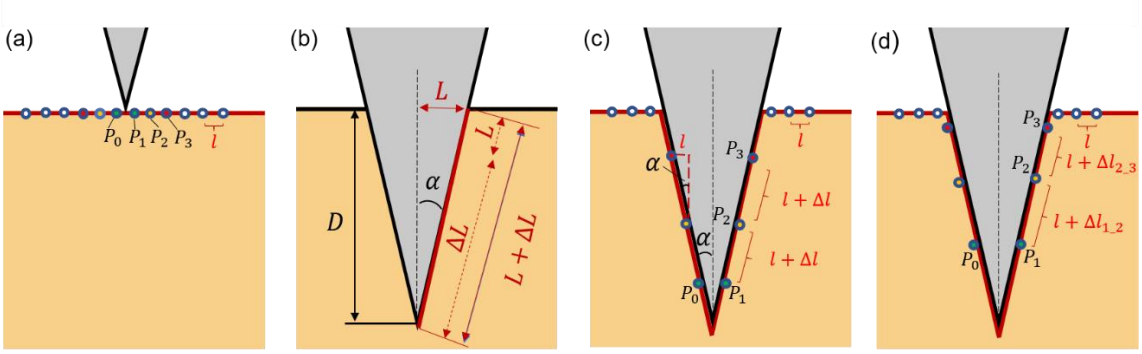

Fig. 4.7 Schematic of (a) initial distribution of tracking points before indentation, (b) macroscopic deformation after indentation, (c) distribution of tracking points under no-slip condition and (d) distribution of tracking points under slip condition after indentation

Assuming that the tracking points P_i ($i = 0, 1, 2, \cdots, n$) are plotted on the metal surface with the regular interval distance l before indentation (Fig. 4.7 (a)) and $v_i(t)$ (wall-slip velocity) is the instantaneous velocity of the tracking marker P_i along the indenter face at a given time t. At any incremental time Δt, the corresponding wall-slip velocity for each two tracking markers P_n and P_{n+1} are $v_n(t + \Delta t)$ and $v_{n+1}(t + \Delta t)$.

The "macroscopic" surface expansion ratio over the entire deformation area can be defined as:

$$\phi = \frac{\Delta L}{L} = \frac{1 - sin\alpha}{sin\alpha} \tag{4.5}$$

where ΔL represents the difference between the original surface length of the undeformed specimen, L, and the surface length after the indentation process (see Fig. 4.7 (b)).

Presuming that the contact condition at the interface adheres to a no-slip condition, i.e., the wall-slip does not occur at the indenter-material interface, where $v_i(t)$ equals to zero, the virtual tracking point at the metal surface moves integrally with the indenter (Fig. 4.7 (c)), i.e., microscopic incremental length for each pair of two tracking markers, Δl, remains uniform, and the total Δl for all tracking markers is equal to ΔL. Under such conditions, the local microscopic surface expansion ratio $\phi_{n\_n+1}(t)$ for each pair of two tracking markers P_n and P_{n+1} at given time t could be expressed as:

$$\phi_{n\_n+1}(t) = \frac{\Delta l_{n\_n+1}(t)}{l} = \frac{\Delta l}{l} = \frac{1 - sin\alpha}{sin\alpha} \tag{4.6}$$

This implies that in the absence of wall-slip at the interface, the surface expansion ratio remains consistently uniform across the entire contact area, maintaining the value consistent with the macroscopic surface expansion ratio. In other words, any difference in the surface expansion ratio should be attributed to the wall-slip behavior at the interface.

On the other hand, assuming that the contact condition at the interface follows the slip condition (Fig. 4.7 (d)) —a scenario that more accurately reflects reality—, uneven friction condition at the interface inevitably results in different interface deformation behavior, causing changes in wall-slip velocity along the interface. According to Eq. 4.4, the incremental surface expansion ratio $\Delta\phi_{n\_n+1}(t)$ at any incremental time Δt for each two tracking markers P_n and P_{n+1}could be expressed as:

$$\Delta\phi_{n\_n+1}(t) = \phi_{n\_n+1}(t+\Delta t) - \phi_{n\_n+1}(t) = \frac{\Delta l_{n\_n+1}(t+\Delta t)}{l} - \frac{\Delta l_{n\_n+1}(t)}{l} =$$

$$\begin{cases} \frac{[x_0(t+\Delta t)-x_0(t)]+[x_1(t+\Delta t)-x_1(t)]}{l} = \frac{\int_t^{t+\Delta t}[v_0(t)+v_1(t)]dt}{l} & (n=0) \\ \frac{[x_{n+1}(t+\Delta t)-x_{n+1}(t)]-[x_n(t+\Delta t)-x_n(t)]}{l} = \frac{\int_t^{t+\Delta t}[v_{n+1}(t)-v_n(t)]dt}{l} & (n>0) \end{cases} \quad (4.7)$$

Here, $\phi_{n\_n+1}(t+\Delta t)$ and $\phi_{n\_n+1}(t)$ represent the microscopic surface expansion ratio for each two tracking markers P_n and P_{n+1} at given time $(t+\Delta t)$ and t, respectively. Meanwhile, $\Delta\phi_{n\_n+1}(t)$ is the incremental value of $\phi_{n\_n+1}(t)$ after an interval time of Δt. This suggests that the distribution of the surface expansion ratio should be determined by the distribution of the wall-slip velocity. To illustrate the wall-slip behavior at the indenter-material interface, the evolution of the distance from the indenter tip, x_n and wall-slip velocity, v_s, for each tracking point (P_1-P_5, see Fig. 4.6) are obtained through the PIV analysis, as shown in Fig. 4.8.

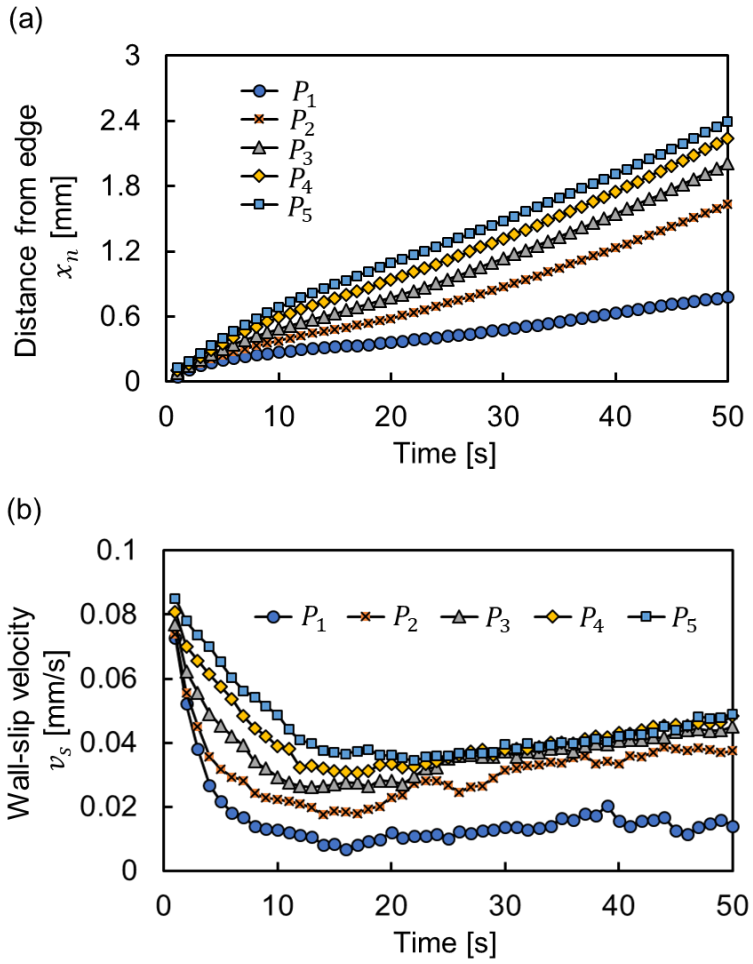

Fig. 4.8 (a) Distance from the indenter tip and (b) wall-slip velocity v_s for each tracking point over time

As illustrated in Fig. 4.8, during the initial indentation, the tracking points are close to the indenter tip (Fig. 4.8 (a)), while exhibiting relatively high wall-slip velocity for each tracking point (Fig. 4.8 (b)). This occurrence is due to lower interface friction at the interface resulting from less fresh surface generated and smaller adhesion at the interface, manifesting as smaller incremental distance between consecutive points (Fig. 4.8 (a)). With the progress of indentation, the friction increases because of more nascent surface generated, thereby largely increasing the adhesion force at the interface, corresponding to large incremental distance of each two consecutive points (Fig. 4.8 (a)). Consequently, the wall-slip velocity for P_1 diminishes and remains nearly constant over time, even as the distance of P_1 extends far from the indenter tip. On the other hand, wall-slip velocity for tracking points P_2-P_5 decreases initially at small indentation depths but gradually increases over time (Fig. 4.8 (b)), leading to distinct growth trends in distance from the indenter tip (Fig. 4.8 (a)).

These differences in the deformation behaviors stem from strain hardening induced by intense plastic deformation near the indenter tip as the indentation depth increases. This phenomenon would hinder further deformation in the vicinity of indenter tip, causing a slowdown in the increasing distance of P_1 from the indenter tip (Fig. 4.8 (a)), as well as reflecting in an almost constant wall-slip velocity (Fig. 4.8 (b)). Subsequently, decreased deformability promotes surface deformation in regions farther from the indenter tip (Fig. 4.8 (a)), triggering an increase in wall-slip velocity for P_2-P_5 (Fig. 4.8 (b)). This ultimately results in a diffuse surface expansion distribution and substantial nascent surface generation (see Fig. 4.6 (b)), since nascent surface does not form until the surface deformation reaches a certain threshold, as illustrated in Fig. 2.18. A more diffuse surface expansion distribution, inevitably increases proportion above a certain value of surface expansion ratio that is required to cause a huge adhesion at the interface, consequently elevating interface friction. As a result, this increased friction impedes material deformation further, manifesting as less wall-slip velocity in the vicinity of indenter tip and more diffuse surface expansion distribution. These findings distinctly illustrate the interrelation and mutual influence among interface friction, wall-slip velocity, and surface expansion distribution.

To verify the relationship between surface expansion distribution and wall-slip velocity, we compare the local surface expansion ratio $\phi_{n\_n+1}(t)$ of several two consecutive tracking markers with different given time t, calculated through the procedure for obtaining distribution of surface expansion ratio (Eq. 4.4), with the integral of wall-slip velocity $\phi_{n\_n+1}(t)_{calculated}$ (Eq. 4.7), as shown in Fig. 4.9. Note that Δt equals to 2 second in this figure. As demonstrated in Fig. 4.9, $\phi_{n\_n+1}(t)$ is highly consistent with $\phi_{n\_n+1}(t)_{calculated}$, indicating that the distribution of surface expansion ratio is indeed determined by that of the wall slip velocity. These findings clearly indicate that non-uniform surface expansion distribution results from variations in the wall-slip velocity along the sliding surface induced by interface friction.

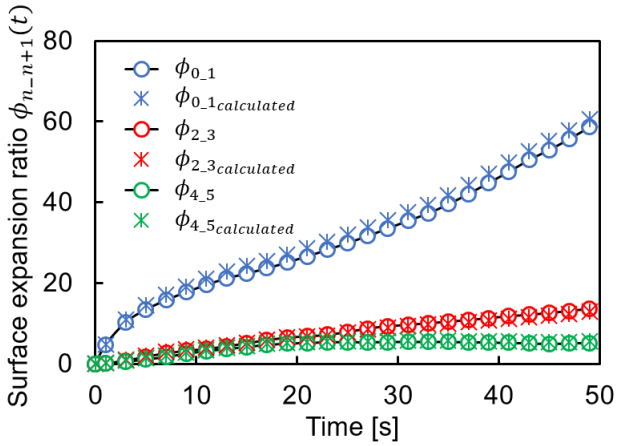

Fig. 4.9 The comparison between $\phi_{n\_n+1}(t)$ and $\phi_{n\_n+1}(t)_{calculated}$

4.4 The quantitative assessment of tribological condition at sliding contact

As discussed in the previous section, interface friction, wall-slip velocity, and surface expansion distribution are interconnected and mutually influential. Moreover, surface expansion distribution can serve as an indicator of adhesion friction force distribution at the contact interface, potentially providing a quantitative approach to assess tribological conditions in sliding contact scenarios. For instance, both surface coatings and lubrication conditions can effectively alter the tribological conditions at the interface, inevitably impacting wall-slip behavior and surface expansion distribution. This suggests that we can quantitatively assess the tribological state of a sliding interface by evaluating changes in wall-slip velocity and surface expansion distribution—a method of substantial practical importance. Moreover, if tribological conditions at the interface can be quantified, we can also evaluate tool wear, the comparative effectiveness of different tool coatings, and lubrication performance, all of which significantly influence the interface's tribological properties.

To verify this insight clearly and demonstrate its potential in developing a method for quantitatively evaluating lubricant lubricity, Fig. 4.10 (a) and Fig. 4.10 (b) are the image of the 30 deg indenter, superimposed with the streaklines at $t = t_0 + 5$ s, with and without the lubricant. In these images, yellow and red points represent the endpoints of the streaklines and points on the indenter face tangent to the initial position of the endpoints, respectively. Additionally, Fig. 4.11 presents a comparison of the slip amounts for each streakline (U_1-U_4) with and without the presence of oil. The results clearly show that the lubricant effectively increases the gap between the red and yellow points, representing the slip amount, at $t = t_0 + 5$ s, indicating the decreased interface friction at the interface. These findings are supported by the distribution of the wall slip velocity along the indenter face at $t = t_0 + 5$ s (Fig. 4.12), under both dry and lubricated conditions. These variations in the state of interface friction manifest as differences in wall-slip behavior, with the wall-slip velocity under the lubricated condition being approximately 60% higher than that under dry conditions (Fig. 4.12), confirming the significant facilitation of sliding motion at the interface due to the presence of lubricant. These results decisively demonstrate the effective reduction of interface friction between the indenter and the material through the application of a mineral-oil-based lubricant.

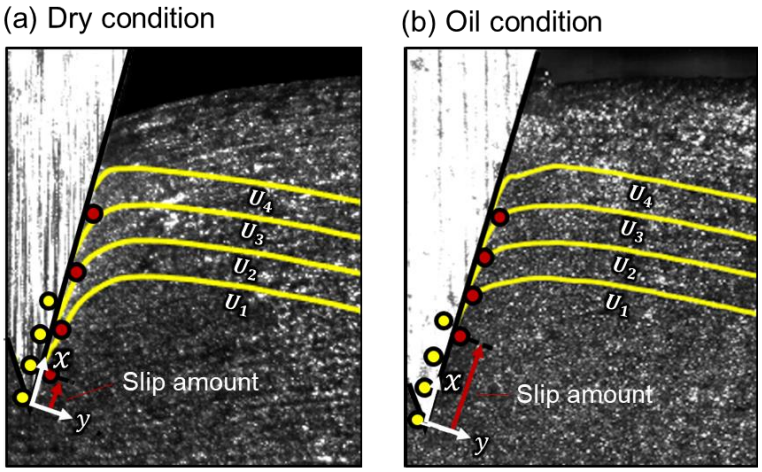

Fig. 4.10 The comparison of streaklines at $t = t_0 + 5$ s under (a) dry and (b) oil conditions

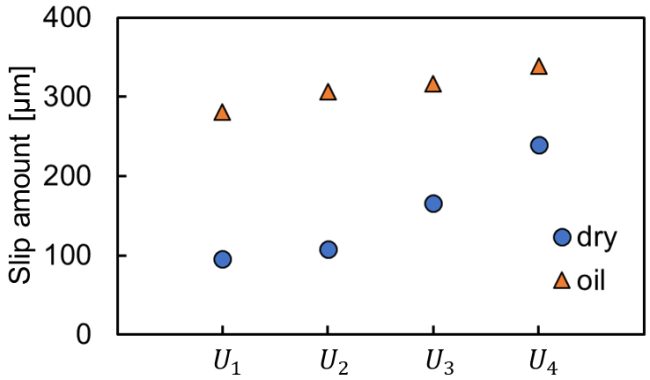

Fig. 4.11 The comparison of slip amount for each streakline

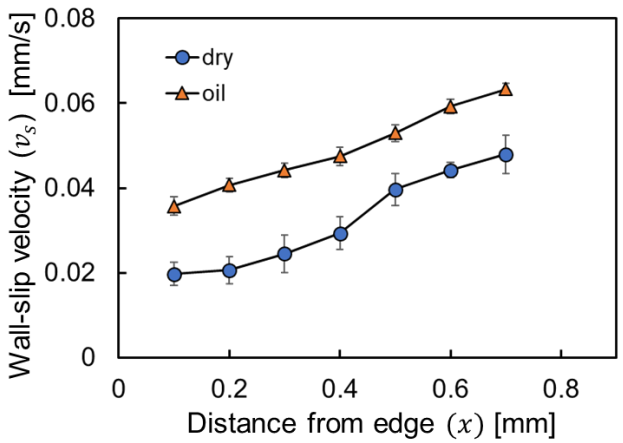

Fig. 4.12 The distribution of the wall slip velocity with and without lubricants

Fig. 4.13 shows the images featuring superimposed virtual tracking markers at an indentation depth of 5 mm, with and without the application of lubricant, indicating alterations in the material's deformation behavior at the sliding contact attributable to the presence of lubricant. As seen in this figure, under the lubricated condition (Fig. 4.13 (b)), substantial wall-slip of the material results in pronounced surface expansion in the vicinity of the indenter tip. Fig. 4.14 provides a schematic diagram illustrating the impact of localization of the surface expansion at the indenter tip on the surface expansion distribution under the dry and lubricated conditions. When subjected to the same indentation depth in both dry and lubricated conditions, the total amount of surface expansion, ΔL, remains consistent (refer to Fig. 4.7 (b)). As depicted in Fig. 4.14, at a given time interval Δt, the indenter initially contacts tracking points P_0 and P_1, resulting in corresponding wall-slip velocities v_0 and v_1. Due to the reduced interface friction in the presence of lubricant, v_0 and v_1 are greater than those under dry conditions. These larger values of v_0 and v_1 inevitably amplify the value of $\phi(0,t)$ (refer to Eq. 4.4 and Eq. 4.7), indicating that the surface expansion under lubricant conditions becomes more localized in the vicinity of indenter tip (Fig. 4.14 (b)). In other words, it should be possible to quantitatively visualize the lubricity at the interface by evaluating the degree of concentration of the distribution of the surface expansion ratio in the vicinity of the indenter tip.

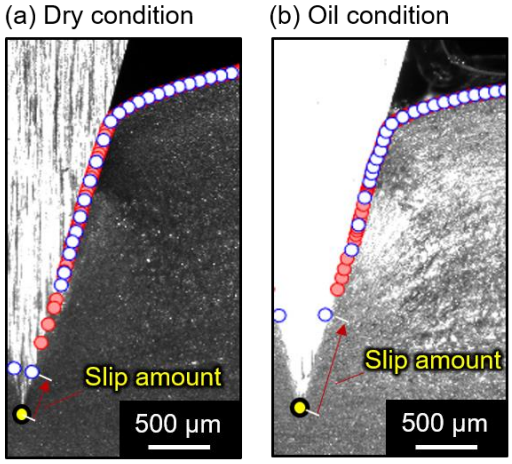

Fig. 4.13 Tracking markers under (a) dry and (b) oil conditions at the depth of 5 mm

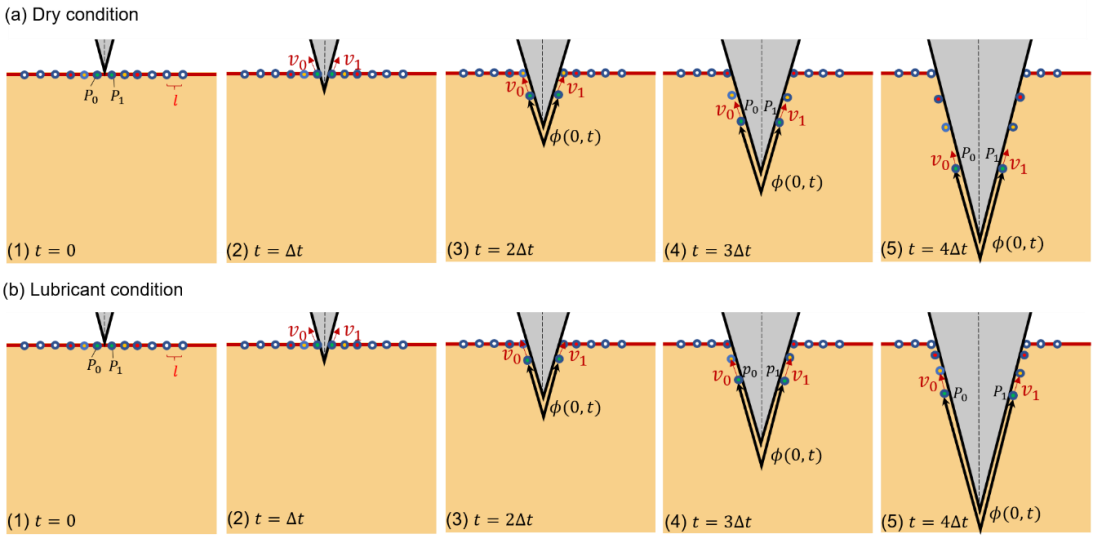

Fig. 4.14 The schematic diagram of the influence of wall-slip velocity on surface expansion distribution under (a) dry and (b) lubricant conditions

To quantitatively show the influence of the lubricity on the surface expansion distribution, Fig. 4.15 shows the distribution of the surface expansion distribution $\phi(x,t)$ at the indentation depth of 5 mm, namely at $t = 50$ s, along the indenter face with and without lubrication. These results demonstrate a significant increase of almost 76% in the surface expansion ratio near the indenter tip due to the effect of the lubricant, confirming that variations in frictional conditions at the interface affect the distribution of the surface expansion ratio. This insight also introduces a method for quantitative evaluation, moving beyond traditional qualitative assessments.

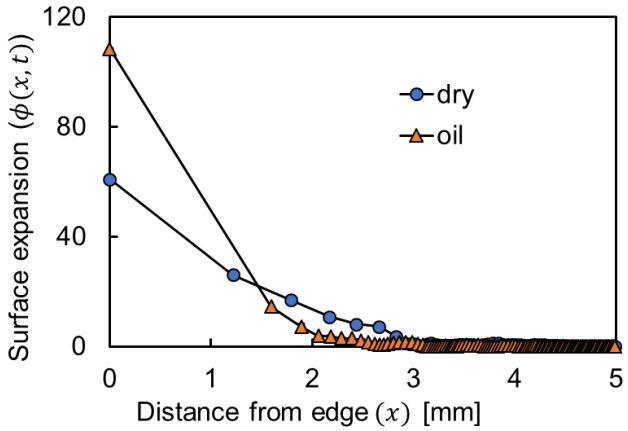

Fig. 4.15 The comparison of surface expansion distribution $\phi(x,t)$ with and without lubricants at the given time t of 50 s

Moreover, Fig. 4.16 compares the specific surface expansion ratio distribution, $\phi_s(x,t)$, which was defined as the following equation, with and without the presence of the lubricant.

$$\phi_s(x,t) = \frac{\phi(x,t)}{\phi(0,t)} \tag{4.8}$$

This figure further demonstrates that the surface expansion distribution under the oil condition becomes more localized and less diffused compared to that under the dry condition. In other words, oil lubricants reduce interface friction, enabling increased wall-slip velocity between the indenter and material at the interface in the vicinity of the indenter tip. This, in turn, triggers pronounced localized surface expansion. To put it simply, more localized surface expansion ratio in the vicinity of indenter tip compared to that under dry condition, indicates a higher wall-slip velocity at the interface, which reflects smaller interfacial friction.

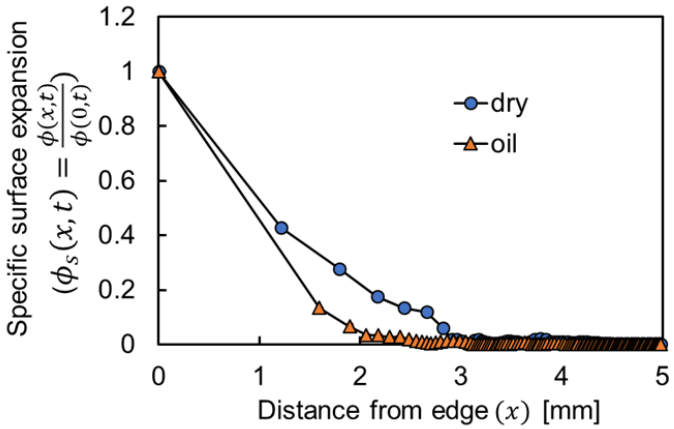

Fig. 4.16 The comparison of specific surface expansion ratio distribution $\phi_n(x,t)$ with and without lubricants at the given time t of 50 s

Building on the discussion above, it may be feasible to quantitatively assess the lubricating efficiency of lubricants under severe sliding contact by evaluating the material deformation behavior at the material-indenter interface, suggesting the potential to gauge tribological conditions in sliding contact scenarios. The reduction in interface friction due to improved tribological conditions—such as effective lubrication and optimal tool surface coatings—leads to an increase in wall-slip velocity, resulting in highly localized surface expansion near the indenter edge. Characterizing this surface expansion distribution, along with its relationship to wall-slip velocity, offers a robust method for quantitatively assessing variations in interface tribological conditions.

4.5 Summary

Interface friction is fundamental to tribology, which has considerable impact on the tribological phenomena in machining and forming processing. This chapter focuses on the relationship between interface friction and plastic boundary layer phenomenon, as well as surface expansion distribution, by using high-speed imaging and particle image velocimetry techniques. The key findings and conclusions are summarized as follows:

(1) The friction-induced plastic deformation flow observed in the vicinity of the severe sliding contact is very similar to a laminar fluid boundary layer, albeit distinct due to the presence of wall-slip velocity.

(2) The interface friction primarily determines the wall-slip behaviors at the interface, which subsequently determines the bulk deformation of the material, i.e., the plastic boundary layer structure.

(3) Non-uniform surface expansion distribution results from the difference in the wall-slip velocity along the sliding surface caused by the interface friction. Since the surface expansion distribution also determines the degree of the exposure of freshly generated nascent surface and subsequently influences interface friction, it can be said that interface friction, wall-slip velocity, and surface expansion distribution interact with each other.

(4) Improved tribological conditions, such as the application of effective lubricants at the interface, can enhance wall-slip velocity by reducing interface friction. This reduction, in turn, causes the surface expansion distribution to become more localized near the indenter tip in the indentation setup. Consequently, it may be feasible to quantitatively assess tribological conditions at the sliding contact by evaluating the deformation behavior of the material at the material-indenter interface.

Chapter 5 Comprehensive exploration of friction model and stress distribution in metal indentation

5.1 General introduction

The previous chapter aimed to obtain a comprehensive understanding of the tribological phenomena at the interface during indentation by investigating the interrelated relationship between interface friction and deformation behavior, including surface expansion distribution and wall-slip behavior. This exploration enables a thorough analysis of tribological phenomena in indentation by fully studying the stress conditions at the interface, including the distribution of normal and friction stresses. This advancement consequently facilitates more comprehensive discussions and potential developments in engineering applications.

Hence, this chapter aims to further explore the quantitative relationship between surface expansion distribution and stress distribution and propose a practical friction model to quantify stress distribution, including both friction and normal stress distribution. It also calculates and verifies quantitative results for stress distribution by using single-grooved indenters. Moreover, based on the comprehensive advancements between friction phenomena and surface expansion behavior, we also propose the potential implications for engineering applications.

5.2 Review of stress distribution

Stress distributions at the tool/die-workpiece interface are crucial for a comprehensive understanding of material deformation and tribological phenomena. It is widely acknowledged that to achieve a full understanding of these phenomena at the interface, it is essential to determine the stress distributions, specifically the distribution of friction stress and normal stress along the interface [152]. For example, friction stress at the interface significantly affects the sliding of the tool and workpiece, generating shear forces that act tangentially to the bulk material and thereby influencing the material deformation behavior and flow characteristics [153]. Conversely, normal stress is a critical parameter in determining whether a material will yield or deform plastically. Higher normal stresses can lead to earlier yielding and the initiation of plastic deformation, resulting in localized plastic deformation or concentrated strain, which may cause material defects and subsequently affect the entire forming operation [154].

Additionally, understanding the friction model, coupled with stress distribution derived from actual deformation behavior, plays a crucial role in identifying stress concentrations and preventing surface defects in various metal forming operations. During processes such as drawing, rolling, and extrusion, materials flow through dies under pressure. Any irregularities in this flow can lead to surface stress concentrations. Moreover, rapid deformation can subject the material to

high strain rates that exceed its plastic deformation capacity, potentially causing cracking [4]. For instance, extrusion is a manufacturing process used to produce objects with a consistent cross-sectional profile by pushing or drawing material through a die of the desired shape and Fig. 5.1 illustrates a schematic of the extrusion process (Fig. 5.1 (a)), associated with the geometric variables involved in extrusion (Fig. 5.1 (b)).

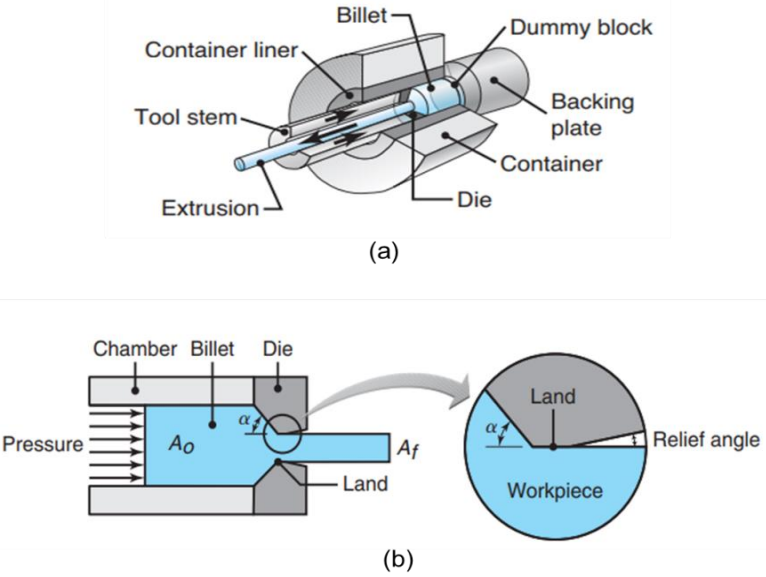

Fig. 5.1 (a) Schematic of the extrusion process and (b) the geometric variables in extrusion [4]

In a metal extrusion process, metal from a workpiece with a specific cross-section is pushed through a die with a smaller cross-section to form an extruded part. Understanding the material flow during this process is crucial. As the metal is forced towards and through the die, it undergoes deformation and consolidation. Due to friction at the die-workpiece interface, the outer layers deform more than those nearer to the center. The shear stress generated by varying friction at this interface impedes material flow near the die surface, resulting in greater material displacement and plastic deformation in sections close to the interface. In contrast, material closer to the center moves more swiftly through the die, attaining higher velocities relative to the die surface. Improper material flow can result in uneven deformation and localized stresses. The central region of the billet may experience less smooth flow compared to the outer regions (close to the interface), leading to stress concentration and potential cracking. Center cracking, or central burst, a critical concern, is particularly challenging to detect as it occurs internally during extrusion [4]. Understanding the mechanisms behind center cracking necessitates a thorough comprehension of metal flow dynamics during the extrusion process. Fig. 5.2 illustrates the zones

of rigidity and plasticity in extrusion with the occurrence of center cracking. Significant disparities in metal displacement between the central and outer regions can generate elevated internal stresses. These stress differentials can precipitate internal cracks, known as center cracking or burst. Addressing this issue effectively requires a detailed understanding of how stress distribution at the interface affects both localized and bulk deformation.

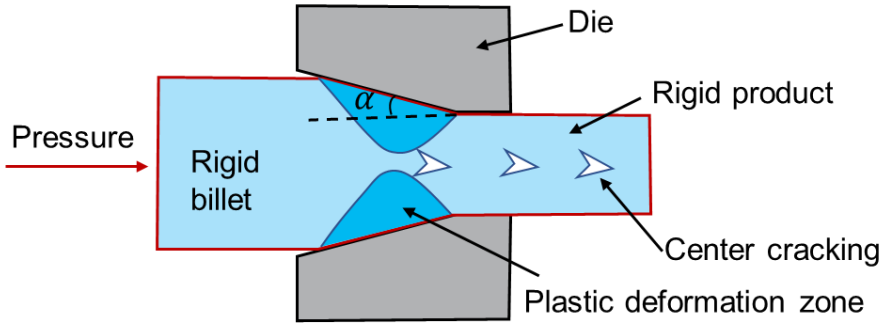

Fig. 5.2 Schematic of zones of rigidity and plasticity in extrusion with the occurrence of center cracking

Given the importance of stress distribution at the interface in metal plastic processes, a variety of experimental techniques have been developed to elucidate stress distribution along the interface. These techniques include photoelastic methods, split-tool tests, and experimental slipline field methods [93, 101, 154]. Fig. 5.3 presents experimental results on the contact stress distribution obtained by different researchers [152]. Although these scholars have obtained stress distributions at the interface using various methods, these efforts are insufficient for a full understanding of tribological phenomena. Firstly, most results are derived from specific processing environments using complex and inefficient equipment, thereby satisfying only the stress distribution under particular conditions [93]. Additionally, many of these results provide only qualitative analysis, and some even show opposite trends despite using the same methods [101]. Clearly, there is still a lack of quantitative friction models on stress distribution in metal cutting and forming processes due to the extreme difficulty in characterizing the complex friction conditions at the interface.

In summary, a new quantitative model of stress distribution for metal plastic deformation is crucial for comprehensive analysis the tribological conditions at the interface, facilitating a broad range of implications for engineering applications. This is a main issue that our studies plan to resolve through wedge indentation.

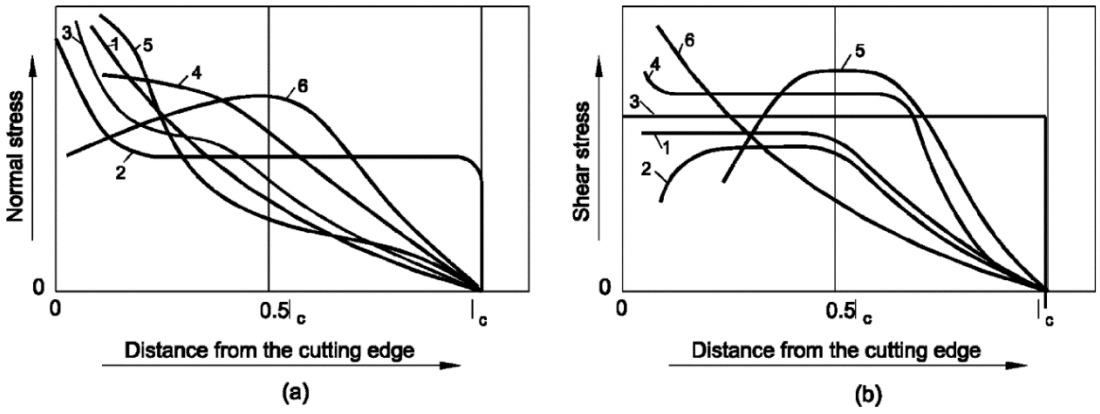

Fig. 5.3 Stress distributions in literature: (a) normal stress and (b) shear stress [152]

5.3 The determination of friction stress distribution

To propose the friction model for the friction stress distribution, first we need to discuss the relationship between friction force and adhesion force under the current indentation configuration and material properties. Typically, friction surfaces consist of numerous micro-convex peaks and valleys, known as asperities. The friction force F_f at the interface arises from plowing and adhesion effects [25], expressed as:

$$F_f = F_a + F_p \tag{5.1}$$

where F_a and F_p are the adhesion force and plowing force at the interface respectively. Under the current indentation configuration and material properties, the indenter was meticulously polished, and the workpiece material—annealed aluminum—was significantly softer than the high-speed steel indenter. This disparity in hardness renders the plowing force negligible in comparison to the adhesion force. Under these conditions, the friction force nearly equals the adhesion force. In other words, the proposal for the friction stress distribution in this section builds upon the discussions of adhesion stress distribution presented in Chapter 3. Therefore, friction stress τ_f could also be expressed as a function of surface expansion distribution $\phi(x)$, given by:

$$\tau_f = \tau_a = \begin{cases} k\phi(x) & (k\phi(x) < m\tau_s) \\ m\tau_s & (k\phi(x) \geq m\tau_s) \end{cases} \tag{5.2}$$

In this scenario, the friction stress distribution could be quantitatively calculated based on the deductions in Chapter 3, as shown in Fig. 5.4. Note that these values in this figure simply represent the predicted results obtained from Fig. 3.13. The findings reveal that under larger

indentations, the friction stress near the indenter tip reaches its maximum value, namely the shear yield stress of the material. This underscores the significant influence of adhesion friction near the indenter edge. Conversely, under low indentation depths, sliding friction predominantly governs the interface in the metal forming process.

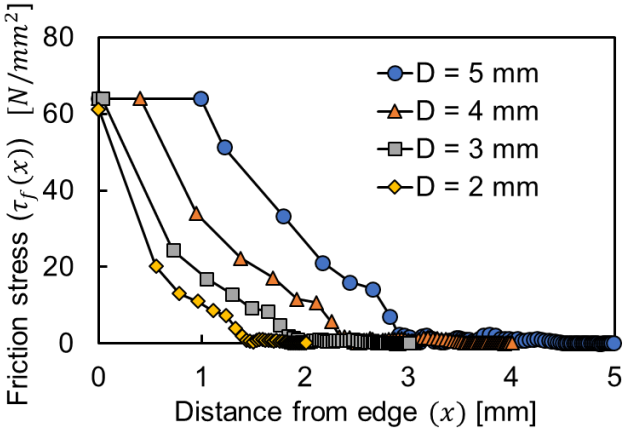

Fig. 5.4 The friction stress distribution under different indentation depth

5.4 The determination of normal stress distribution

5.4.1 Challenges and approaches

Quantifying normal stress distribution in metal forming and machining is challenging due to the nonlinear stress-strain behavior of materials during these processes. This nonlinearity complicates accurate prediction and measurement of normal stress distribution. Furthermore, direct real-time measurement of normal stresses is complex, often requiring embedded sensors in the tool or workpiece, which can interfere with the process. Indirect techniques, such as photoelasticity, provide some insight but with the limitation on the materials to which it can be applied or precision necessary for detailed stress mapping [93, 155]. Inevitably, the current indentation configuration faces the same challenges in characterizing normal stress behavior. However, a thorough analysis of tribological phenomena during metal plastic processes would greatly benefit from an in-depth investigation of normal stress conditions at the interface, emphasizing the urgent need for precise friction models to describe stress distribution based on the current indentation configuration and material properties.

Under conventional sliding contact conditions, Coulomb's law describes the relationship between normal pressure and friction force (Eq. 1.1). However, due to the complex contact conditions in the present indentation configuration, the friction behavior along the entire interface deviates from Coulomb's law, underscoring the difficulty in directly quantifying the

normal stress distribution. Nevertheless, if the ratio, defined as $\mu(x)$, between friction stress ($\tau_f(x)$) and normal stress ($\sigma_n(x)$) is established, we can indirectly obtain the value of the normal stress distribution, as expressed in Eq. 5.3, since we have quantitatively calculated the friction stress distribution in the previous section. Note that, unlike the constant μ in conventional Coulomb's law (Eq. 1.1), $\mu(x)$ in Eq. 5.3 varies depending on the contact conditions at each location.

$$\mu(x) = \frac{\tau_f(x)}{\sigma_n(x)} \tag{5.3}$$

The question that remains is how to obtain $\mu(x)$. The discussions in the previous chapters have illustrated the strengths and capabilities of PIV in quantifying deformation behavior. If $\mu(x)$ can be demonstrated to be a function of deformation parameters, such as strain or strain rate, then we can compute $\mu(x)$ without needing to directly measure pressure and friction values. This represents a significant breakthrough in obtaining the normal stress distribution. The traditional theory of plastic mechanics, specifically the Prandtl–Reuss equations [156], provides a framework for computing $\mu(x)$. Fig. 5.5 summarizes the procedure for deducing the normal stress distribution by determining $\mu(x)$ and $\tau_f(x)$ in each section. Sections 5.4.2 and 5.4.3 will subsequently focus on explaining the Prandtl–Reuss equations and their application in calculating $\mu(x)$.

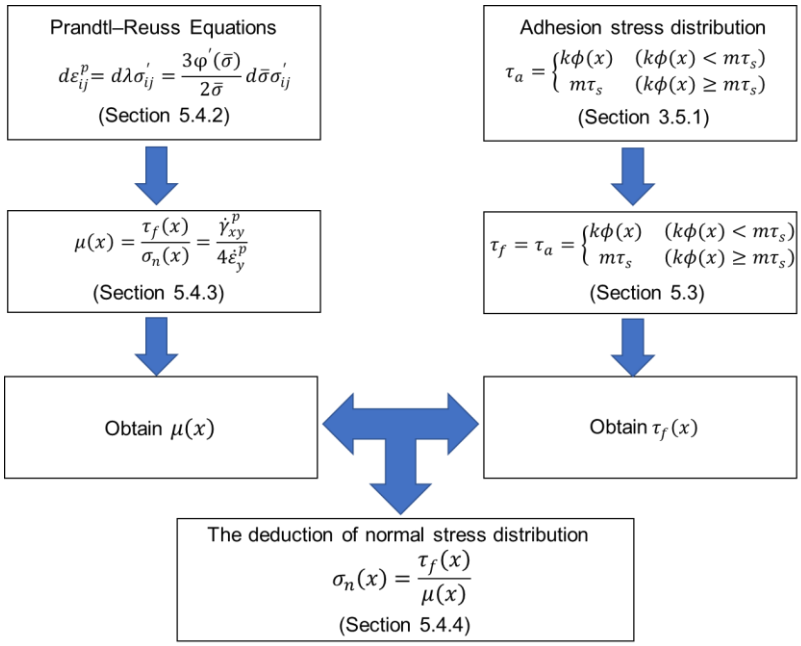

Fig. 5.5 The summary of the procedure to deduce normal stress distribution

5.4.2 The explanation of Prandtl–Reuss Equations

Prandtl-Reuss Equations, also known as the flow rule in plasticity theory, are commonly used to describe the relationship between stress and strain in the plastic deformation of materials [156-157]. They are simplified according to the following assumptions:

(1) An isotropic, homogeneous, ideally plastic material, obeying the von Mises yield criterion;
(2) The deforming material adheres to the principle of volume constancy during plastic deformation;
(3) The principal axes of plastic strain increment and deviatoric stress are coincident, following the normality rule.

Since metal indentation belongs to metal plastic process and the flow rule obeys the normality condition, we assume the plastic deformation theory during indentation follows Prandtl–Reuss Equations.

According to Prandtl–Reuss Equations, the total strain increment $d\varepsilon_{ij}$ is the sum of the elastic strain increment $d\varepsilon_{ij}^{e}$ and the plastic strain increment $d\varepsilon_{ij}^{p}$, written as:

$$d\varepsilon_{ij} = d\varepsilon_{ij}^{e} + d\varepsilon_{ij}^{p} \qquad \text{with} \quad d\varepsilon_{ij}^{p} = d\lambda\sigma_{ij}' \tag{5.4}$$

where σ_{ij}' is the deviatoric stress, in which i, j are assumed to take their values in the set {1, 2, 3} and $d\lambda$ is a factor of proportionality that shows the relationship between the strain increment and deviatoric stress. Since plastic deformation takes place with zero volume change, i.e., the material is incompressible, mean normal strain increment $d\varepsilon_{m}$ is zero, so that plastic strain increment $d\varepsilon_{ij}^{p}$ reduces to:

$$d\varepsilon_{ij}^{p} = d\varepsilon_{m}\delta_{ij} + \ de_{ij}^{p} = de_{ij}^{p} = d\lambda\sigma_{ij}' \tag{5.5}$$

where de_{ij}^{p} is the deviatoric strain increment and Kronecker's delta δ_{ij} is defined as:

$$\delta_{ij} = 1 \quad when\ i = j$$
$$\delta_{ij} = 0 \quad when\ i \neq j$$

According to Eq. 5.5, gives:

$$d\varepsilon_{ij}^{p} d\varepsilon_{ij}^{p} = de_{ij}^{p} de_{ij}^{p} = d\lambda^{2}\sigma_{ij}'\sigma_{ij}' \tag{5.6}$$

Noting that effective strain increment and effective stress could be expressed as follows:

$$\overline{d\varepsilon} = \sqrt{\frac{2}{3}\, de_{ij}^{p}\, de_{ij}^{p}} \qquad \bar{\sigma} = \sqrt{\frac{3}{2}\sigma_{ij}'\sigma_{ij}'} \tag{5.7}$$

Thus,

$$\mathrm{d}\lambda = \frac{3\overline{d\varepsilon}}{2\bar{\sigma}} \tag{5.8}$$

Eq. 5.8 indicates that $\mathrm{d}\lambda$ remains consistent regardless of variations in normal and shear strain increments or deviatoric normal and shear stress under the same indentation condition. The discussion on the Prandtl–Reuss Equations presented above assumes an ideal elastic-perfectly plastic material. However, it is important to note that material strain hardening is a significant phenomenon in metal plastic deformation. Strain hardening, also referred to as work hardening, is a process through which a material gains hardness and strength as a result of plastic deformation, and it encompasses several forms of hardening in plastic deformation applications. The Prandtl–Reuss Equations presuppose isotropic material behavior and adhere to the isotropic hardening rule. Given that aluminum alloys typically exhibit strain hardening and the load during indentation maintains a consistent direction, it is reasonable to assume that the strain hardening model during indentation follows the isotropic hardening rule. In this scenario, the resultant yield condition can be expressed as follows:

$$f(\sigma_{ij}, H) = 0 \tag{5.9}$$

where the function of f represents the yield surface and H is the hardening parameter which is a function of effective strain $\bar{\varepsilon}$, written as:

$$H = H(\bar{\varepsilon}) \qquad \bar{\varepsilon} = \int \overline{d\varepsilon} \tag{5.10}$$

Assuming Yield criterion obeys Mises yield criterion, gives:

$$\bar{\sigma} - \sigma_s - H\left(\int \overline{d\varepsilon}\right) = 0 \qquad \text{or} \qquad \int \overline{d\varepsilon} = \varphi(\bar{\sigma}) \tag{5.11}$$

where σ_s is the yield strength of the material and φ is the inverse function of H, dependent on $\bar{\sigma}$. So that the effective strain increment $\overline{d\varepsilon}$ can be represented as:

$$\overline{d\varepsilon} = \varphi(\bar{\sigma})d\bar{\sigma} \tag{5.12}$$

then

$$\mathrm{d}\lambda = \frac{3\varphi'(\bar{\sigma})}{2\bar{\sigma}}d\bar{\sigma} \tag{5.13}$$

Eq. 5.13 clearly indicates that proportionality factor of strain increment and deviatoric stress, denoted as $d\lambda$, is a function of effective stress $\bar{\sigma}$ and remains no time dependence. In other words, under the same indentation condition, $\mathrm{d}\lambda$ remains constant. This establishes the groundwork for quantitatively describing the relationship between interface phenomena and deformation behavior.

5.4.3 The ratio of friction stress to normal stress

The preceding section elaborates on the Prandtl–Reuss Equations, which elucidate the correlation between strain increment and deviatoric stress. In plastic processes, it is typical for an elastic strain component to persist beyond the elastic limit alongside the plastic strain and plastic strain component is usually significantly larger than elastic strain component. In such case, Prandtl–Reuss Equations could be modified and are called Levy-Mises Equations [158]. Compared to Prandtl–Reuss Equations, Levy-Mises Equations assumes no elastic deformation occurs. Fig. 2.6 depicts the variations in force during indentation. Notably, the force changes illustrated in Fig. 2.6 (c), where cessation occurs one second after indentation to allow for the recovery of elastic deformation, suggest that the force generated during indentation primarily constitutes plastic deformation force. This implies that the plastic strain component is substantial, while the elastic strain component is negligible, following Levy-Mises Equations. That is:

$$d\varepsilon_{ij}^{p} = d\lambda\sigma_{ij}' = \frac{3\varphi'(\bar{\sigma})}{2\bar{\sigma}}d\bar{\sigma}\sigma_{ij}' \tag{5.14}$$

Thus, the normal strain increment $d\varepsilon_{ii}^{p}$ could be described by:

$$d\varepsilon_{ii}^{p} = d\lambda\sigma_{ii}' = d\lambda(\sigma_{ii} - \sigma_m) \tag{5.15}$$

where σ_m is the hydrostatic stress and equal to the average of the normal stress, written as:

$$\sigma_m = \frac{\sigma_{ii}}{3} \tag{5.16}$$

Since experiments are performed under plane strain condition, and Fig. 5.6 (a) is the schematic of the stress components of plane strain state at a point near the indenter surface, in which σ_x and σ_y is the normal stress of different direction and τ_{xy} is the shear stress at the interface, then according to Eq. 5.15, the normal strain increment $d\varepsilon_z^p$, which equals to zero under plane strain condition, could be expressed as:

$$d\varepsilon_z^p = d\lambda\sigma_z' = d\lambda(\sigma_z - \sigma_m) = d\lambda(\sigma_z - \frac{\sigma_x + \sigma_y + \sigma_z}{3}) = \frac{2}{3}d\lambda(\sigma_z - \frac{\sigma_x + \sigma_y}{2}) = 0 \quad (5.17)$$

that means:

$$\sigma_z = \frac{\sigma_x + \sigma_y}{2} \quad (5.18)$$

In such case, the deviatoric stress σ_y' could be obtained as:

$$\sigma_y' = \sigma_y - \sigma_m = \sigma_y - \frac{\sigma_x + \sigma_y + \sigma_z}{3} = \frac{\sigma_y - \sigma_x}{2} \quad (5.19)$$

Fig. 5.6 (b) depicts the schematic of force distribution at the tool-workpiece interface. Given that material flow in narrow-wedge indentation is primarily induced by interface friction [133], the material predominantly experiences the friction force F_f and normal force F_n exerted by the indenter. Consequently, there is minimal or negligible tension or compression effects along the x-axis. In other words, σ_y is much larger than σ_x since σ_x is generated by the tension or compression effects, then σ_y' reduces to:

$$\sigma_y' = \sigma_y - \sigma_m \approx \frac{\sigma_y}{2} \quad (5.20)$$

Levy-Mises Equations give:

$$d\varepsilon_y^p = d\lambda\sigma_y' = \frac{3\varphi'(\bar{\sigma})}{2\bar{\sigma}}d\bar{\sigma}\frac{\sigma_y}{2} \quad (5.21)$$

$$d\varepsilon_{xy}^p = d\lambda\sigma_{xy}' = \frac{3\varphi'(\bar{\sigma})}{2\bar{\sigma}}d\bar{\sigma}\tau_{xy} \quad (5.22)$$

Thus,

$$\tau_{xy} \approx \frac{d\varepsilon_{xy}^{p}}{2d\varepsilon_{y}^{p}}\sigma_{y} \tag{5.23}$$

since

$$d\varepsilon_{xy}^{p} = \frac{d\gamma_{xy}^{p}}{2} \tag{5.24}$$

where $d\gamma_{xy}^{p}$ is engineering shear strain increment, then

$$\tau_{xy} \approx \frac{\dot{\gamma}_{xy}^{p}}{4\dot{\varepsilon}_{y}^{p}}\sigma_{y} \tag{5.25}$$

in which τ_{xy} is equal to friction stress τ_f and σ_y is equal to normal stress σ_n, so that the ratio of friction stress to normal stress, defined as μ, could be expressed as:

$$\mu(x) = \frac{\tau_f(x)}{\sigma_n(x)} = \frac{\dot{\gamma}_{xy}^{p}}{4\dot{\varepsilon}_{y}^{p}} \tag{5.26}$$

where $\tau_f(x)$ and $\sigma_n(x)$ are the distribution of friction stress and normal stress along the interface, while $\dot{\gamma}_{xy}^{p}$ and $\dot{\varepsilon}_{y}^{p}$ are the corresponding distribution of shear strain increment and normal strain increment, which can be calculated through PIV analysis. Specifically, the PIV analysis provides a grid of velocity vectors over the field of view [127], used to compute the strain rate components ($\dot{\varepsilon}_h, \dot{\varepsilon}_v, \dot{\gamma}_{hv}$), in which h-axis and the v-axis represent the horizontal and vertical direction, respectively, as shown in Fig. 5.6 (c). Based on the principle of the transformation of an Eulerian strain tensor with a rotation angle of α in the orthogonal axes from v-axis to x-axis (Fig. 5.6 (c)) [159], $\dot{\gamma}_{xy}^{p}$ and $\dot{\varepsilon}_{y}^{p}$ could be calculated through PIV as:

$$\dot{\varepsilon}_{y}^{p} = \frac{\dot{\varepsilon}_h + \dot{\varepsilon}_v}{2} + \frac{\dot{\varepsilon}_h - \dot{\varepsilon}_v}{2} cos\, 2\alpha + \frac{\dot{\gamma}_{hv}}{2} sin\, 2\alpha \tag{5.27}$$

$$\dot{\gamma}_{xy}^{p} = (\dot{\varepsilon}_v - \dot{\varepsilon}_h)\, sin\, 2\alpha + \dot{\gamma}_{hv} \cos 2\alpha \tag{5.28}$$

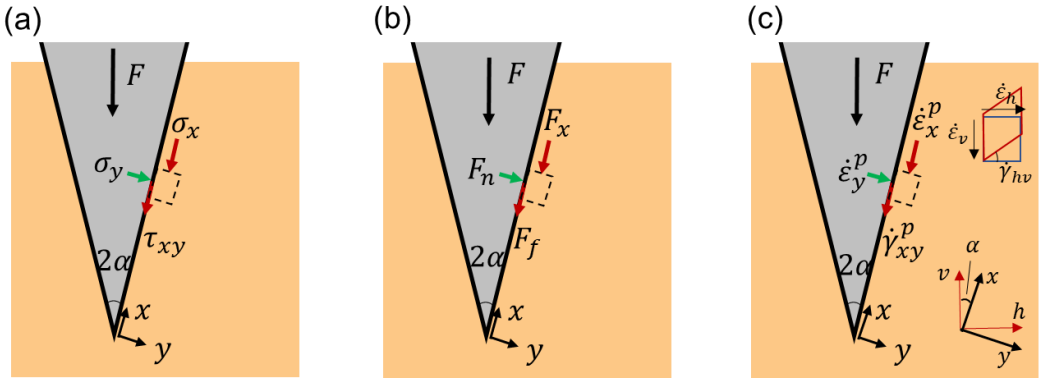

Fig. 5.6 The schematic of the (a) stress component of plane strain state, (b) distribution of force at a point near the indenter surface and (c) strain rate increments state

Eq. 5.26 clearly shows the quantitative relationship between the tribological phenomenon and deformation field at the interface and Fig. 5.7 is the experimental results of the ratio of friction stress to normal stress $\mu(x)$ at indentation depths of 2, 3, 4, and 5 mm. It reveals that at low indentation depths, the ratio of friction stress to normal stress, namely $\mu(x)$, remains relatively constant at a certain value. However, as the indentation depth increases, $\mu(x)$ gradually rises before stabilizing. This phenomenon occurs because, at greater indentation depths, the pressure near the indenter tip becomes exceptionally high. At this point, the friction stress equates to the shear yield stress near the indenter tip and subsequently decreases with increasing distance from the indenter tip. Meanwhile, the normal stress is at its maximum at the tool tip and gradually diminishes to zero. Consequently, the trend line of $\mu(x)$ remains consistent at low indentation depths but gradually increases near the indenter tip before stabilizing at higher indentation depths. These findings, coupled with the friction stress distribution, establish the groundwork for quantifying normal stress distribution.

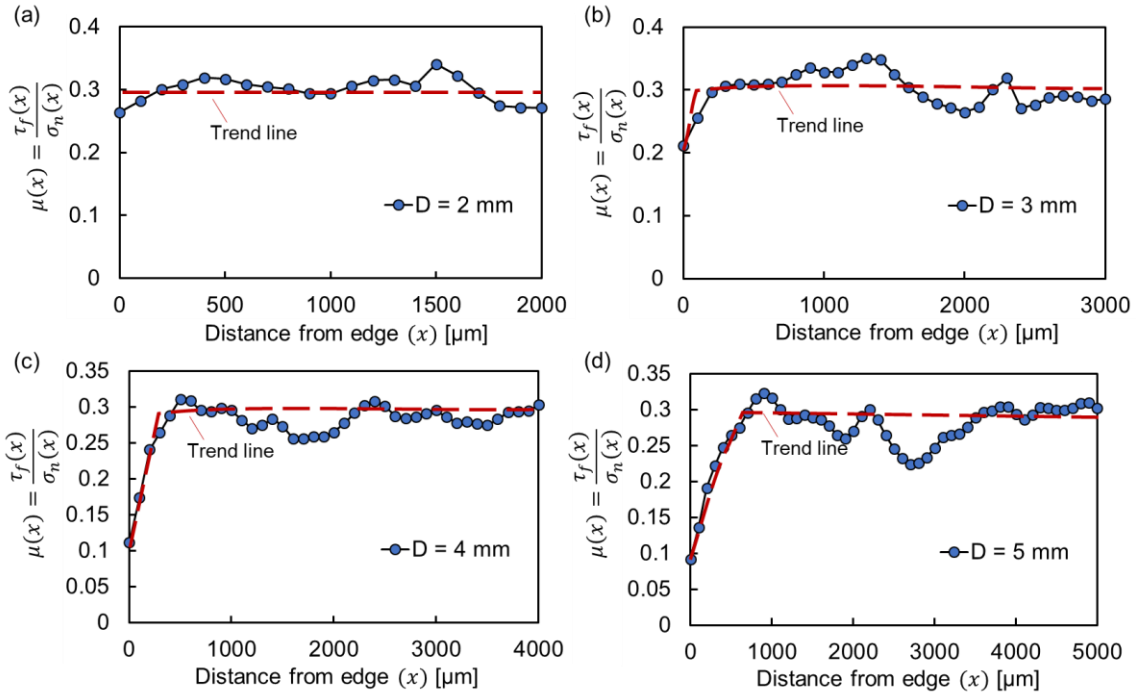

Fig. 5.7 The distribution of the ratio of friction stress to normal stress $\mu(x)$ at different indentation depths

5.4.4 Determination and discussion

Building upon the preceding sections, both $\tau_f(x)$ and $\mu(x)$ have been quantitatively determined, as shown in Figs 5.4 and 5.7, respectively. Under these conditions, the normal stress distribution can be derived based on Eq. 5.4, and Fig. 5.8 shows the normal stress distribution $\sigma_n(x)$ at indentation depths of 2, 3, 4, and 5 mm. It demonstrates that the normal stress at the interface is highest at the indenter tip and gradually diminishes with increasing distance from the tool edge, facilitating the quantification of the complex contact condition at the interface.

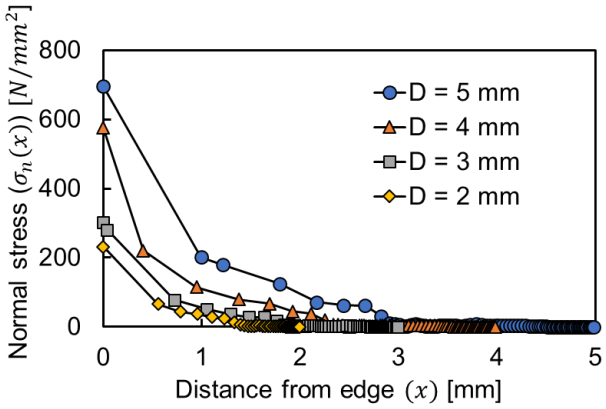

Fig. 5.8 The distribution of normal stress at different indentation depths

To validate the accuracy of the quantified normal stress distribution in Fig. 5.8, it is essential to verify the correctness and reasonableness of the model proposed in the previous sections. Given that the force measurement experiments in this study capture only the overall indentation force and the adhesion (or friction) force at the interface, the normal force at the interface cannot be measured directly.

As depicted in Fig. 5.9, the indentation force F is divided into two components: the penetrating force at the indenter edge, denoted as F_{edge}, and the force acting along the sides of the indenter, defined as F_{int}.The latter force, F_{int}, represents the combined effect of the normal and frictional forces at the interface on the indenter's side surface, which is the primary contributor to interface deformation. In other words, measured indentation force F or normal indenter is composed of interface indentation force F_{int} and edge indentation force F_{edge}, and can be expressed as:

$$F = 2F_{int} + F_{edge} \tag{5.29}$$

where F_{int} is the resultant force of interface friction force F_f and normal force F_n, namely the integral of τ_f and σ_n respectively, written as:

$$F_{int} = F_f \cos\alpha + F_n \sin\alpha = \int_0^{L_t} w\tau_f \cos\alpha dx + \int_0^{L_t} w\sigma_n \sin\alpha dx \tag{5.30}$$

Therefore, the predicted partial indentation force $F_{12\_predict}$ generated in the area between L_1 and L_2 on either side of the indenter surface (see Fig. 3.8), can be calculated based on τ_f and σ_n, as shown in Figs. 5.4 and 5.8, respectively. This force can be expressed as:

$$F_{12\_predict} = \int_{L_1}^{L_2} w\,(\tau_f \cos\alpha + \sigma_n \sin\alpha) dx \tag{5.31}$$

Similar to the indentation force of normal indenters, the measured indentation force of grooved indenters, defined as F_g, is divided into two components: the penetrating force at the indenter edge, denoted as F_{g_edge}, and the force acting along the sides of the indenter, defined as F_{g_int}. Ideally, under identical conditions, the penetrating force at the indenter edge for both the normal and single-grooved indenters—denoted as F_{edge} and F_{g_edge}, respectively—should be equal. This is because both indenters should experience similar edge contact characteristics, unaffected by the groove's presence on the indenter face. Consequently, any difference in the total indentation forces between the two types of indenters would be primarily due to variations in the

interface forces along the sides of the indenter rather than at the edge. In other words, the measured indentation force of the single-grooved indenters, F_g, can be expressed as:

$$F_g = 2F_{g\_int} + F_{g\_edge} = 2F_{g\_int} + F_{edge} \tag{5.32}$$

By measuring the indentation force for normal indenter and single groove indenter, the experimental indentation force F_{12} partially generated in the area between L_1 and L_2 on either side of indenter face can be calculated by:

$$F_{12} = F_{int} - F_{g\_int} = \frac{F - F_g}{2} \tag{5.33}$$

If we define mean indentation stress distribution as $\tau(x)$, then mean indentation stress $\tau(x_m)$ at the mid point of micro-groove, x_m, could be calculated as follows:

$$\tau(x_m) = \frac{F_{12}}{w(L_2 - L_1)} = \frac{\int_{L_1}^{L_2} \tau(x)dx}{L_2 - L_1} \tag{5.34}$$

In this context, F and F_g represent the indentation forces measured for the normal indenter and the single-groove indenter, as illustrated in Figs. 5.9 (b) and (c), respectively. If the stress distribution model proposed in the previous section is accurate, then this experimentally derived partial indentation force in the area between L_1 and L_2 on either side of indenter face, F_{12} (Eq. 5.33), should be close to $F_{12\_predict}$, obtained from the calculated values of τ_f and σ_n (see Figs. 5.4 and 5.8). This comparison will serve as a validation of the proposed model's correctness and reliability in characterizing the normal stress distribution.

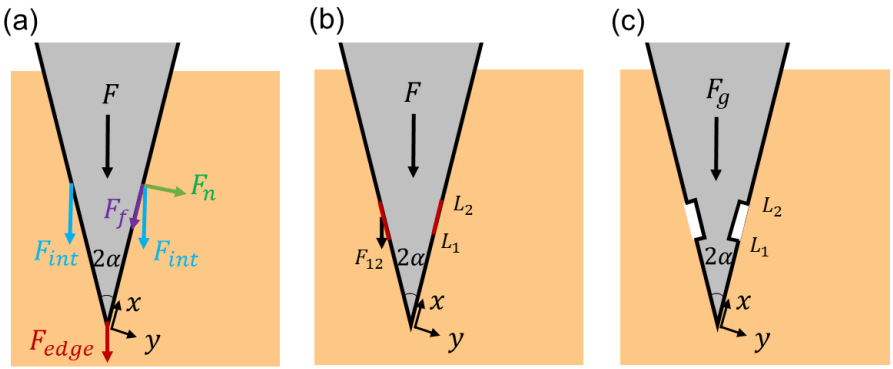

Fig. 5.9 The schematic diagram of the (a) force distribution (b) normal indentation force and (c) single-groove indentation force

In Fig. 5.10, the comparison between the experimentally determined partial indentation force F_{12} and the predicted partial indentation force $F_{12\_predict}$ is shown. The black straight line in the figure serves as a reference, indicating the range where $F_{12} = F_{12\_predict}$. The results indicate that the experimental indentation force is proportional and nearly equal to the predicted force, with most of the experimental indentation forces being smaller than those of the predicted partial indentation forces. This phenomenon arises due to the presence of the second cutting effect, which increases the value of indentation force for groove indenters [160]. Consequently, the experimental indentation stress is smaller, and the effects of second cutting become more pronounced with increasing indentation depth. These findings unequivocally validate the accuracy of the stress distribution. Furthermore, we obtain the indentation stress distribution $\tau(x)$ at indentation depths of 2, 3, 4, and 5 mm based on Figs. 5.4 and 5.8, alongside the experimentally derived mean indentation stress values (Eq. 5.34) in Fig. 5.11. As illustrated in Fig. 5.11, the predicted indentation stress distributions closely match the experimental data, with the experimental indentation stress being slightly smaller than the predicted value. This further confirms the reliability of the quantitative stress distribution model.

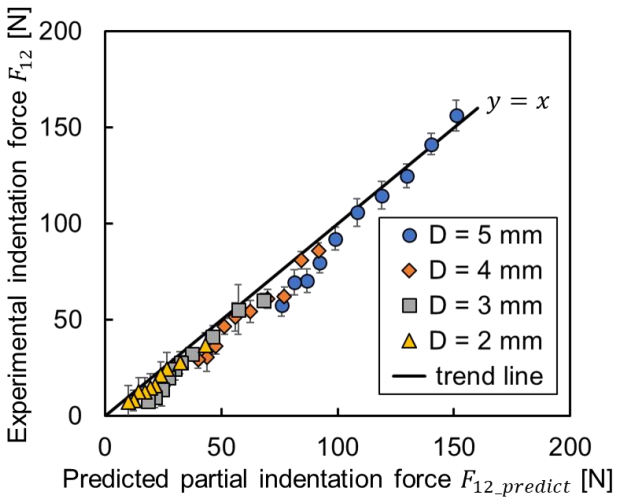

Fig. 5.10 The comparison of experimental and predicted partial indentation force F_{12}

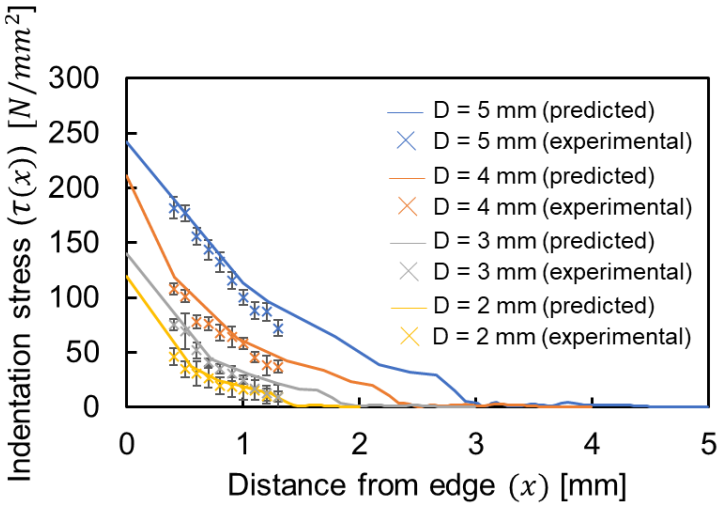

Fig. 5.11 The comparison between experimental results and predicted indentation stress

In summary, our research proposes the friction model based on the response of actual deformation during indentation, marking a key breakthrough in the comprehensive understanding of tribological phenomena at the interface. This model quantifies the effects of interface friction on plastic flow, facilitating further discussion on this topic. Additionally, this advancement led to the proposal of a quantitative method for evaluating the tribological conditions at the sliding contact, which we believe represents a significant application of our research findings. Undoubtedly, a thorough comprehension of tribological phenomena through quantitative exploration of their relationship with deformation behavior in wedge indentation clearly facilitates advancements across diverse forming processes. The focal objective lies in designing novel model systems that better correspond to various forming techniques, thereby representing a substantial stride forward in the practical application of current research findings.

Undeniably, our friction model has certain limitations, and several assumptions were made, particularly in the normal stress distribution model. For instance, we applied classical plasticity theory to analyze the relationship between stress and strain during deformation, neglecting the effects of elastic deformation. While plastic deformation typically dominates in most forming processes, elastic deformation is inevitably present. Ignoring this aspect could impact the model's accuracy. Therefore, future research focusing on incorporating elastic deformation into the current model will likely enhance both its precision and reliability. Additionally, our models, including friction stress distribution and normal stress distribution, are primarily based on discussions involving the application of 30-degree wedge indenters, where the deformation field is known to be influenced by friction. Therefore, while the model is suitable for most cases of deformation induced by friction, it may not be directly applicable to cases of

deformation induced by pressure, such as those near a 120-degree indenter. Nevertheless, by varying the indenter angle, we have successfully replicated and studied deformations induced by compressive stresses. While we have not extensively explored the influence of tribological phenomena corresponding to this aspect of deformation, the research methodology employed in our study provides a framework to potentially investigate these aspects of the model. This highlights opportunities for further research and development aimed at expanding the applicability and comprehension of our friction models.

5.5 Summary

Stress distribution is fundamental to understand tribological phenomena and material deformation at contact surface. In this study, we focused on the quantitative relationship between the distribution of surface expansion and stress distribution by using wedge indentation and direct observation coupled with high-speed imaging and particle image velocimetry techniques. The main conclusions are summarized as follows:

(1) Under current indentation configuration and material, the friction force nearly equals the adhesion force during indentation due to the meticulously polished indenter, and the workpiece material significantly softer than the indenter. Consequently, the friction stress distribution could be determined based on the deductions of adhesion stress distribution.

(2) Based on the Prandtl–Reuss Equations, the ratio of friction stress to normal stress has been computed, exhibiting high consistency with the distribution of friction stress and laying the groundwork for quantifying normal stress distribution.

(3) The normal stress distribution has been quantitatively calculated based on the determination of friction stress distribution and the ratio of friction stress to normal stress. The stress distribution, encompassing both friction stress and normal stress, offers a deeper comprehension of extreme friction conditions at the interface in metal forming processes. This constitutes a significant advancement and breakthrough in fundamental research on metal forming processes, facilitating more comprehensive discussions and potential developments in engineering applications.

Chapter 6 Conclusions and recommendations

6.1 Summary of conclusions

In recent years, the demand for high-mix, low-volume manufacturing in metal forming processes has risen, alongside an increasing emphasis on high-quality production and cost-effective technologies. To meet these demands and effectively prevent surface defects, a comprehensive understanding of tribological phenomena at the interface is crucial. In this dissertation, we proposed a novel methodology to quantify deformation behavior—including surface expansion and wall-slip behavior—using Particle Image Velocimetry (PIV) analysis, to explore the quantitative influence of tribological phenomena on deformation at the interface. By investigating the quantitative relationship between tribological effects and deformation behavior, we developed new friction models based on surface expansion distribution, particularly suited for friction-induced deformation scenarios, such as narrow wedge indentation, where traditional pressure-based models prove inadequate. This breakthrough provides a deeper understanding of tribological phenomena at the interface by quantifying the effects of interface friction on plastic flow, facilitating further exploration of the topic. Moreover, this advancement enabled the development of a quantitative method for evaluating tribological conditions at the sliding contact, representing a significant practical application of our research findings. The following sections will summarize the results and findings obtained in each chapter of this study.

In Chapter 2, wedge indentation experiments are conducted as a model system to quantify deformation behavior and explore distinct tribological phenomena at the interface using PIV analysis. This chapter illustrates various deformation behaviors, such as velocity fields and material flow under diverse conditions, highlighting PIV's capability to capture the characteristics of severe plastic deformation. It demonstrates that existing friction models are inadequate for accurately describing these tribological phenomena, and it proposes the feasibility of new friction models based on observed deformation behavior. This chapter verifies the limitations of traditional friction models and suggests that surface expansion behavior offers significant potential for further exploration of adhesion phenomena. This underscores the necessity for a more detailed examination of the microscopic interactions occurring at the interface.

In Chapter 3, the quantitative relationship between adhesion phenomena and surface expansion behavior is proposed and new friction model for adhesion stress distribution is proposed building upon the characteristics of various plastic deformation fields and the influence of surface expansion on adhesion force outlined in Chapter 2. The chapter confirms that adhesion stress, $\tau_a(x)$, is proportional to the surface expansion ratio, $\phi(x)$, with a factor of k at relatively smaller surface expansion ratios. It reaches its maximum value, $m\tau_s$, when the condition $m\tau_s \geq$

$k\phi(x)$ is satisfied. The constants m ($0 < m \leq 1$) and k are determined by the processing conditions, and changes at the interface, such as the application of effective lubrication, can reduce the values of k and m. The findings reveal a strong consistency between the predicted adhesion stress distribution and the experimentally measured mean adhesion stress values, both with and without lubricants. This agreement enables the quantification of the friction model based on actual deformation behavior in metal forming processes, representing a significant breakthrough in the quantitative investigation of the relationship between tribological phenomena and deformation behavior.

In Chapter 4, the effects of friction on plastic deformation in both the metal surface and bulk are examined, particularly focusing on the factors contributing to the uneven distribution of surface expansion ratio. This analysis aims to achieve a comprehensive understanding of the correlation between tribological phenomena and deformation behavior, a topic not fully addressed in Chapter 3. The chapter demonstrates that interface friction, wall-slip velocity, and surface expansion distribution interact in complex ways. Furthermore, it suggests the possibility of quantitatively assessing the tribological conditions at the sliding contact by evaluating the material's deformation behavior at the material-indenter interface.

In Chapter 5, a comprehensive exploration of friction models and stress distribution in metal indentation is conducted, building upon the findings from Chapters 3 and 4. This chapter consolidates the analysis of stress distribution, including both friction stress and normal stress, to provide a deeper understanding of extreme friction conditions at the interface in metal forming processes. This represents a significant advancement and breakthrough in fundamental research, fostering more comprehensive discussions and potential developments in engineering applications.

6.2 Recommendations for future work

This dissertation quantifies the effects of tribological phenomena on metal deformation behavior utilizing direct in-situ observations coupled with high-speed imaging and PIV techniques. This advancement facilitated the development of a friction model that reflects actual deformation behavior, as well as a quantitative method for evaluating lubrication performance in practical forming processes. The following section provides recommendations and outlines potential directions for future work.

(1) Chapter 4 provides a brief discussion on how wall-slip velocity induced by interface friction leads to changes in the structure of boundary layer-like phenomena. However, detailed research on boundary layer phenomena remains limited, particularly regarding the relationship between boundary layer thickness, pseudo-viscosity, and other forms of deformation. Further investigation in this area is necessary to gain a deeper understanding of these complex interactions.

(2) Chapter 5 presents friction models based on actual deformation responses, including friction stress distribution and normal stress distribution. However, the discussion on the practical applications of these models is limited. For example, real-time monitoring and finite element analysis necessitate substantial quantitative data to validate and advance current developments in this field. Thus, exploring the applications of existing friction models across various contexts would be a promising direction for future research.

(3) The current research utilized wedge indentation experiments as a model system, primarily due to the deformation field near the contact interface during indentation closely resembling that observed in various plastic forming processes. This relevance extends to a broad range of applications. However, a gap persists between these models and actual forming processes such as forging, rolling, and extrusion. Therefore, the design of new model systems that more accurately align with various forming processes would represent a significant advancement in the application of the present findings.

(4) The present research delves into the impact of tribological phenomena on the plastic deformation of metals. However, the properties of metal materials comprise only a fraction of modern technological materials. Investigating tribological phenomena in the forming processes of other materials, such as the deformation behavior of difficult-to-machine materials, is expected to reveal significant variations. This suggests a promising avenue for future applications and extensions of this research.

(5) The current research heavily depends on high-speed photography technology. Continued advancements in this technology are poised to further augment the investigation of the quantitative effects of tribological phenomena on deformation behavior, potentially catalyzing significant breakthroughs in this field.

References

[1] Dixit, P. M., & Dixit, U. S. (2008). Modeling of metal forming and machining processes. Springer.

[2] Seshacharyulu, K., Bandhavi, C., Naik, B. B., Rao, S. S., & Singh, S. (2018). Understanding friction in sheet metal forming-a review. Materials Today: Proceedings, 5(9), 18238-18244.

[3] Hosford, W. F., & Caddell, R. M. (2007). Metal forming. Cambridge University Press.

[4] Kalpakjian, S., & Schmid, S. R. (2013). Manufacturing engineering and technology. Prentice Hall.

[5] Cao, J., Brinksmeier, E., Fu, M., Gao, R. X., Liang, B., Merklein, M., Schmidt, M., & Yanagimoto, J. (2019). Manufacturing of advanced smart tooling for metal forming. CIRP Annals, 68(2), 605-628.

[6] Kumar, S., & Povoden-Karadeniz, E. (2021). Plastic Deformation Behavior in Steels during Metal Forming Processes: A Review. Plastic Deformation in Materials, IntechOpen.

[7] Rosenthal, S., Maaß, F., Kamaliev, M., Hahn, M., Gies, S., & Tekkaya, A. E. (2020). Lightweight in automotive components by forming technology. Automotive Innovation, 3(3), 195-209.

[8] Huh, H., & Kim, S. (2001). Optimum process design in sheet-metal forming with finite element analysis. Journal of Engineering Materials and Technology, 123(4), 476-481.

[9] Haepp, H., & Rohleder, M. (2005). Fe simulation of sheet metal forming state of the art in automotive industry. Advanced Materials Research, 6-8, 13-18.

[10] Allwood, J., Duncan, S., Cao, J., Groche, P., Hirt, G., Kinsey, B., Kuboki, T., Liewald, M., Sterzing, A., & Tekkaya, A. (2016). Closed-loop control of product properties in metal forming. CIRP Annals, 65(2), 573-596.

[11] Eldahshan, H., Munoz, D. P., Alves, J., Perchat, E., & Bouchard, P. (2022). 3d crack initiation and propagation applied to metal forming processes. International Journal of Material Forming, 15(5), 1-26.

[12] Neto, D., Oliveira, M., Santos, A., Alves, J., & Menezes, L. (2017). Influence of boundary conditions on the prediction of springback and wrinkling in sheet metal forming. International Journal of Mechanical Sciences, 122, 244-254.

[13] Hsu, C., Ulsoy, A., & Demeri, M. (2002). Development of process control in sheet metal forming. Journal of Materials Processing Technology, 127(3), 361-368.

[14] Konovalenko, I., Maruschak, P., Brevus, V., & Prentkovskis, O. (2021). Recognition of scratches and abrasions on metal surfaces using a classifier based on a convolutional neural network. Metals, 11(4), 549, 1-14.

[15] Gödri, I. (2022). Improving delivery performance in high-mix low-volume manufacturing

by model-based and data-driven methods. Applied Sciences, 12(11), 5618, 1-22.

[16] Gan, Z. L., Musa, S. N., & Yap, H. J. (2023). A review of the high-mix, low-volume manufacturing industry. Applied Sciences, 13(3), 1687.

[17] Becker, J. M. J., Borst, J., & Veen, A. V. D. (2015). Improving the overall equipment effectiveness in high-mix-low-volume manufacturing environments. CIRP Annals, 64(1), 419-422.

[18] Duda, J., Macioł, A., Jedrusik, S., Rebiasz, B., Stawowy, A., & Sopinska-lenart, M. (2021). Quick response manufacturing for high mix, low volume,high complexity manufacturers. Management and Production Engineering Review. 72-84.

[19] Tan, Y. S., Tjandra, T. B., & Song, B. (2015). Energy efficiency benchmarking methodology for mass and high-mix low-volume productions. Procedia CIRP, 29, 120-125.

[20] Rahnejat, H. (2010). Tribology and dynamics of engine and powertrain. Woodhead Publishing.

[21] Bhushan, B. (2013). Introduction to tribology. John Wiley & Sons.

[22] Stachowiak, G., & Batchelor, A. W. (2005). Engineering tribology. Butterworth-heinemann.

[23] Straffelini, G. (2015). Friction and wear. Springer.

[24] Hutchings, I., & Shipway, P. (2017). Tribology. Butterworth-heinemann.

[25] Bowden, F. P., & Tabor, D. (2001). The friction and lubrication of solids. Oxford University Press.

[26] Nikas, G. K. (2010). Recent developments in wear prevention, friction and lubrication, Research Signpost.

[27] Menezes, P. L., Nosonovsky, M., Ingole, S. P., Kailas, S. V., & Lovell, M. R. (2013). Tribology for scientists and engineers. Springer.

[28] Booser, E. R. (1993). Handbook of lubrication and tribology. Crc-press.

[29] Ludema, K. C., & Ajayi, L. (2018). Friction, wear, lubrication. Crc Press.

[30] Menezes, P. L., Nosonovsky, M., Ingole, S. P., Kailas, S. V., & Lovell, M. R. (2013). Tribology for scientists and engineers. Springer.

[31] Menezes, P. L., Kumar, K., Kishore, & Kailas, S. V. (2009). Influence of friction during forming processesa study using a numerical simulation technique. The International Journal of Advanced Manufacturing Technology, 40(11-12), 1067-1076.

[32] Lupoi, R., & Osman, F. (2005). Under surface pressure sensing technique for the evaluation of contact stresses. Journal of Materials Processing Technology, 164-165, 1537-1543.

[33] Creus, G. (2000). Instability and damage effects in the modeling of metal forming. Computer Methods in Applied Mechanics and Engineering, 182(3-4), 421-437.

[34] Shih, H., & Wilson, W. R. D. (1999). Effects of contact pressure and strain on friction in sheet-metal forming. Tribology Transactions, 42(1), 144-151.

[35] Saha, P. K., & Wilson, W. R. (1994). Influence of plastic strain on friction in sheet metal forming. Wear, 172(2), 167-173.

[36] Hsu, T., & Huang, C. (2003). The friction modeling of different tribological interfaces in extrusion process. Journal of Materials Processing Technology, 140(1-3), 49-53.

[37] Al-mousawi, M., Daragheh, A., Ghosh, S., & Harrison, D. (1992). Some physical defects in metal forming processes and creation of a data base. Journal of Materials Processing Technology, 32(1-2), 461-470.

[38] Trzepiecinski, T., & Lemu, H. G. (2019). Recent developments and trends in the friction testing for conventional sheet metal forming and incremental sheet forming. Metals, 10(1), 47, 1-34.

[39] Lupoi, R., & Osman, F. (2005). Under surface pressure sensing technique for the evaluation of contact stresses. Journal of Materials Processing Technology, 164-165, 1537-1543.

[40] Wang, S., & Rao, K. (1997). An upper-bound analysis of friction in metal forming. International Journal of Mechanical Sciences, 39(2), 201-209.

[41] Jerina, J., & Kalin, M. (2014). Initiation and evolution of the aluminium-alloy transfer on hot-work tool steel at temperatures from 20 'c to 500 'c. Wear, 319(1-2), 234-244.

[42] Lu, J., Song, Y., Zhou, P., Lin, J., Dean, T. A., & Liu, P. (2021). Process parameters effect on high-temperature friction and galling characteristics of aa7075 sheets. Materials and Manufacturing Processes, 36(8), 967-978.

[43] Noh, J. H., & Hwang, B. B. (2018). Influence of punch geometry on surface deformation and tribological conditions in backward extrusion. Journal of Mechanical Science and Technology, 32(1), 323-331.

[44] Sugihara, T., & Enomoto, T. (2012). Improving anti-adhesion in aluminum alloy cutting by micro stripe texture. Precision Engineering, 36(2), 229-237.

[45] Teller, M., Ross, I., Prünte, S., Temmler, A., Küpper, M., Poprawe, R., Schneider, J. M., & Hirt, G. (2018). Probing the potential of structured and surface functionalized tools for dry cold forging of aluminium. MATEC Web of Conferences, 190, 14010, 1-7.

[46] Ghiotti, A., Bruschi, S., & Medea, F. (2017). Wear onset in hot stamping of aluminium alloys sheets. Wear, 376-377, 484-495.

[47] Tripathi, K. (1975). Correlation of chemical and mechanical effects of lubricants. Tribology International, 8(4), 146-152.

[48] Kinoshita, H., Yoshimura, H., & Ohmae, N. (2007). Wettability effect of hydroxyl and alkane fluids for preventing adhesion of aluminum alloy to tungsten carbide. Journal of Advanced Mechanical Design, Systems, and Manufacturing, 1(5), 737-742.

[49] Menezes, P. L., Reeves, C. J., & Lovell, M. R. (2016). Fundamentals of lubrication. Taylor & Francis.

[50] Bartz, W. (1978). Tribology, lubricants and lubrication engineering a review. Wear, 49(1), 1-18.

[51] Zareh-desari, B., & Davoodi, B. (2016). Assessing the lubrication performance of vegetable oil-based nano-lubricants for environmentally conscious metal forming processes. Journal of Cleaner Production, 135, 1198-1209.

[52] Dudkiewicz Ł., Hawryluk M., Ziemba J., Miżejewski A., Polak S., Marzec J., & Szymańska T. (2023). Determination of the friction coefficient in the ring test for selected lubricants dedicated to the hot forging process of precision steel products. Lubricants, 11(9), 399, 1-16.

[53] Sulaiman, M. H., Christiansen, P., & Bay, N. (2019). An experimental compression test of lubricants with direct measurement of lubricant pressure build-up. Jurnal Tribologi, 20, 51-64.

[54] Nielsen, C. V., & Bay, N. (2017). Overview of friction modelling in metal forming processes. Procedia Engineering, 207, 2257-2262.

[55] Wang, C., Ma, R., Zhao, J., & Zhao, J. (2017). Calculation method and experimental study of coulomb friction coefficient in sheet metal forming. Journal of Manufacturing Processes, 27, 126-137.

[56] Hol, J., Alfaro, M. C., Rooij, M. D., & Meinders, T. (2012). Advanced friction modeling for sheet metal forming. Wear, 286-287, 66-78.

[57] Ramezani, M., Ripin, Z. M., & Ahmad, R. (2009). A static friction model for tube bulge forming using a solid bulging medium. The International Journal of Advanced Manufacturing Technology, 43(3-4), 238-247.

[58] Wanheim, T., Bay, N., & Petersen, A. (1974). A theoretically determined model for friction in metal working processes. Wear, 28(2), 251-258.

[59] Wang, D., Yang, H., & Li, H. (2014). Advance and trend of friction study in plastic forming. Transactions of Nonferrous Metals Society of China, 24(5), 1263-1272.

[60] Yang, H., Zhan, M., & Liu, Y. (2002). A 3d rigidviscoplastic fem simulation of the isothermal precision forging of a blade with a damper platform. Journal of Materials Processing Technology, 122(1), 45-50.

[61] Ebrahimi, R., & Najafizadeh, A. (2004). A new method for evaluation of friction in bulk metal forming. Journal of Materials Processing Technology, 152(2), 136-143.

[62] Wilson, W. R. D., Hsu, T., & Huang, X. (1995). A realistic friction model for computer simulation of sheet metal forming processes. Journal of Engineering for Industry, 117(2), 202-209.

[63] Tan, X., Yan, X., Juster, N. P., Raghunathan, S., & Wang, J. (2008). Dynamic friction model and its application in flat rolling. Journal of Materials Processing Technology, 207(1-3),

222-234.

[64] Bay, N., Eriksen, M., Tan, X., & Wibom, O. (2011). A friction model for cold forging of aluminum, steel and stainless steel provided with conversion coating and solid film lubricant. CIRP Annals, 60(1), 303-306.

[65] Yang, X., Liu, H., Zhang, L., Hu, Y., Politis, D. J., Gharbi, M. M., & Wang, L. (2024). Interactive mechanism and friction modelling of transient tribological phenomena in metal forming processes: A review. Friction, 12(3), 375-395.

[66] Wright, P., Horne, J., & Tabor, D. (1979). Boundary conditions at the chip-tool interface in machining: Comparisons between seizure and sliding friction. Wear, 54(2), 371-390.

[67] Hosford, W. F., & Caddell, R. M. (2011). Metal forming. Cambridge University Press.

[68] Sugihara, T., Udupa, A., & Viswanathan, K. (2019). A plastic boundary layer in wedge indentation of aluminum. MATERIALS TRANSACTIONS, 60(8), 1436-1441.

[69] Rigney, D., & Hirth, J. (1979). Plastic deformation and sliding friction of metals. Wear, 53(2), 345-370.

[70] Bourgin & Patrick (1979). Fluid-Film Flows of Differential Fluids of Complexity n Dimensional Approach—Applications to Lubrication Theory. Journal of Lubrication Technology, 101(2), 140-144.

[71] Saiki, H., Ngaile, G., & Ruan, L. (1997). Influence of die geometry on the workability of conversion coatings combined with soap lubricant in cold forming of steels. Journal of Materials Processing Technology, 63(1-3), 238-243.

[72] Duran D., & Özdemir İ.. (2016). Predicting and measuring surface enlargement in forward rod extrusion. Journal of Manufacturing Science and Engineering, 138(7), 1-7.

[73] Totten, G. E., & Mackenzie, D. S. (2003). Handbook of aluminum: physical metallurgy and processes. Crc Press. 48.

[74] Wang, Z., & Yoshikawa, Y. (2014). A new forming method of triple cup by plate forging. Procedia Engineering, 81, 389-394.

[75] Sagisaka, Y., Nakamura, T., Hayakawa, K., & Ishibashi, I. (2013). Evaluation of environmentally friendly lubricant for aluminum cold forging using friction test based on spline extrusion. Journal of Manufacturing Processes, 15(1), 96-101.

[76] Ok, J., & Hwang, B. B. (2006). An analysis on the surface expansion of aluminium alloys in backward can extrusion process. Materials Science Forum, 519-521, 931-936.

[77] Schrader, T., Shirgaokar, M., & Altan, T. (2007). A critical evaluation of the double cup extrusion test for selection of cold forging lubricants. Journal of Materials Processing Technology, 189(1-3), 36-44.

[78] Chang, Y., Wang, B., Li, X., Wang, C., Zhao, K., & Dong, H. (2020). A new continuous tensile-compressive testing device with friction-counteracting and anti-buckling supporting

mechanism for large strain. Journal of Materials Processing Technology, 278, 116540, 1-14.

[79] Zai, L., You, G., Tong, X., Ding, Y., Xu, X., & Liu, Q. (2020). Microstructure and Mechanical Properties of InertiaFriction-Welded Fe–Cr–Ni–Mo High-Strength Steel. Steel Research International, 91(9), 1-12.

[80] Li, Z., Zhao, J., Jia, F., Zhang, Q., Liang, X., Jiao, S., & Jiang, Z. (2019). Numerical and experimental investigation on the forming behaviour of stainless/carbon steel bimetal composite. The International Journal of Advanced Manufacturing Technology, 101(1-4), 1075-1083.

[81] Celik, G., Kaftanoğlu, B., & Karadogan, C. (2011). Investigation of influence parameters on forming limit diagrams of aluminum alloy-aa2024. Key Engineering Materials, 473, 382-389.

[82] Msolli, S., Martiny, M., Cardoso, M. C., Moreira, L. P., Mercier, S., & Molinari, A. (2016). Numerical modeling of the deformation of aisi 304l using a tangent additive mori-tanaka homogenization scheme: Application to sheet metal forming. Journal of Materials Processing Technology, 235, 187-205.

[83] Wang, Y., Liu, Y., Zheng, J., Lan, B., & Jiang, J. (2022). Develop a new strain rate sensitive solid-state pressure bonding model. Materials & Design, 215, 110436.

[84] Zhang, Y., Li, D., Li, X., Li, Y., Liu, X., Wang, H., & Huang, Z. (2022). Study on nonuniform deformation behavior and mechanical properties of complex-shaped ti-6al-4'v extruded profiles with different lubrication conditions. The International Journal of Advanced Manufacturing Technology, 121(9-10), 5885-5899.

[85] Phillips, C., Bould, D., Claypole, T., & Gethin, D. (2009). Finite element modelling of low temperature forming of polymer films with application in in-mould decoration. Materials & Design, 30(3), 537-550.

[86] Larson, M. G., & Bengzon, F. (2013). The finite element method: theory, implementation, and applications. Springer.

[87] Kobayashi, S. (1982). A review on the finite-element method and metal forming process modeling. Journal of Applied Metalworking, 2(3), 163-169.

[88] Zareh-desari, B., Abaszadeh-yakhforvazani, M., & Khalilpourazary, S. (2015). The effect of nanoparticle additives on lubrication performance in deep drawing process: Evaluation of forming load, friction coefficient and surface quality. International Journal of Precision Engineering and Manufacturing, 16(5), 929-936.

[89] Ebrahimi, R., Rezvani, A., & Bagherpour, E. (2018). Circular simple shear extrusion as an alternative for simple shear extrusion technique for producing bulk nanostructured materials. Procedia Manufacturing, 15, 1502-1508.

[90] Xu, S., Zhao, G., Ren, X., & Guan, Y. (2008). Numerical investigation of aluminum deformation behavior in three-dimensional continuous confined strip shearing process. Materials Science and Engineering: A, 476(1-2), 281-289.

[91] Huang, L., Zeng, R., Zhang, X., & Li, J. (2014). Study on plastic deformation behavior of hot splitting spinning of ta15 titanium alloy. Materials & Design, 58, 465-474.

[92] Zhang, D., & Yang, H. (2013). Numerical study of the friction effects on the metal flow under local loading way. The International Journal of Advanced Manufacturing Technology, 68(5-8), 1339-1350.

[93] Challen, J., & Oxley, P. (1984). A slip line field analysis of the transition from local asperity contact to full contact in metallic sliding friction. Wear, 100(1-3), 171-193.

[94] Kim, D., Kang, K., & Earmme, Y. (2001). Integrity analysis of solder joints; fracture mechanics approach. Advances in Electronic Materials and Packaging 2001 (Cat. No.01EX506).

[95] Miguel, V., Benet, J., Coello, J., Calatayud, A., & Martínez, A. (2007). Slip line field applied to deep drawing. AIP Conference Proceedings.

[96] Farmer, L., & Oxley, P. (1984). A method of constructing slip line fields for plane strain compression. CIRP Annals, 33(1), 167-170.

[97] Wright, P. K. (1990). Transparent sapphire tools. Journal of Manufacturing Systems, 9(4), 292-302.

[98] Isobe, H., Uehara, Y., Hara, K., Onuma, T., & Mihara, A. (2012). Experimental verification of machining process of ultrasonic drilling. Key Engineering Materials, 516, 275-280.

[99] Ramulu, M. (1993). Dynamic photoelastic investigation on the mechanics of waterjet and abrasive waterjet machining. Optics and Lasers in Engineering, 19(1-3), 43-65.

[100] Mandal, S., Kumar, A., & Nagahanumaiah. (2012). Dynamic shear stress evaluation on micro-turning tool using photoelasticity. Advanced Materials Research, 569, 376-379.

[101] Wern, C. W., Ramulu, M., & Shukla, A. (1996). Investigation of stresses in he orthogonal cutting of fiber-reinforced plastics. Experimental Mechanics, 36(1), 33-41.

[102] Pallicity, T. D., Vu, A., Ramesh, K., Mahajan, P., Liu, G., & Dambon, O. (2017). Birefringence measurement for validation of simulation of precision glass molding process. Journal of the American Ceramic Society, 100(10), 4680-4698.

[103] Laakso, S. V., Bushlya, V., & Ståhl, J. (2018). The correct way of splitting tools optimization of instrument design for measuring contact stress distribution. Procedia Manufacturing, 25, 97-102.

[104] Arsecularatne, J. (1997). On tool-chip interface stress distributions, ploughing force and size effect in machining. International Journal of Machine Tools and Manufacture, 37(7), 885-899.

[105] Sagapuram, D., Viswanathan, K., Trumble, K. P., & Chandrasekar, S. (2018). A common mechanism for evolution of single shear bands in large-strain deformation of metals. Philosophical Magazine, 98(36), 3267-3299.

[106] Moreton, D. (2001). An introduction to measurements using strain gauges karl hoffmann. Strain, 37(3), 127-127.

[107] Parisot, R., Forest, S., Gourgues, A., Pineau, A., & Mareuse, D. (2000). Modeling the mechanical behavior of a multicrystalline zinc coating on a hot-dip galvanized steel sheet. Computational Materials Science, 19(1-4), 189-204.

[108] Matsuno, T., Shoji, H., & Ohata, M. (2018). Fracture-strain measurement of steel sheets under high hydrostatic pressure. Procedia Manufacturing, 15, 869-876.

[109] Fast-irvine, C., Abedini, A., Noder, J., & Butcher, C. (2021). An experimental methodology to characterize the plasticity of sheet metals from uniaxial to plane strain tension. Experimental Mechanics, 61(9), 1381-1404.

[110] Flores, P., Tuninetti, V., Gilles, G., Gonry, P., Duchêne, L., & Habraken, A. M. (2010). Accurate stress computation in plane strain tensile tests for sheet metal using experimental data. Journal of Materials Processing Technology, 210(13), 1772-1779.

[111] Zaman, S. B., Barlat, F., & Kim, J. (2018). Deformation-induced anisotropy of uniaxially prestrained steel sheets. International Journal of Solids and Structures, 134, 20-29.

[112] Badulescu, C., Grédiac, M., & Mathias, J. D. (2009). Investigation of the grid method for accurate in-plane strain measurement. Measurement Science and Technology, 20(9), 095102-0951011.

[113] Mäntyjärvi, K., Tulonen, J., Saarnivuo, T., Porter, J., & Karjalainen, J. A. (2008). Grid patterns by laser for forming strain analysis. International Journal of Material Forming, 1(S1), 249-252.

[114] Simoncini, M., Forcellese, A., Mancini, E., Chiappini, G., & Sasso, M. (2021). Experimental and numerical investigation on forming limit curves of aa6082 aluminum alloy at high strain rates. The International Journal of Advanced Manufacturing Technology, 112(7-8), 1973-1991.

[115] Smith, J. R., Vaidya, U. K., & Johnstone, J. K. (2014). Analytical modeling of deformed plain woven thermoplastic composites. International Journal of Material Forming, 7(4), 379-393.

[116] Barik, S., Narayanan, R., & Sahoo, N. (2020). Forming response of aa5052h32 sheet deformed using a shock tube. Transactions of Nonferrous Metals Society of China, 30(3), 603-618.

[117] Bandini, C., Reggiani, B., Donati, L., & Tomesani, L. (2015). Code validation and development of user routines for microstructural prediction with Qform. Materials Today:

Proceedings, 2(10), 4904-4914.

[118] Ellis, J., Kirk, R., & Barrow, G. (1969). The development of a quick-stop device for metal cutting research. International Journal of Machine Tool Design and Research, 9(3), 321-339.

[119] Wiklund, U., Rubino, S., Kádas, K., Skorodumova, N., Eriksson, O., Hedberg, S., Collin, M., Olsson, A., & Leifer, K. (2011). Experimental and theoretical studies on stainless steel transfer onto a tin-coated cutting tool. Acta Materialia, 59(1), 68-74.

[120] Hoshi Koichi, & Hoshi Tetsutaro (1969). On the Metal Cutting Mechanism with the Bullt-up Edge. Memoirs of the Faculty of Engineering, Hokkaido University, 12(3), 241-271.

[121] Reu, P. (2012). Introduction to digital image correlation: Best practices and applications. Experimental Techniques, 36(1), 3-4.

[122] Zhang, L., Lin, J., Min, J., Ye, Y., & Kang, L. (2016). Formability evaluation of sheet metals based on global strain distribution. Journal of Materials Engineering and Performance, 25(6), 2296-2306.

[123] Mashiwa, N., Furushima, T., & Manabe, K. (2017). Novel non-contact evaluation of strain distribution using digital image correlation with laser speckle pattern of low carbon steel sheet. Procedia Engineering, 184, 16-21.

[124] Deng, H., Yang, S., Li, G., Zhang, X., & Cui, J. (2020). Novel method for testing the high strain rate tensile behavior of aluminum alloys. Journal of Materials Processing Technology, 280, 116601, 1-14.

[125] Lv, L., Shao, L., Lin, H., & Jin, T. (2022). Deformation and mechanical responses of az31b magnesium alloy under combined shear-compression loading conditions. Materials Today Communications, 31, 103551, 1-18.

[126] Wehrs, J., Mohanty, G., Guillonneau, G., Taylor, A. A., Maeder, X., Frey, D., Philippe, L., Mischler, S., Wheeler, J. M., & Michler, J. (2015). Comparison of in situ micromechanical strain-rate sensitivity measurement techniques. JOM, 67(8), 1684-1693.

[127] Zhao, P., Jiao, J., Tang, Y., & Fang, G. (2021). Investigation on damage evolution and acoustic emission behavior of aluminum alloy sheet during blanking process. The International Journal of Advanced Manufacturing Technology, 117(1-2), 675-688.

[128] Willert, C., Raffel, M., Kompenhans, J., Stasicki, B., & Kähler, C. (1996). Recent applications of particle image velocimetry in aerodynamic research. Flow Measurement and Instrumentation, 7(3-4), 247-256.

[129] Zhang, P., Peterson, S. D., & Porfiri, M. (2019). Combined particle image velocimetry/digital image correlation for load estimation. Experimental Thermal and Fluid Science, 100, 207-221.

[130] Udupa, A., Sugihara, T., Viswanathan, K., & Chandrasekar, S. (2019). Altering the stability

of surface plastic flow via mechanochemical effects. Physical Review Applied, 11(1), 1-16.

[131] Iglesias, P., Bermúdez, M., Moscoso, W., Rao, B., Shankar, M., & Chandrasekar, S. (2007). Friction and wear of nanostructured metals created by large strain extrusion machining. Wear, 263(1-6), 636-642.

[132] Viswanathan, K., Udupa, A., Yeung, H., Sagapuram, D., Mann, J. B., Saei, M., & Chandrasekar, S. (2016). On the stability of plastic flow in cutting of metals. CIRP Annals, 66(1), 69-72.

[133] Udupa, A., Sundaram, N., Sugihara, T., & Chandrasekar, S. (2019). Direct in-situ observation of deformation modes in wedge indentation of metals. MATERIALS TRANSACTIONS, 60(8), 1442-1449.

[134] Murthy, T. G., Huang, C., & Chandrasekar, S. (2008). Characterization of deformation field in plane-strain indentation of metals. Journal of Physics D: Applied Physics, 41(7), 074026, 1-9.

[135] Mahato, A., Yeung, H., Guo, Y., Viswanathan, K., Sundaram, N. K., Udupa, A., Mann, J. B., & Chandrasekar, S. (2017). Sinuous flow and folding in metals: Implications for delamination wear and surface phenomena in sliding and cutting. Wear, 376-377, 1534-1541.

[136] Santos, C. A., Corrêa, E. C. S., Aguilar, M. T. P., Andrade, M. S., & Cetlin, P. R. (2010). The anomalous redundant deformation and work hardening of the aisi 420 stainless steel during axisymmetric drawing. Journal of Engineering Materials and Technology, 132(1), 1-7.

[137] Sundaram, N., Guo, Y., Murthy, T. G., Saldana, C., & Chandrasekar, S. (2012). Rotation field in wedge indentation of metals. Journal of Materials Research, 27(1), 284-293.

[138] Kim, W., Kawai, K., & Koyama, H. (2007). Metal flow in wedge indentation of v- and w-shaped tools. Journal of Materials Processing Technology, 189(1-3), 392-400.

[139] Abraham, T., Bräuer, G., Flegler, F., Groche, P., & Demmler, M. (2015). Dry sheet metal forming of aluminum by smooth dlc coatings a capable approach for an efficient production process with reduced environmental impact. Procedia Manufacturing, 43, 642-649.

[140] Lee, S., Hwang, J., Shankar, M. R., Chandrasekar, S., & Compton, W. D. (2006). Large strain deformation field in machining. Metallurgical and Materials Transactions A, 37(5), 1633-1643.

[141] Buijs, H., Pomerleau, A., Fournier, M., & Tam, W. (1974). Implementation of a fast fourier transform (fft) for image processing applications. IEEE Transactions on Acoustics, Speech, and Signal Processing, 22(6), 420-424.

[142] Gnanamanickam, E. P., Lee, S., Sullivan, J. P., & Chandrasekar, S. (2009). Direct measurement of large-strain deformation fields by particle tracking. Measurement Science

and Technology, 20(9), 095710-095722.

[143] Służalec, A. (1991). An analysis of dead zones in the process of direct extrusion through single'hole flat die. Communications in Applied Numerical Methods, 7(4), 281-287.

[144] Ghassemali, E., Song, X., Zarinejad, M., Atsushi, D., & Tan, M. J. (2013). Bulk metal forming processes in manufacturing. Handbook of Manufacturing Engineering and Technology. 1-50.

[145] Hill, R. (1953). On the mechanics of cutting metal strips with knife-edged tools. Journal of the Mechanics and Physics of Solids, 1(4), 265-270.

[146] Mulhearn, T. (1959). The deformation of metals by Vickers-type pyramidal indenters. Journal of the Mechanics and Physics of Solids, 7(2), 85-88.

[147] Bahi, S., Nouari, M., Moufki, A., Mansori, M. E., & Molinari, A. (2012). Hybrid modelling of slidingsticking zones at the tool-chip interface under dry machining and tool wear analysis. Wear, 286-287, 45-54.

[148] Childs, T., Childs, T. H. C., Maekawa, K., & Obikawa, T. (2000). Metal machining. John Wiley & Sons.

[149] Masjuki, H., Maleque, M., Kubo, A., & Nonaka, T. (1999). Palm oil and mineral oil based lubricantstheir tribological and emission performance. Tribology International, 32(6), 305-314.

[150] Cremers, D. A., & Chinni, R. C. (2009). Laser-induced breakdown spectroscopycapabilities and limitations. Applied Spectroscopy Reviews, 44(6), 457-506.

[151] Arslan, A., Masjuki, H. H., Kalam, M. A., Varman, M., Mufti, R. A., Mosarof, M. H., Khuong, L. S., & Quazi, M. M. (2016). Surface texture manufacturing techniques and tribological effect of surface texturing on cutting tool performance: A review. Critical Reviews in Solid State and Materials Sciences, 41(6), 447-481.

[152] Astakhov, V. P., & Outeiro, J. C. (2005). Modeling of the contact stress distribution at the tool-chip interface. Machining Science and Technology, 9(1), 85-99.

[153] Yang, X., Hu, Y., Zhang, L., Zheng, Y., Politis, D. J., Liu, X., & Wang, L. (2022). Experimental and modelling study of interaction between friction and galling under contact load change conditions. Friction, 10(3), 454-472.

[154] Lagergren, J. (1997). Measurements of multiple normal pressure peaks in flat rolling. Steel Research, 68(7), 313-325.

[155] Viktor P. Astakhov. (2006). Tribology of Metal Cutting. Elsevier Science.

[156] Rees, D. W. A. (2006). Basic engineering plasticity. Butterworth-heinemann.

[157] Jones, R. M. (2009). Deformation theory of plasticity. Bull Ridge Corporation.

[158] Wang, Z. R., Hu, W., Yuan, S. J., & Wang, X. (2018). Engineering plasticity. John Wiley & Sons.

[159] Dixit, U. S. (2020). Modeling of metal forming: A review. Mechanics of Materials in Modern Manufacturing Methods and Processing Techniques. 1-30.

[160] Kümmel, J., Braun, D., Gibmeier, J., Schneider, J., Greiner, C., Schulze, V., & Wanner, A. (2015). Study on micro texturing of uncoated cemented carbide cutting tools for wear improvement and built-up edge stabilisation. Journal of Materials Processing Technology, 215, 62-70.

List of publications

Peer-reviewed journal articles

Xiaoke LIN, Tatsuya SUGIHARA and Toshiyuki ENOMOTO: Effects of interface friction states on plastic deformation in metal surface and bulk, Tribology International, 196（2024）109668.

Xiaoke LIN, Seiji KINOSHITA, Tatsuya SUGIHARA and Toshiyuki ENOMOTO: Exploring the role of the interface adhesion phenomena focusing on surface expansion distribution, Tribology International, 179（2023）108160.

Conference proceedings

Xiaoke LIN, Tatsuya SUGIHARA, Toshiyuki ENOMOTO: Direct observation of surface expansion and its influence on adhesion force at die-workpiece interface in metal forming, Proceedings of the 19th International Conference on Precision Engineering, (ICPE 2022), C184.

Tatsuya SUGIHARA, Xiaoke LIN, Seiji KINOSHITA, Toshiyuki ENOMOTO: Direct Observation of Large-Strain Deformation at Contact Interface in Wedge Indentation of Aluminum, Proceedings of NanoSPD8, (2023) P24

Acknowledgements

This dissertation is the culmination of my Ph.D. studies at Osaka University, Japan. I am profoundly grateful to all the individuals who have supported and encouraged me throughout this journey.

First, I would like to express my sincere gratitude to Professor Toshiyuki Enomoto, for believing in my capabilities and potential as a researcher and accepting me in this laboratory. This journey would not have been possible without his faith and trust in me, and I am truly thankful for the opportunity.

I am truly grateful to Associate Professor Tatsuya Sugihara, my supervisor, for his invaluable advice, unwavering support, and kindness throughout my study. I owe a great deal to his direct guidance on this research topic. Without his counsel, this dissertation would not have been completed.

I also extend my gratitude to Assistant Professor Urara Satake, and all the members of our laboratory for their assistance over the years. Their kind support during my studies has been invaluable, enabling me to adapt to the laboratory environment and gain proficiency in using related equipment.

Lastly, I want to express my heartfelt appreciation to my friends and family who have stood by me from the start. I am especially thankful to my parents. Their kindness and determination serve as constant sources of inspiration. This achievement is as much theirs as it is mine, and I am grateful to share it with them.